TECHNISCHE UNIVERSITÄT WIEN
Vienna University of Technology

Diese Dissertation haben begutachtet:

_____   _____
Prof. Dr. C.W. Fabjan   Dr. Paul Lecoq

Dissertation

Photonic Crystals: Enhancing the Light Output of Scintillation Based Detectors

Ausgeführt zum Zwecke der Erlangung des akademischen Grades eines Doktors der technischen Naturwissenschaften unter der Leitung von

Univ. Prof. Dr. Christian Fabjan
E141
Atominstitut der Österreichischen Universitäten

eingereicht an der Technischen Universität Wien Fakultät für Physik von

Arno R. Knapitsch
Matrikel Nr. 0231068
Schöckelbachweg 55A, A-8045 Graz

Genf, am 21. Oktober 2012   Eigenhändige Unterschrift:

To my family and friends....

Epigram

Do not believe in anything simply because you have heard it. Do not believe in anything simply because it is spoken and rumored by many. Do not believe in anything simply because it is found written in your religious books. Do not believe in anything merely on the authority of your teachers and elders. Do not believe in traditions because they have been handed down for many generations. But after observation and analysis, when you find that anything agrees with reason and is conducive to the good and benefit of one and all, then accept it and live up to it.

Siddhārtha Gautama

Abstract

A scintillator is a material which emits light when excited by ionizing radiation. Such materials are used in a diverse range of applications; From high energy particle physics experiments, X-ray security, to nuclear cameras or positron emission tomography. Future high-energy physics (HEP) experiments as well as next generation medical imaging applications are more and more pushing towards better scintillation characteristics. One of the problems in heavy scintillating materials is related to their high index of refraction. As a consequence, most of the scintillation light produced in the bulk material is trapped inside the crystal due to total internal reflection. The same problem also occurs with light emitting diodes (LEDs) and has for a long time been considered as a limiting factor for their overall efficiency. Recent developments in the area of nanophotonics were showing now that those limitations can be overcome by introducing a photonic crystal (PhC) slab at the outcoupling surface of the substrate. Photonic crystals are optical materials which can affect the propagation of light in multiple ways. In this work, we used 2D PhC slabs consisting of hexagonal placed rods of air or square shaped pillars made of silicon nitride. The 300-500nm thick photonic crystal slab changes the reflection properties of the crystal-air interface in different ways. In our case the pattern was optimized to enable the light extraction of photons which are otherwise confined within the scintillator by total internal reflections. In the simulation part we could show light output improvements of a wide range of scintillating materials due to light scattering effects of the photonic crystal grating. For these calculations we used two different programs. At first, a Monte Carlo program called LITRANI was used to calculate the light propagation inside a common scintillation based detector setup. LITRANI calculates the path of a photon starting from the production inside the crystal by an ionizing event all the way through the different materials until it is absorbed or detected. It uses the Fresnel formulas to calculate the light transition and reflection between different absorbing or non-absorbing materials. The second program in our simulations was used to calculate the light extraction efficiency of our PhC structure. This program calculates the 2D photonic crystal interface using a rigorous

coupled wave analysis (RCWA) tool. It was used to determine the reflection and transition parameters of the PhC slab for a photon of a certain angle and polarization. With the combination of these two programs the overall gain of the PhC modified scintillators could be calculated and we could show a theoretical light yield improvement of 60-100% by the use of PhCs. In the practical part of this work it is shown how the first samples of PhC slabs on top of different scintillators were produced. The aim of these demonstrator samples was to confirm the simulation results by measurements. Through the deposition of an auxiliary layer of silicon nitride and the adaptation of the standard electron beam lithography (EBL) parameters we could successfully produce several PhC slabs on top of $1.2 \times 2.6 \times 5mm^3$ lutetium oxyorthosilicate (LSO) scintillators. In the characterization process, the PhC samples showed a 30-60% light yield improvement when compared to an unstructured reference scintillator. In our analysis it could be shown that the measured PhC sample properties are in close accordance with the calculations from our simulations.

Keywords. Photonic Crystals, Light Yield, Inorganic Scintillators, High Energy Physics, Monte-Carlo Simulations, Rigorous Coupled Wave Analysis, Nanolithography

Kurzfassung

Ein Szintillator ist ein Material das Licht emittiert wenn es durch ionisierende Strahlung angeregt wird. Szintillatoren bieten vielfältige Einsatzmöglichkeiten; Von Hochenergie Physik Experimenten, Röntgen Geräten bis hin zu Gammakameras oder Positronen-Emissions-Tomographie Anwendungen. Zukünftige Hochenergiephysik (HEP) Experimente sowie medizinischen Bildgebungsverfahren setzen eine fortwährende Verbesserung der szintillationseigenschaften von anorganischen Szintillatoren voraus. Ein anorganischer Szintillator ist ein Kristall dessen Moleküle beim Durchgang von ionisierender Strahlung (energiereichen Photonen oder geladenen Teilchen) durch Stoßprozesse angeregt werden und die Anregungsenergie in Form von meist sichtbarem Licht wieder abgeben. Diese Eigenschaft machen sich vor allem Teilchendetektoren und Medizinische Bildgebungsverfahren zu nutze. Bei diesen Detektoren wird besonders viel Wert auf die Lichtausbeute (Light Yield) und die Zeitauflösung (Timing) gelegt. Um diese Eigenschaften zu verbessern, wurde in unserer Arbeit ein altes Problem der anorganischen Szintillationsmaterialien wieder aufgegriffen: Aufgrund des hohen Lichtbrechungsindex dieser Materialien kann das Szintillationslicht nur schlecht zu den Photodetektoren gekoppelt werden. Im Detail geht es um die Indexanpassung von Szintillator und Kopplungsmedium. Da das Kopplungsmedium meist einen kleineren Refraktionsindex als der Kristall besitzt, kommt es zu einer Totalreflektion des Lichts innerhalb des Szintillators. Als Folge davon verbleibt ein großer Teil des Szintillationslichts im Kristall und wird nicht detektiert. Das gleiche Problem tritt auch bei Leuchtdioden (LEDs) auf und ist dort für eine lange Zeit als ein limitierender Faktor für die Gesamteffizienz betrachtet worden. Jüngste Entwicklungen im Bereich der Nanophotonik haben nun gezeigt, dass diese Einschränkungen durch die Verwendung photonischer Kristalle (PhC) überwunden werden können. Photonische Kristalle sind optische Materialien, die die Ausbreitung von Licht in vielfältiger Weise beeinflussen kann. In der vorliegenden Arbeit verwendeten wir zweidimensionale PhC Schichten die durch ein Nanolithographie

Verfahren auf den Szintillator aufgebracht wurden. Die Strukturen bestehen entweder aus dreieckig angeordneten Löchern oder gitterförmig angeordneten Nuten und sind in einer Silikon-Nitrid Schicht eingebracht. Die 300-500nm dicken Photonischen Strukturen auf unseren Szintillatoren ändern die Reflexionseigenschaften der Kristall-Luft Grenzfläche auf unterschiedliche Weise. In unserem Fall wurde das photonische Muster optimiert um die Licht Extraktion von Photonen zu maximieren die anderenfalls interner Totalreflexion unterliegen würden. Im Simulationen Teil unserer Arbeit konnten wir zeigen, dass die Lichtausbeute einer breiten Palette von Szintillationsmaterialien mit photonischen Kristallen verbessert werden kann. Für diese Berechnungen verwendeten wir eine Monte-Carlo-Programm (LITRANI). Mit diesem Programm kann die Lichtausbreitung innerhalb eines Detektor Aufbaus von der Erzeugung des Photons bis zu dessen Registrierung oder dessen Absorption verfolgt werden. LITRANI berechnet die Licht Reflexion und Transmission im Übergang von einem dielektrischen Medium ins andere. Dabei können absorbierende oder nicht absorbierende optische Materialien berechnet werden. Die Software im zweiten Teil der Simulationen berechnet die zweidimensionalen photonischen Kristall Schichten mit Hilfe einer rigorosen Analyse gekoppelter Wellen (Rigorous Coupled Wave Analysis (RCWA)). Dieses Programm wurde verwendet um die Lichtreflexionseigenschaften der PhC Schicht zu berechnen. Dabei kann für jedes Photon die Reflexions- und Transmissionswerte auf Grund dessen Einfallswinkel und Polarisation bestimmt werden. Durch die Kombination der Informationen aus dem Monte-Carlo Programm und der RCWA Berechnung konnte nun ein PhC modifizierter Szintillator simulationstechnisch beschrieben werden. Durch den Vergleich dieser Ergebnisse mit den Ergebnissen einer Simulation eines konventionellen Szintillators konnten wir eine theoretische Verbesserung der Lichtausbeute von 60 bis 100 % zeigen. Im praktischen Teil der Arbeit wurden erste Prototypen von PhC Szintillatoren hergestellt. Durch das Auftragen einer zusätzlichen Schicht aus Siliziumnitrid und die Anpassung der Standard Elektronenstrahl-Lithographie (electron beam lithography - EBL) Parameter konnten mehrere PhC Szintillatoren hergestellt werden. Die PhC Prototypen wurden auf 1,2 mm x 2,6 mm x 5mm große Lutetiumoxyorthosilikat (LSO) Szintillatoren aufgebracht. Bei der Vermessung dieser Szintillatoren konnten wir eine 30-60 % gesteigerte Lichtausbeute an den verschiedenen Mustern feststellen. Durch Anpassung der Simulationsmodelle an die reellen PhC Muster konnte eine gute Übereinstimmung zwischen den theoretischen Berechnungen und den Messungen gezeigt werden.

Schlüsselwörter. Photonische Kristalle, Szintillatoren, Hochenergie Physik, Monte-Carlo Simulationen, Nanolithographie

Acknowledgments

First of all, I would like to express my gratitude to Etiennette Auffray and Paul Lecoq, who invited me to join their group here at CERN and write my PhD in an international leading-edge research facility. Thanks to their trust, help and support it was very easy for me to get acquainted to the new environment, the new colleagues and the new field of research here at CERN. Etiennette Auffray always helped me to organize crystals, equipment, or manpower for my work in the laboratories. Thanks to Paul Lecoq I quickly got introduced to collaboration partners and people who worked in my field of research. I am very thankful to him for always keeping up the motivation during challenging phases of the project. Many thanks to Prof. Christian Fabjan, who agreed to be my university supervisor and helped and motivated me during our bi-weekly to monthly meetings here at CERN. He immediately recognized flaws and weak points in theoretical discussions, measurements or reports and therefore greatly helped to develop my scientific work to a professional level. Furthermore I thank him, but also Etiennette Auffray and Paul Lecoq very much for carefully reviewing and correcting this work as well as all my published papers, posters and reports. Furthermore I would like to thank Dominique Deyrail for the numerous hours he had to spend in our workshop for my work. Dominique was building or modifying various crystal holders, adapters, and measurement equipment as well as polishing and cutting very small and fragile crystals. His great work of high precision and reliability can be credited for the good crystal and measurement results I had obtained in this work. I especially want to point out the support I got from my colleague and friend Benjamin Frisch who worked at the office next door. Starting from my first day here at CERN he consistently helped me with professional, organizational, and private matters and therefore is highly accountable for my fast adaptation to the new living and working environment. Due to his excellent language skills he often was asked to help me communicating within the group or to translate words, emails, and documents to me as well as to make telephone conversations for me. Thanks for your patience Benjamin. Also

Statutory Declaration

I declare that I have authored this thesis independently, that I have not used other than the declared sources / resources, and that I have explicitly marked all material which has been quoted either literally or by content from the used sources.

_____	_____	_____
Place	Date	Signature

Eidesstattliche Erklärung

Ich erkläre an Eides statt, dass ich die vorliegende Arbeit selbstständig verfasst, andere als die angegebenen Quellen/Hilfsmittel nicht benutzt, und die den benutzten Quellen wörtlich und inhaltlich entnommene Stellen als solche kenntlich gemacht habe.

_____	_____	_____
Ort	Datum	Unterschrift

Contents

Chapter 1

Introduction

Contents

1.1 Motivation

Many detectors in particle physics experiments as well as in nuclear medicine imaging cameras are using scintillator based radiation sensors. One of the major challenges for such devices will be the improvement of energy and time resolution of the corresponding detector systems. Both parameters are strongly correlated with the number of photoelectrons which can be registered after a particle has deposited its energy in the scintillator. One of the problems in heavy scintillating materials is that a large fraction of the light which is produced inside the bulk material is trapped inside the crystal due to total internal reflection. According to Snell's law, light can only escape from the crystal into the ambient medium if the angel Θ is smaller than the critical angle Θ_c (see Figure 1.1). The critical angle Θ_c, which is also called total reflection angle, can be calculated by taking the *arcsin* of the ratio between the index of refraction of the ambient medium and the index of refraction of the crystal (see Formula 1.1).

$$\Theta_c = asin(n_{amb}/n_{sc}) \tag{1.1}$$
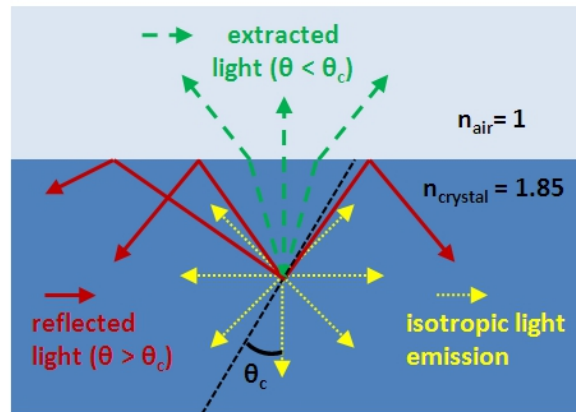
Figure 1.1: Reflected and emitted light at a crystal-air interface when having isotropic light emission within the crystal. Due to total internal reflection, all light which hits the crystal-air interface with an angle larger than Θ_c cannot escape the crystal.

In crystal configurations with high aspect ratio*, up to 50% of the produced light within the scintillator does not reach the photo detector (e.g. photomultiplier tube, photodiode)[1]. Besides photons which are lost due to absorption and scattering in the crystal or crystal-wrapping, a large fraction of these losses can be related to total internal reflection at the detector side of the crystal [2]. One reason is that a large fraction of the photons which reach the outcoupling side of the scintillator are reflected back into the bulk material due to a mismatch of the index of refraction of the scintillating crystal and the outside medium. This problem is well known and so far one has tried to use different crystal geometries, high index of refraction optical contact agents and diffusive wrappings to overcome this problem [3][4].

1.1.1 Light Yield Enhancement by PhC Gratings

The fast emerging field of nanotechnologies provides another technique to cope with that restriction. So-called photonic crystals (PhCs) are a one-, two, or three dimensional periodic arrangements of materials with different indices of refraction. The periodic arrangement affects the propagation of light in the same way as the periodic potential in a semiconductor crystal affects the electron motion. Certain photonic crystal structures have been shown to enhance the light extraction from high index of refraction materials [5][6]. In the field of light emitting diodes (LEDs) photonic crystals have been used suc-

---

*ratio between the area of the lateral faces and the out-coupling face, e.g. aspect ratio = 20 for a crystal of $2 \times 2 \times 10 mm^3$

cessfully to enhance the LED light extraction which is usually restricted by total internal light reflection in the substrate [7][8][9]. To enhance the light extraction efficiency of LEDs PhC structures can be used in different ways. One way is to increase the internal quantum efficiency by the Purcell effect [10] and another way is the so-called band gap effect [7][11]. The aim of this work is to use the PhC as a diffraction grating [12] for scintillating materials. In that case the diffractive properties of a 2D PhC structure are used to couple light into the outside medium (see Figure 1.2. For heavy inorganic scintillators (HIS) this technique was theoretically investigated the first time in the work of [1] and [13].
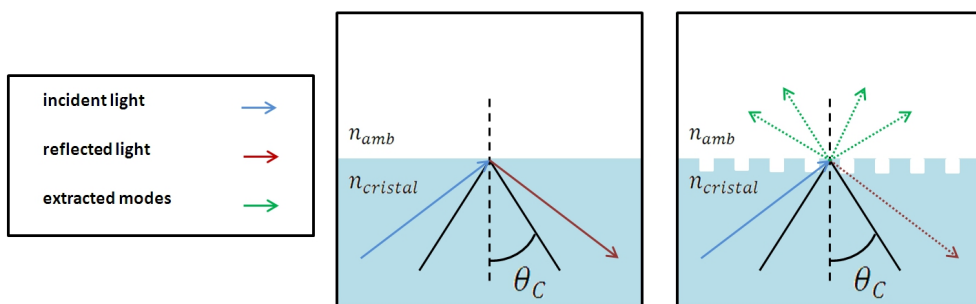
Figure 1.2: Light which is reflected at a plain crystal-air interface (left) can be partially extracted by means of photonic crystal gratings (right).

In the present work, two dimensional PhC structures are used for the light yield improvement on heavy inorganic scintillators (HIS). The measurements and simulations are based on an actual sample which has been produced in cooperation with the Lyon Institute of Nanotechnology (INL). The photonic crystal slab on top of the scintillator operates as a diffraction grating. That means that the photonic crystal changes the reflection properties of a scintillator interface in a way which leads to higher extraction efficiencies [14].

1.1.2 Impact on the Detector Performance

As mentioned before, the main reason for the PhC grating is the light yield enhancement. But a well-designed PhC grating can also have an effect on the energy resolution and the timing of the detector [15][16][17].

Effect on the Light Yield

According to Snell's law, light can only radiate into the ambient medium when the incident angle Θ is smaller than the critical angle $\Theta_c = asin(n_{amb}/n_{crystal})$ (see figure 1.1). The

light extraction efficiency of such a plane crystal-air interface can therefore be calculated as shown in the following formula:

$$\eta_{eff} = \frac{1}{2} \int_0^{\Theta_c} sin\Theta d\Theta \tag{1.2}$$

In this formula, isotropic light emission is assumed over a solid angle of 4π and Fresnel reflection is neglected. To get the efficiency, light is integrated over all angles which can irradiate into air ($\Theta < \Theta_c$). If we do the calculations for LYSO (Cerium-doped Lutetium Yttrium Orthosilicate) which has an refractive index of 1.82, we get an extraction probability of less than 8% at one side of an indefinite plane crystal-air interface (see figure 1.1). For an efficient scintillation based detector, one wants to have the extraction factor as large as possible. To achieve that, the crystals are usually wrapped with a diffusive material and are additionally coupled to the detector with optical grease which has a typical index of refraction of 1.35. In this configuration, the scintillating crystals can achieve a light extraction efficiency of 50-60%. This means, that 40-50% of the produced photons are still lost inside the crystal or the wrapping and the main reason for that can be accounted to the index of refraction mismatch between the crystal and the outcoupling medium. A PhC grating which is minimizing these reflections can therefore have a large impact on the total number of extracted photons.

Effect on the Energy resolution

With the improvement of the light extraction efficiency, the energy resolution R of a scintillation counter will increase since it is statistically linked to the number of detected photons. According to [18] the energy resolution of a scintillation based detector system is proportional to the square root of the fractional variance of a detector signal Q_0 (see Formula 1.3). Q_0 is the product of the number of photons (N) created in the scintillator by one ionizing particle, the photon transfer efficiency (p) and the gain of the photo detector (M) which can be seen in Formula 1.4. Statistical fluctuations in these processes produce variations in the magnitude of Q_0 and therefore determines the energy resolution of the scintillation counter. The contributors to the energy resolution R can be seen as the intrinsic resolution R_i coming mainly from non-proportionality, the transfer resolution R_p and the detector resolution R_M (see Formula 1.5). R_M can now be expressed as Formula 1.6 where the product $\bar{N}\bar{p}$ is the number of photoelectrons which is furthermore dependent on the light collection efficiency. By increasing the number of extracted photons towards a photodetector with a PhC structure, R_M will improve and therefore the overall energy

resolution of the detector.

$$R = \left(\frac{\Delta E_{FWHM}}{E} \right) = 2.354 \sqrt{v(Q_0)} \tag{1.3}$$

$$Q_0 = NpM \tag{1.4}$$

$$R^2 = R_i^2 + R_p^2 + R_M^2 \tag{1.5}$$

$$R_M = 2.354 \sqrt{\frac{1 + v(M)}{\bar{N}\bar{p}}} \tag{1.6}$$

Effect on the Timing

Future detector systems will continue aiming for improved detector performance. In high energy physics experiments for example, better energy resolution will be required for precision measurements of complex events. In the field of medical imaging, better light yield and improved timing would have a directly impact on the signal-to-noise ratio of the images, the dose rate for the patient and the image acquisition time. Especially in time of flight (TOF) positron emission tomography (PET) applications, the timing is essential [19]. The work of [20] gives an overview about the different aspects of the time resolution for future detector systems. According to [18] one component of the time resolution Δt in scintillator based detector systems can be related to the number of extracted photons N_{pht} and the decay time τ as follows:

$$\Delta t \propto \sqrt{\frac{\tau}{N_{pht}}} \tag{1.7}$$

The PhC structure improves the time resolution due to two different effects. First of all the number of extracted photons N_{pht} is increased. According to our simulation, an ideal PhC structure could enhance this number by 60%. Second, the PhC structure extracts most of the photons already on their first incidence on the extraction surface, which would decrease the effective rise and decay time (see Figure 1.3) by avoiding multiple reflections.
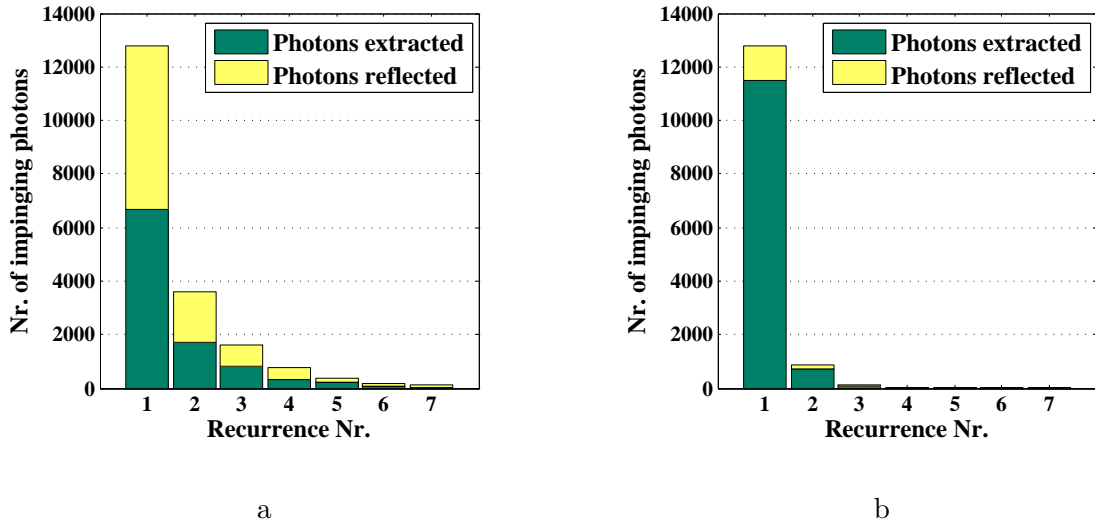
Figure 1.3: Simulation of the recurrence rate of photons at the extraction side of the crystal ($1.2 \times 2.6 \times 5mm^3$ LSO crystal, reflective wrapping, glue contact). One can see, that without a PhC (a), about 2/3 of the photons are reflected at the first incidence and reappear for several times, each time with a loss but also with a certain amount of delay. Using the PhC grating (b), most photons get extracted at the first time they hit the interface, therefore decreasing the effective decay time.

1.2 Related Work

1.2.1 PhC Slabs in Light Emitting Diodes

After the discovery of electroluminescence by the British experimenter H. J. Round the Russian Oleg Vladimirovich Losev reported the first creation of an light emitting diode (LED) in 1927 [21]. The first practical visible spectrum LED was developed several decades later (1962) by Nick Holonyak [22] who is also called the father of the LED. Since then they have been continuously improved regarding their cost, efficiency and reliability. Due to these improvements they are used now in a wide field of applications and it is expected, that LEDs will be the next light source for general lighting. A main restriction for their overall performance is their low light extraction efficiency. Due to the high index of refraction of the semiconductor (2.5 to 3.5) a large fraction of the light produced by the active region inside the LED cannot radiate into the ambient medium. According to Snell's law, only light with a smaller angle than the critical angle can escape the semiconductor [9]. The problem is therefore the same than for the light which wants to escape a scintillating crystal. Since the upcoming of photonic crystals numerous publications investigated the

solution of this problem [7] [23] [24] [25] [26]. Enhancements between 1.5 and 2.5 were reported ([6], [27]). Apart from enhancing the extraction efficiency, PhC are also used to shape the emission profile of LEDs [27]. This could be an advantage in application where the angle of emission is important like headlamps, monitors, or projection devices. Another way of improving LEDs by PhCs is the usage of PhC- omni directional reflectors on the backside of a LED to minimize the absorption losses [28].

1.2.2 PhC Slabs in Photovoltaics

In Photovoltaic, the general pursuit is to reduce the cost and increase the efficiency of solar cells. Many different approaches to do that have been investigated since the birth of the first solar cell. In general PhC are used to decrease reflections, as filters or reflectors, or to redirect light to increase the path length of the light within the solar cell. In multilayer solar cells several of these techniques can be used to enhance the efficiency [29]. In multilayer cells there is a lateral and vertical architecture. In the lateral approach the incident light is split into different spectral components which are then diffracted to cells of different band gap energies. In the vertical stack approach the short wavelength cells are stacked on top of lower energy cells. Another way to improve the efficiency was investigated by the work of [30] where the PhC itself was used for the light absorption.

1.3 The Crystal Clear Collaboration at CERN

This work was initiated and supported by the Crystal Clear Collaboration which is a CERN based group for research and development of scintillation based detector systems. It was set-up in 1990 as an interdisciplinary network involving experts from industry and science from around the world. It combines the expertise of different fields of material science (crystallography, solid state physics, luminescence, defects in solids) with the knowledge of the photon and electron detection instrumentation field.

CERN

CERN (European Organization for Nuclear Research) is the world largest particle physics laboratory. It is situated on the border between Geneva and France and was established in 1954. The organization hosts numerous particle- and high energy physics experiments. The most famous "experiment" at CERN is the large hadron collider (LHC) which is the world's largest and most powerful particle accelerator. It is designed to collide protons

with a center of mass energy of 14 TeV and an luminosity of $10^{34}cm^{-2}s^{-1}$ For heavy ions, e.g. lead (Pb), it is planned to reach 2.8 TeV per nucleon and a luminosity of $10^{34}cm^{-2}s^{-1}$. The LHC consists of two superconducting hadron accelerator rings, installed in a 26.7 km long tunnel which was constructed between 1984 and 1989 for the CERN LEP (large electron positron) collider. The two LHC rings are accelerating the particles in opposite directions and at the four experimental areas the two beams can be crosser to get the particle collisions. The four big experiments at these crossing points are called ATLAS (A Toroidal LHC Apparatus), LHCb (LHC-beauty), ALICE (A Large Ion Collider Experiment) and CMS (Compact Muon Solenoid).

1.4 Guideline through this Work

The introduction gives some insight in the basic principles and the motivation of this work. The second chapter 2 is explaining the theory of the scintillation process and basic characteristics of common heavy inorganic scintillators. It provides some examples of scintillation based detector systems in high energy physics and medical imaging. In the third chapter 3, the theory of photonic crystals is summarized. The chapter starts with basics of the electromagnetic theory of light, continues with the derivation of Eigenmodes from the Maxwell equations and concludes with explaining the out of plane light diffraction of PhC slabs. Chapter 4 describes our approach to model a standard scintillating crystal based detector using a Monte-Carlo program. In this approach, the model parameters of the scintillator were optimized to reproduce actual measurements. The model provides important information about the nature of the light propagation inside a scintillator. To calculate the efficiency of a PhC grating (Chapter 5) a good general model of a scintillator is of great importance. In Chapter 5 the proposed PhC structure is simulated and optimized and the simulation results in combination with the Monte-Carlo program are shown. The structure which has been optimized for maximal light extraction efficiency was then produced using nano lithography techniques which is shown in Chapter 6. There the manufacturing process is outlined. Starting from a plain scintillator, auxiliary layers are deposited and patterned afterwards using electron beam lithography. In Chapter 7 these samples are characterized using light yield and angular distribution measurements. In the summary the measurement and simulation results are compared and discussed and future perspectives and solutions to difficulties of the current approach are outlined.

Chapter 2

Inorganic Scintillators

Contents

2.1 Introduction

A scintillator is a material which produces light (mostly in the visible or UV range) when exposed to an ionizing event. The underlying process is called scintillation which comes from the Latin word *"scintillare"* and means twinkle or sparkle. Scintillation summarizes all physical processes within a material which leads to light emission in a specific wavelength when excited by ionizing radiation. The history of scintillators in high energy physics started in the beginning of the 20th century, when William Crookes invented the Spinthariscope which is a tool to count α particles [31]. The α particles are producing individual scintillations on an activated zinc sulphide screen which has to be visually observed in a darkroom. Visual scintillation counters played an important role in major discoveries by Ernest Rutherford and Hans Geiger. In 1944 Samuel Curran was the first one who used the newly developed photomultiplier tubes for the photon counting [32] and therefore invented the predecessor of the modern photomultiplier scintillation counters.

Nowadays scintillation based detectors are used in numerous applications, starting from detector systems in high energy physics, homeland security, as well as medical imaging. Scintillators can have organic or inorganic composition, further they can be categorized according to their condition of aggregation which divides them into solids, liquids and gases. A very important category of scintillators in high energy physics and other radiation detector applications are the group of inorganic scintillators. They are showing a wide range of favourable physical properties and are therefore the first choice in most of the detector applications.

2.2   The Scintillation Mechanism

2.2.1   The Absorption of the Incident Radiation

The scintillation process starts with the absorption of a high energy photon or particle in order to transform a part of the energy into the scintillation light pulses. Due to their different interaction with matter they can be divided into four different Groups:

1. Heavy Charged Particles

   When a heavy charged particle impinges on a scintillator, the path of the particle is usually straight, just in the rare case of a nuclear collision, large angle scattering occurs. The particle deposits its energy by inelastic collisions with the electrons of the scintillator crystal resulting in a molecular excitation and ionization. The Bethe formula specifies the energy loss $\frac{\delta E}{\delta r}$ which defines the energy δE lost over a path length of δr. It is defined by:

   $$\frac{\delta E}{\delta r} = \frac{4\pi e^4 z^2}{m_0 c^2 \beta^2} NZ \left[ln \frac{2m_0 c^2 \beta^2}{I} - ln \left(1 - \beta^2 \right) - \beta^) \right] \tag{2.1}$$

   where one assumes a homogeneous medium with a density of N atoms/cm^3 and each atom of the atomic number Z. I is an empirical constant and corresponds to the mean excitation and ionization potential of the scintillator. M is the rest mass of the particle, z its charge, β its velocity ($V = \beta c$) and m_o and e are the rest mass of an electron and the electronic charge respectively. For the no-relativistic case ($\beta << 1$) the last two terms in the bracket can be neglected.

2. Electrons

   Electrons deposit their energy by excitation and ionization but also in radiative ways

(Bremsstrahlung due to scattering at electrons and nuclei). Radiative dissipation dominates in high Z materials and also increases with the electron kinetic energy. As an example, the radiative losses of an electron inside a material are getting already as strong as the ionization losses at an kinetic electron energy of $9MeV$ in lead whereas in water or air the electron needs an kinetic energy of $100MeV$ to achieve the same balance [18]. Usually, the electron path is deviating from a straight line due to deflections and can get up to 4 times larger than the straight path. This effect is proportional to Z and inversely proportional to the kinetic energy of the electron [33].

3. Electromagnetic Radiation

While charged particles deposit their energy in a sequence of many ionization and excitation events, the electromagnetic radiation is absorbed or scattered in a single event. The three dominating interactions for EM radiation are the Compton scattering, the photo-electric effect and electron pair production (e^+e^-). The fraction of incident γ-rays which experiences one of these three interactions when passing through a scintillator of the thickness d can be calculated as:

$$f = 1 - e^{-\mu d} \tag{2.2}$$

Where the attenuation coefficient $\mu[cm^{-1}]$ is the sum of the three different linear attenuation coefficients ($\mu = \sigma + \tau + \chi$)corresponding to each of the three interaction possibilities:

- The Compton Effect
  It describes the elastic collision between a γ-ray photon and a free (unbound) electron. A photon with an energy of $E = hv$ collides with an electron which makes the electron recoil in an angle ϕ and with an energy T_c (see Figure 2.1). The scattered photon direction on the other hand shows now an angle of θ compared to the direction of the incident photon and has reduced energy $E' = hv'$. Through the principle of the conservation of energy and momentum, several parameters can be derived:
  The energy of the scattered photon:

$$E' = \frac{E}{1 + \alpha(1 - cos\theta)} \quad \text{with} \quad \alpha = \frac{E}{m_0c^2} \tag{2.3}$$

The energy of the recoiled electron:

$$T_c = E - E' = \frac{\alpha E(1 - cos\theta)}{1 + \alpha(1 - cos\theta)} \tag{2.4}$$

The maximum energy of the recoiled electron in Compton collisions(T_{cm}) appears when $\theta = 180°$ and $\phi = 0°$ (which means a 180° reflection of the photon and an electron acceleration in the direction of the incident photon). Therefore the maximum energy becomes:

$T_{cm} = \frac{E}{1 + \frac{1}{2\alpha}}$

and is known as the Compton edge. In Figure 2.2 one can see a typical scintillation spectrum with the photopeak and the Compton edge.
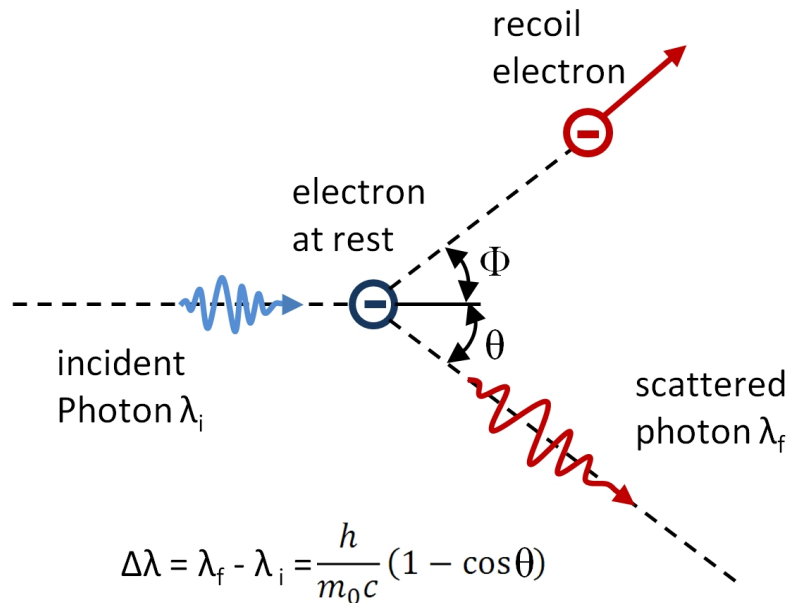
Figure 2.1: Compton scattering. A photon of wavelength λ_i collides with a electron at rest and a new photon of wavelength λ_f emerges at an angle θ.

- The Photo-Electric Effect

In Compton scattering, the energy of the incident gamma photon cannot be completely absorbed since the electrons are considered free and are taking just a certain amount of energy. But if the γ-ray photon hits a bound electron (usually from the K or L shell) the whole Energy E is absorbed and a photo electron with an energy of $T_p = E - B_e$ is ejected where B_e is the binding

Figure 2.2: Example of a scintillation spectrum of a LYSO scintillator on a photomultiplier tube, recorded with a digital oscilloscope.

energy of the electron.

- Pair Production

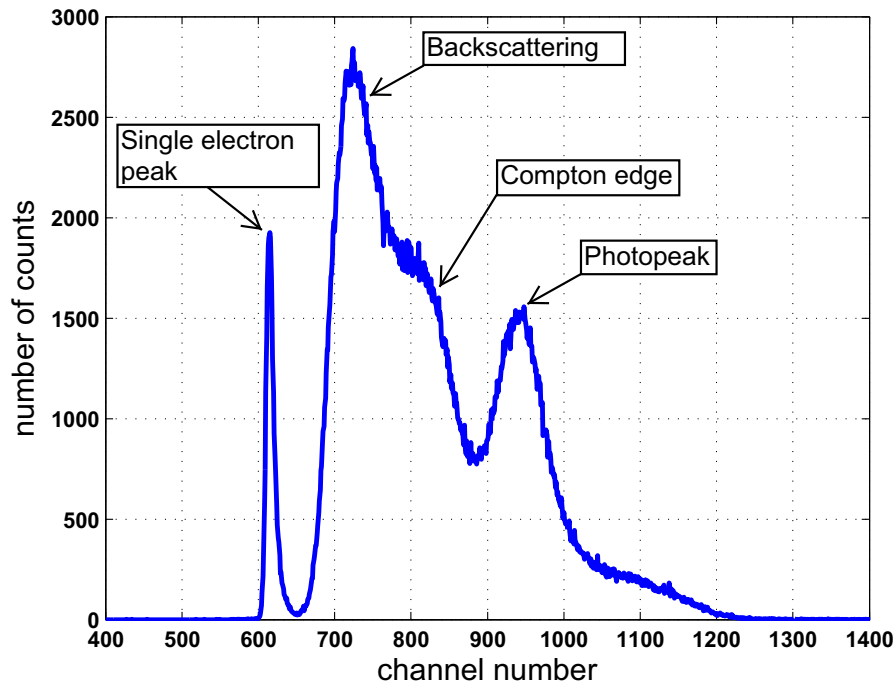 When the incident energy of the γ-ray photon exceeds $2m_0c^2 = 1.02 MeV$, e^+e^- pair production becomes possible. Pair production usually occurs when the photon interacts with a nucleus. In that case, the energy of that photon can be converted into the rest mass energy $2m_0c^2$ and kinetic energy T_{pp} of a electron - positron pair with the total kinetic energy of:

  $T_{pp} = E - 2m_0c^2.$

4. Neutrons

  Since neutrons are uncharged massive particles their interaction is limited to the nuclei of the absorber material. This interaction can be grouped in scattering and absorption. In scattering the most important process is the elastic scattering of neutrons by protons. According to [18] the maximal recoil energy E_{max} of the nucleus can be described by:

  $E_{max} = \frac{4A}{(A+1)^2} E_n$

where A is the mass of the nucleus and E_n the kinetic energy of the neutron. In the case of single protons this means we get a maximal recoil energy equal to E_n and it is decreasing with heavier nuclei. The absorption of neutrons by a nucleus is much more likely with slow neutrons. Neutron absorption can trigger the formation of new stable or unstable isotopes but also nuclear fission when having a heavy nuclei ($Z > 90$).

2.2.2 The Scintillation Process

Scintillation in general can be seen as the summary of all processes which results into an emission of many low energy photons due to an incident gamma-quantum. In Figure 2.3, the elementary processes which occur in inorganic scintillators can be seen [34]. To get a better overview, the scintillation process can be divided into the following five fundamental stages:

1. Energy absorption and creation of electron hole pairs

   When having gamma rays up to an energy of $100keV$ the photo electric effect predominates (see 3. in chapter 2.2.1). This means that the incident γ-ray is producing an electron hole in the inner shell of an atom and a free electron. If it is represented by a single ionization process of an atom A one can write: $A + hv \rightarrow A^+ + e$.

2. Relaxation of the primary electron-hole pairs

   The free electron and the hole relaxation process differs. The hole (atom with ionized inner shell A^+) relaxes either radiatively by emitting a photon or non-radiative by generating an Auger electron (secondary electron released by the energy which is freed after the hole is filled up by an electron of a higher energy level, named after one of its discoverers Pierre Victor Auger). The secondary photon produced in the radiative case as well as the Auger electron can be absorbed by another atom yielding to a new hole and a free electron. Therefore the relaxation of an atom with a hole in the inner shell is triggering a cascade of radiative and non-radiative transitions in the time range of 10^{-13} to $10^{-15}s$

3. Thermalization

   As soon as the electron energy gets smaller than the necessary ionization energy they are interacting with matter by vibrations of the environment which is known as the electron-phonon relaxation or the thermalization stage. In the thermalization
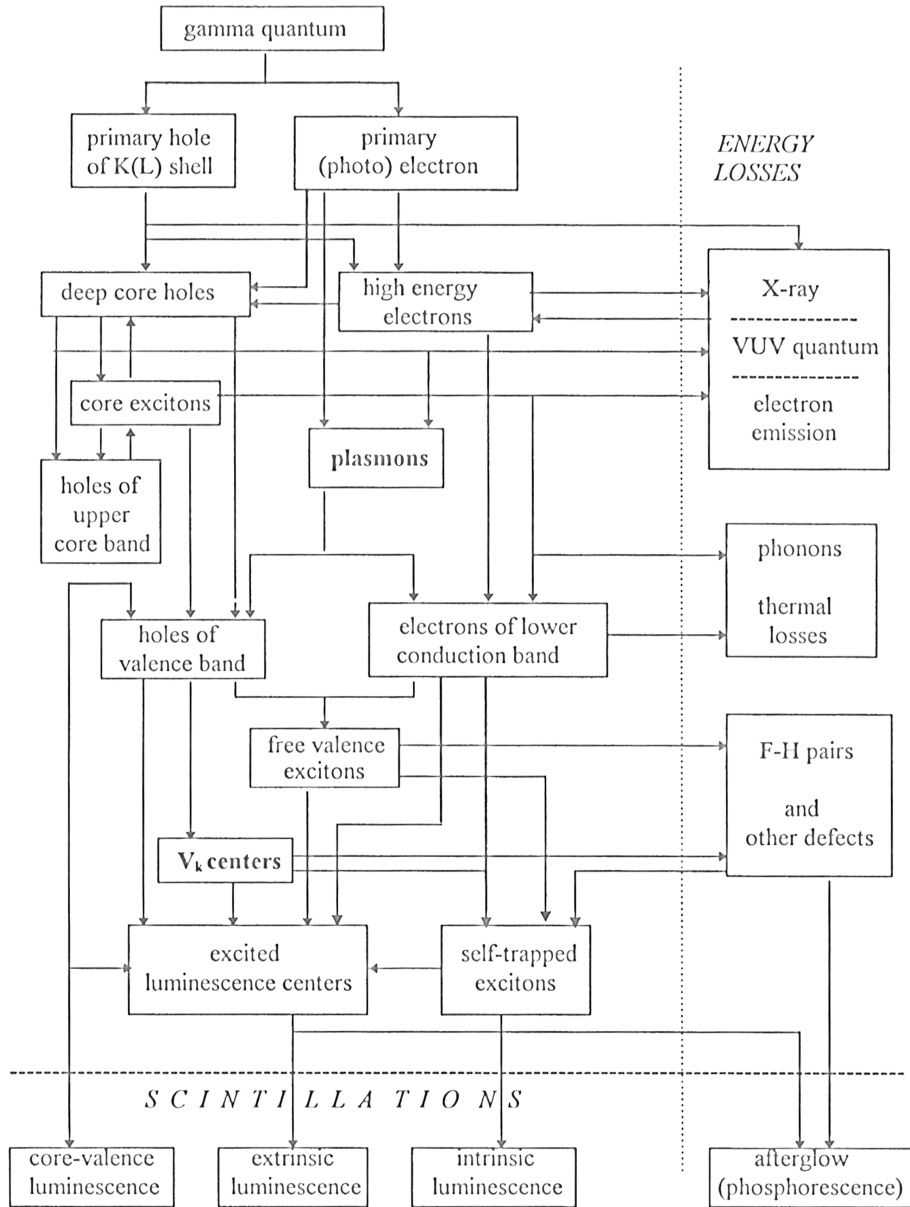
Figure 2.3: Scintillation scheme of the elementary processes within an inorganic scintillator after an absorption of a gamma quantum [34].

process the electrons move down to the bottom of the conduction band and the holes move up to the top of the valence band. Once the holes and electrons are settled the e-h pair energy equals the band-gap energy E_g of the crystal. All ionization processes will at some point create electron-hole (e-h) pairs therefore the number of e-h pairs N_{eh} is proportional to the energy of the initial gamma ray E_γ or other radiations absorbed by the matter:

$$N_{eh} = \frac{E_\gamma}{\xi_{eh}} = \frac{E_\gamma}{bE_G} \tag{2.5}$$

where ξ_{eh} is the average energy required to create a single thermalized e-h pair. Further, ξ_{eh} consists of the product bE_G where E_G is the band gap energy of the crystal and b is a crystal specific constant which is for ionic crystals $b \approx 1.5...2.0$ and $b \approx 3.0...4.0$ for semiconductors. The thermalization time for inorganic crystals is in the range of 10^{-11} to $10^{-12}s$.

4. Energy transfer from e-h pairs to luminescence centers

The energy transfer from e-h pairs to luminescence centers can also be called the migration stage. At this point, two different types of energy transfers are possible: The e-h type and excitonic type of energy transfer. In the e-h type transfer (recombination luminescence) a sequentially capture of either a hole and an electron or an electron and a hole are exciting a luminescence center. In the later case an exciton (bound state of an electron and a hole) is created and is exciting a luminescence center.

5. Emission from the luminescence centers

The emission of luminescence centers can be categorized in intrinsic and extrinsic luminescence. Usually, the intrinsic luminescence is formed by the emission of STEs (Self trapped excitons) and the extrinsic luminescence is defined by the electronic transitions of the activator itself or transitions between activator and the environment. The emission stage is well studied and one is referred to [34] and [35] for a more detailed description.

2.3   Physical Properties of inorganic Scintillators

2.3.1   Light Yield

The light yield is defined by the number of photons produced per unit of energy deposited in the scintillator by an ionizing event (see Formula 2.11). The conversion or energy efficiency of this process (η) relates the number of produced photons N_{ph} to the maximum number of created e-h pairs $N_{eh,max}$ (see Formula 2.6). It can be calculated as a product of the energy conversion efficiency β, the the efficiency of the energy transfer from e-h pairs to luminescence centers S and the quantum efficiency of the luminescence centers Q 2.7:

$$\eta = \frac{N_{ph}}{N_{eh,max}} \tag{2.6}$$

$$\eta = \beta S Q \tag{2.7}$$

The energy conversion efficiency β (Formula 2.8) is a material specific constant which is dependent on the type of chemical bounds in the regarding material. It relates the actual number of created e-h pairs N_{eh} to the theoretical maximum $N_{eh,max}$ which would be present without phonon losses. Due to phonon losses for example, the energy conversion efficiency is smaller in covalent bound materials (semiconductors) than in ionic crystals. The number of electron hole pairs (N_{eh}) can be calculated using Formula 2.10 and equals $N_{eh,max}$ in the case $\beta = 1$ where E_γ is the gamma energy and E_G is the band gap energy of the crystal.

$$\beta = \frac{1}{b} = \frac{N_{eh}}{N_{eh,max}} \tag{2.8}$$

$$N_{eh} = \frac{E_\gamma}{bE_G} \tag{2.9}$$

The efficiency of the energy transfer from e-h pairs to luminescence centers is summarized with (S) and includes the formation of exciton states and groups of excited centers. The luminescence efficiency or quantum efficiency of the luminescence centers Q is the probability that de-excitation takes place by an actual emission of a photon.

Taking formula 2.10 for $b = 1$ and substitute it into 2.6 we can calculate the number of photons generated by a single gamma particle as:

$$N_{ph} = N_{eh,max} \cdot \eta = \frac{E_\gamma}{bE_G} SQ \tag{2.10}$$

The absolute light yield L_{abs} is the total number of photons created for each MeV deposited in the crystal by a gamma photon:

$$LY_{abs} = \frac{N_{ph}}{E_\gamma} = \frac{SQ}{bE_G} [MeV] \tag{2.11}$$

As an example, if we assume a CsI based scintillator with an band gab width of $E_g = 6.2eV$ and $S\&Q \simeq 1$ with $b = 2$, it would give us a calculated light yield of 80,000 $[photons/MeV]$. This theoretical value differs from the measured absolute scintillation light yield which is $64,000 \pm 3200[photons/MeV]$ [34] at room temperature and $70000 \pm 3200[photons/MeV]$ at $-35^{\circ C}$. The difference in the theoretical and the real value of the light yield in CsI is mostly due to limited light transport and transfer efficiency and also due to a limit in the luminescence quantum efficiency (Q). The measurement of the absolute light yield also involves the determination of the light collection efficiency (2.12)and the quantum efficiency of the photosensor. The discrepancy between the number of produced and detected photons can be summarized with the light collection efficiency η_L:

$$\eta_L = \frac{N_{ph,det}}{N_{ph}} \tag{2.12}$$

The measured light output of a scintillator is then defined by formula:

$$LY_{meas} = \eta_L \cdot LY_{abs} \left[\frac{photons}{MeV} \right] \tag{2.13}$$

η_L summarizes all effects which leads to photon losses between the production point inside the scintillator and the photodetector. Main factors for the photon loss are absorption, scattering, reflection and diffusions of the photons along the way to the detector or at the other crystal surfaces. The determination of the absolute light yield has always been a challenging task. While [36] has been using thin crystal samples to evaluate the LY_{abs} others were trying to evaluate it by fitting computer models to experimentally observed light yield values of the according setups [2][37][38].

2.3.2   Time Resolution

Besides of the number of photons generated in a scintillator (Chapter 2.3.1) and the energy resolution (Chapter 2.3.3), the time resolution is one of the main characteristics of a

scintillator or a scintillation based detector system. It describes the ability of discriminate between two consecutive scintillation pulses. This ability is important when having high event rates to reduce the number of unwanted coincidences. But also in the measurement of coincident gamma rays coming from electron-positron annihilation, for example in PET detectors, fast timing is desired. Fast timing is also required in time of flight measurements or positron lifetime measurements which have numerous applications in the field of medical imaging, high energy physics and material sciences. The relative number of photons which are produced inside a scintillator during the time span of one pulse $I_{rel}(t)$ can be approximated by the sum of two exponentials, one describing the rise of the function with the time constant τ_r and one responsible for the decay with τ_d as a time constant (assuming just one averaged decay time constant for simplicity):

$$I_{rel}(t) = \frac{N_{ph}}{\tau_d - \tau_r} \left[e^{-\frac{t}{\tau_d}} - e^{-\frac{t}{\tau_r}} \right] \tag{2.14}$$

Plotting function 2.14 with a rise time of 5ns and a decay time of 40ns and N_{ph}=1000 the scintillation pulse would look like the following plot:
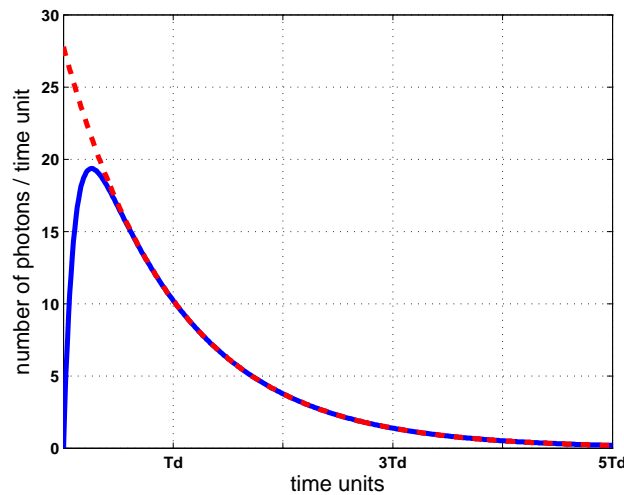

Figure 2.4: Example plot for the rise and decay time of a single scintillation pulse. The red dashed line represents the approximation of the pulse when the rise time is neglected.

Since τ_r in comparison to τ_d is very small it is usually neglected and therefore the formula can be simplified to $I(t) = Ae^{-\frac{t}{\tau_d}}$ (represented by the red dashed line in 2.4 with A the maximal photon emission rate which gives a light yield of $A\tau_d$ between 0 and ∞:

$$I(t) = \int_0^\infty A e^{-\frac{t}{\tau_d}} = A\tau_d \tag{2.15}$$

When looking now to the scintillation pulse from Figure 2.4 it becomes clear that a shorter scintillation pulse (at constant N_{eh}) or an increase of N_{eh} (at constant τ_d) would lead to a better defined pulse shape and therefore increase the time resolution Δt. It can be shown that one component of Δt is proportional to the square root of τ_d and indirect proportional to N_{eh} [34]:

$$\Delta t \propto \sqrt{\frac{\tau}{N_{eh}}} \tag{2.16}$$

2.3.3   Energy Resolution

In most detector physics applications it is important to discriminate different radiation events with different energies. For that it is necessary to get a narrow photopeak so that particles with different energies can be distinguished in the pulse-height spectrum. This can be described by the energy resolution R which is defined as:

$$R[\%] = 100 \cdot \left(\frac{\Delta E_{FWHM}}{E} \right) \tag{2.17}$$

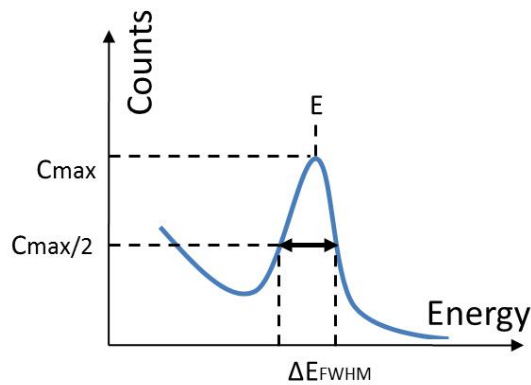Where FWHM is the full width at the half maximum (see 2.5)

Figure 2.5: Definition of FWHM - Full width (ΔE) at half the maximum of the peak count .

According to [39] and [18] the energy resolution R can be related to the fractional (or

relative) variance $v(x)$ as

$$R = \left(\frac{\Delta E_{FWHM}}{E}\right) = 2.354\sqrt{v(Q_0)} \tag{2.18}$$

where $v()$ is the fractional variance defined as the variance of an event divided by its mean value: $v(x) = var(x)/\overline{X}$. The multiplication factor 2.354 is the numerical expression of the term $2\sqrt{2ln2}$ and is derived from the definition of a Gaussian function which can be assumed when having a large number of events. Q_0 is the average charge accumulated in the photomultiplier anode for one pulse:

$$\overline{Q_0} = \overline{N}\overline{p}\overline{M} \tag{2.19}$$

where:

$\overline{N}$	Mean number of photons arriving at the PMT
$\overline{p}$	average transfer efficiency describing the probability that a photon is converted into an electron at the first dynode of the PMT
$\overline{M}$	Mean electron amplification factor for the PMT

The fractional variance of the PMT signal $v(Q_0)$ is approximated by formula 2.20 [18]

$$v(Q_0) \approx \left[v(N) - \frac{1}{\overline{N}}\right] + v(p) + \frac{1 + v(M)}{\overline{N}\overline{p}} \tag{2.20}$$

The term in the square brackets represents the variance of the photons produced in the scintillator which are not from a Poisson process. Therefore, for $v(N) = \overline{N}^{-1}$ (purely Poisson) the bracket term vanishes. The variance in the PMT gain is described by $v(M)$ which makes the right term the PMT-variance. The middle term $v(p)$ is the transfer variance of the photon to electron conversation of the PMT. If we relate the overall energy resolution R of a detector system in the intrinsic resolution R_i, the transfer resolution R_p, and the PMT resolution R_M we get $R^2 = R_i^2 + R_p^2 + R_M^2 = 5.54v(Q_0)$ (See also Formula 2.18). The intrinsic resolution can be further split up into the resolution describing the variation of the scintillator response due to non-proportionality (different energies causing a non-proportional release of photons, further reading see [18]) R_{np} and into the resolution describing the variation due to inhomogeneities in the crystal R_{inh}.

Inhomogeneities in the response can be caused by different concentration of luminescence centers within the crystal as well as by incomplete gamma ray absorption in small crystals or crystal edges as well as scattering effects. More details and actual data for different scintillators can be seen in [40], [41], [42], and [43]. The transfer efficiency p describes the probability that a photon produced in the scintillator will release an electron in the first dynode. Therefore the related transfer resolution R_p is influenced by many factors. For example the wavelength λ of the photon and the regarding quantum efficiency (QE) of the photomultiplier tube. But also the transmittance of the scintillator, the optical properties of the wrapping, the optical coupling to the PMT window, angle of incidence of the photon on the PMT, the uniformity of the photocathode, and the photoelectron collection efficiency at the first dynode are having an influence on R_p. In the modern scintillation based detector systems the transfer resolution component is negligible compared to the intrinsic and photomultiplier resolution. Thus one can reduce the formula for the energy resolution R to:

$$R^2 = R_i^2 + R_M^2 \tag{2.21}$$

with R_M:

$$R_M = 2.35\sqrt{\frac{1 + v(M)}{\overline{N}\overline{p}}} \tag{2.22}$$

When the variance of the PMT gain $v(M)$ is known (usually between 0.1-0.2[44]), the PMT Resolution can be evaluated experimentally by measuring the number of photoelectrons N which is the product of $\overline{N}\overline{p}$ (mean number of photons times the mean photon transfer efficiency). Using formula 2.21 the intrinsic resolution can also be obtained when the overall energy resolution of the detector system is known or measured. An overview of the intrinsic energy resolution of common scintillators (1995) can be seen in Table 2.1 [39]. More recent results on energy resolution can be seen in [45], [46] and [47].

Table 2.1: Light yields (N), photoelectron yields ($\overline{N}\overline{p}$) and energy resolution R for 662 keV gamma excitation [39]. R_M and R_s is the PMT resolution and the scintillator resolution respectively. The references to the according measurements and the dimensions of the crystals used in the measurements can be seen in [39].

Crystal	N $10^3 ph/MeV$	$\bar{N}\bar{p}$ pe/662keV	R %	R_M %	R_s %	PMT
$NaI(Tl^+)$	38-43	6230	6.5	3.1	5.7 ± 0.2	R1306
		4900	7.1	3.7	6.1 ± 0.2	R1306
$CsI(Tl^+)$	65	3240	7.3	4.3	5.9 ± 0.3	XP2020Q
		3640	5.7	4.2	3.9 ± 0.4	R1306
$CsI(Na^+)$	42	5740	7.4	3.3	6.6 ± 0.34	R1306
$CaF_2(Eu^{2+})$	24					
$CdWO_4$	≈ 28	2380	6.8	5.2	4.4 ± 0.4	R1306
		1200	8.0	7.3	3.3 ± 0.6	R1306
$Bi_4Ge_3O_{12}$	9	960	9.3	8.1	4.2 ± 0.6	R1306
		960	9.0	8.1	3.9 ± 0.76	R1306
BaF_2	11	1590	7.8	6.2	4 ± 1.03	XP2020Q
		1590	7.7	6.2	4.6 ± 0.5	XP2020Q
$Gd_2SiO_5(Ce^{3+})$	8.5-10	1250	7.8	7.3	2.7 ± 1.0	R878
		1480	7.8	6.6	4.2 ± 0.56	R1306
$YAlO_3(Ce^{3+})$	14.3	1900	7.28	5.7	4.4 ± 0.5	R2059
		1740	5.7	5.9	4.6 ± 0.5	XP2020Q
$Lu_2SiO_5(Ce^{3+})$	23	3360	7.9	4.4	6.6 ± 0.34	R878
$Lu_3Al_5O_{12}(Sc^{3+})$	23	2320	6.5	5.1	4.0 ± 0.4	XP2020Q
$K_2LaCl_5(Ce^{3+})$	28	3900	5.1	3.9	3.3 ± 0.4	XP2020Q

2.4   Requirements in Medical Imaging and High Energy Physics Applications

2.4.1   Medical Imaging

Heavy inorganic scintillators have become an important part of many medical imaging applications. They are used in x-ray radiology, positron emission tomography (PET) and scintigraphic applications (gamma cameras). The operation principle of these technique can be seen in Chapter 2.5.2. The most widespread technique is x-ray radiology and computed tomography (CT) which also can be seen in Table 2.2 where the annual usage of scintillators of each technique is given in the year 1999. Due to their different modes of operation and their different x-ray and gamma ray energy levels (see Table 2.3), each technique has special requirements regarding their scintillator materials. In general, crystals with a high light yield are required by all of them. Like that, one can keep the integrated x-ray flux or injected activity for the patient to a reasonably low level while getting good imaging results by a high detection efficiency.

Modality	Annual Production	Scintillator Content	Annual Scint. Volume
Planar X-Ray	1,000,000 screens	50 cc / screen	50,000 liters
X-Ray CT	2,000 scanners	75 cc / scanner	150 liters
SPECT	2,000 scanners	3,000 cc / scanner	6,000 liters
PET	50 scanners	10,000 cc / scanner	500 liters

Table 2.2: Worldwide annual scintillator material usage by the different medical imaging techniques in 1999 [48].

Imaging modalities and radiation energies

Imaging modality		Energies
X-ray imaging	Mammography	$25\,kVp$, $\sim 18\,keV$
	Radiography, chest	$150\,kVp$
	Fluoroscopy	$150\,kVp$
	X-ray CT	$150\,kVp$
Nuclear medicine	Scintigraphy	$\sim 80/140\,keV$
	SPECT	60–$511\,keV$
	PET	$511\,keV$

Table 2.3: Photon energy levels of different nuclear medicine imaging techniques [49].

In the following, a few special requirements for each application are mentioned:

Computed Tomography:

Since the technique makes use of very small differences in the attenuation of the x-ray signal (the transmitted flux must be measured in the 1-10ppm accuracy range), systematic errors of the scintillator must be minimized by all means. Therefore one requires a homogeneous crystal with low afterglow, small temperature coefficient and good radiation hardness. In Table 2.4 the properties of the three most frequently used scintillator materials are shown.

Material	Luminosity (photons/MeV)	Density (g/cm^3)	Decay (μs)	Afterglow (@ 3 ms)	Form
CdWO$_4$	14,000	7.9	5, 20	<0.1%	Crystal
(Y,Gd)$_2$O$_3$:Eu,Pr	19,000	5.9	1000	3%	Ceramic
Gd$_2$O$_2$S:Pr,Ce,F	21,000	7.3	3	<0.1%	Ceramic

Table 2.4: The three main scintillator materials used for CT imaging and their properties [48].

Positron Emission Tomography :

In PET one tries to detect the two back-to-back 511keV photons coming from an electron-positron annihilation process. By using time coincidence instead of a mechanical collimator (like in SPECT - single photon emission computed tomography), it can operate much more efficient than SPECT. Important properties for scintillators in PET applications are listed in Table 2.5, where two commonly used scintillator types (BGO, LSO) are specified. Apart from the short attenuation length, which is necessary to stop the 511 keV gamma ray within a reasonably crystal thickness, the time- and energy resolution becomes more and more important. A good time resolution is necessary to detect the coincidence of the two 511 keV photons, but even more important for time of flight applications (see Chapter 2.5.2). A good energy resolution is required to keep a good signal to noise ratio by distinguishing between scattered and true coincidences.

2.4.2 High Energy Physics

There are four main factors governing the choice of scintillator materials in high energy physics detectors:

Material	Luminosity (photons/MeV)	Atten. Length (cm)	Decay Time (ns)	Wavelength (nm)
$Bi_4Ge_3O_{12}$	8,000	1.1	300	480
Lu_2SiO_5:Ce	25,000	1.2	40	420

Table 2.5: Two of the most common used PET scintillator materials and their characteristics [48].

1. Radiation Length

   The radiation length describes the electromagnetic interaction of matter with an high energy particle. It is defined as the mean length in the material where an electron loses $1 - e^{-1}$ of its energy. The symbol for it is usually X_0 and the unit is $g \cdot cm^{-2}$. It is obvious that for scintillators a short radiation length is preferred. This is accomplished by a compact crystal lattice and not only by using high Z elements, which would result in a large Moliere radius ($R_M = 0.0265 X_0 (Z + 1.2)$) and therefore to a large shower size [35].

2. Scintillation Properties

   For the scintillation properties one has to mention decay time, light yield, emission wavelength and energy resolution. The LHC is designed for a bunch crossing time of 25ns which means that the detectors must be fast enough to distinguish between two consecutive bunches. If the detector has to be operated in a magnetic field, like in most electromagnetic calorimeters, one cannot use photomultiplier tubes. The PIN diodes or avalanche photo diodes which are usually used instead of PMTs are having a much lower gain which is compensated by low-noise preamplifiers. In addition the light yield of the crystal must be high enough to reach the desired statistics. Also the emission wavelength of the scintillator has to be in the range where photodiodes have a sufficiently good sensitivity which usually starts at 300nm and peaks somewhere between 500nm and the near infrared range. The energy resolution of a detector describes the capability of distinguishing two different particles with different energy. Therefore the scintillator should have a small light yield variation when excited by particles of the same energy to get a narrow photopeak in the pulse-height spectrum.

3. Radiation Hardness

   After a certain amount of radiation, a scintillating crystal can show radiation damage effects. These damage effects are mostly due to the formation of colour centers in the

bulk material which can absorb the scintillation light on its way to the photodetector [50]. In the case of electromagnetic calorimeters at the LHC but also at other big high energy physics experiments, the scintillating crystals are in an constant high radiation environment over a long period of time. Therefore it is necessary to use materials with good radiation hardness. A better radiation hardness can be reached by the optimization of the stoichiometry in the crystal production process but also by doping (e.g. Yttrium or Niobium in the case of PWO crystals [51]).

4. Cost

There are several parameters governing the costs of a crystal. There is the cost of the raw material, the cost of the growing technique and the cost of the mechanical processing like cutting and polishing. If the crystal structure contains some rare earth elements, for example lutetium or cerium, the raw material can be a major cost factor. The expenses for the growing technique is mainly governed by the energy costs, since one has a very slow pulling rate (1-2 mm/h) and a usually high melting point (e.g. GSO: $> 1900^{\cdot}C$). The price for the mechanical processing of the final crystals is mainly depending on the crystal size (small crystals are harder to manipulate) and their mechanical properties which will affect the throughput of the cutting and polishing process.

2.5   Scintillation based Detector Systems

2.5.1   High Energy Physics

Scintillation based detector systems are used in a lot of different parts of the HEP experiments. While at some points they are just small detectors for beam monitoring or triggering applications they can be very big in case of calorimeters. In the following examples, two big heavy inorganic crystal based detector systems are explained into more detail, one detector from the LHC at CERN an one detector from the SLAC (Stanford linear accelerator):

CMS - Electromagnetic Calorimeter (ECAL)

One part of the CMS experiment is the electromagnetic calorimeter (ECAL) (see overview in the introduction). It is made of 61200 lead tungstate ($PbWO_4$) crystals mounted in the central barrel part and 7324 crystals in each of the two endcaps. Avalanche photodiodes (APDs) are used as photodetectors in the barrel and vacuum phototriodes (VPTs) in the endcaps (see pictures in Figure 2.8). One of the driving criteria in the design of the CMS was the capability to detect the two photon decay of the recently observed Higgs boson and this capability is enhanced by the good energy resolution provided by a homogeneous crystal calorimeter. The design and the specifications of the CMS ECAL can be seen in Figure 2.7 and 2.6.

Lead Tungstate ($PbWO_4$) Crystals:

Lead Tungstate was chosen for the ECAL due to its favourable properties for the application in the high event rate LHC environments. $PbWO_4$ have a radiation length of 8.9 mm, a density of 8.28 g/cm^3 and a Molière radius of 22 mm. Also the optical transmittance (see Figure 2.9) and the radiation hardness has been improved leading to a mass production of homogeneous crystals for high energy calorimetry applications [54] [55][56][57]. In addition, the decay time has been improved in a way that 80% of the light is emitted before 25 ns which is an important criteria for CMS since this is the bunch crossing time of the LHC [58] [59]. The light output is 4.5 photoelectrons per MeV which are collected by the APDs and varies with the temperature at a rate of $2.1\%/C^\circ$ at $18^\circ C$. The crystals are polished for better light collection at the photodetectors. Because of the pyramid like shapes of the barrel type crystals, the polishing leads to a non-uniformity of the light collection along the crystal. To reduce that effect, they were depolished at one lateral
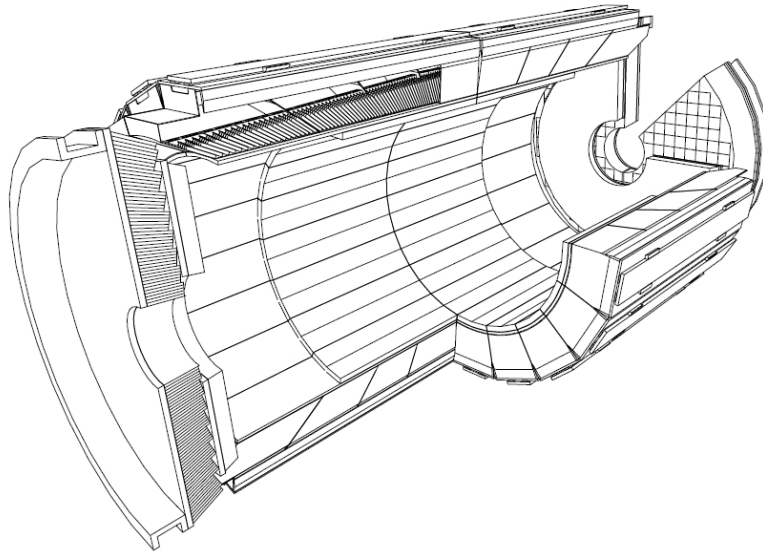
Figure 2.6: A 3-D view of the barrel and endcap of the CMS electromagnetic calorimeter [52].

Parameter	Barrel	Endcaps
Pseudorapidity coverage	$|\eta| < 1.48$	$1.48 < |\eta| < 3.0$
ECAL envelope: r_{inner}, r_{outer} [mm]	1238, 1750	316, 1711
ECAL envelope: z_{inner} z_{outer} [mm]	0, ±3045	±3170, ±3900
Granularity: $\Delta\eta \times \Delta\phi$	0.0175×0.0175	0.0175×0.0175 to 0.05×0.05
Crystal dimension [mm^3]	typical: $21.8 \times 21.8 \times 230$	$24.7 \times 24.7 \times 220$
Depth in X_0	25.8	24.7
No. of crystals	61 200	21 528
Total crystal volume [m^3]	8.14	3.04
Total crystal weight [t]	67.4	25.2
Modularity	36 supermodules	4 Dees
1 supermodule/Dee	1700 crystals (20 in ϕ, 85 in η)	5382 crystals
1 supercrystal unit	–	36 crystals

Figure 2.7: Overview of the endcap and barrel design parameters of the ECAL.

face.

Electromagnetic Calorimeter (EMC) at the BaBar Experiment (SLAC)

The name BaBar is derived from the name for the B meson (symbol B) and its antiparticle (symbol $\bar{B}$, pronounced B-bar). It was located at the Stanford linear accelerator center (SLAC), which is operated by the Stanford University for the Department of Energy in California. The detector was built to understand the imbalance of matter and antimatter
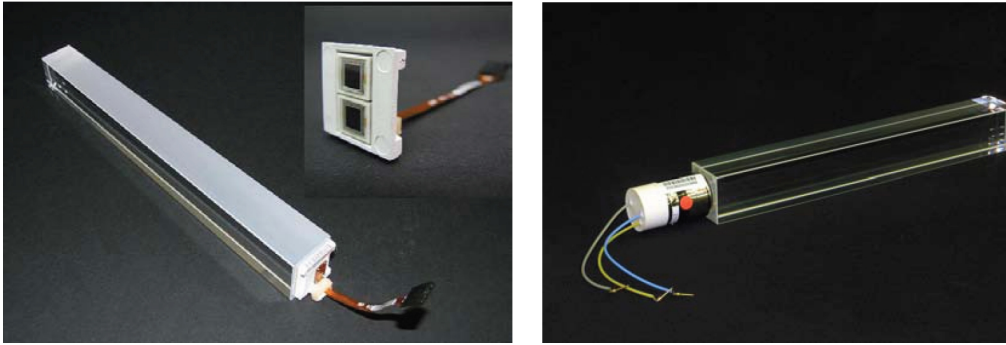
Figure 2.8: $PbWO_4$ crystals with avalanche photodiodes (APDs) or vacuum phototriodes attached. Left side: A barrel crystal with the upper face depolished and the APD capsule. In the insert, a capsule with the two APDs can be seen. Right side: An endcap crystal with a vacuum phototriode attached. [53]
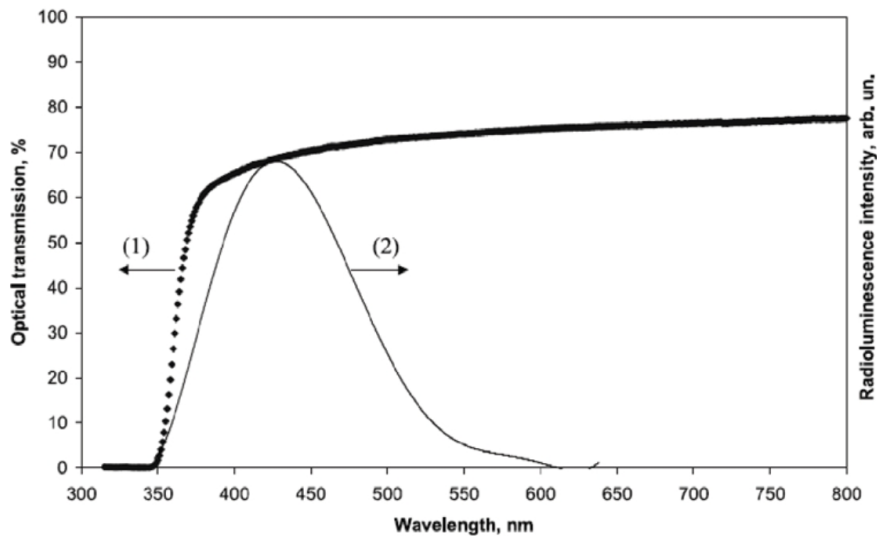
Figure 2.9: Optical transmission in the longitudinal direction (1, left scale) and radioluminescence intensity (2, arbitrary units) at room temperature. Picture taken from [56]

in the universe by measuring CP violation which is a combination of charge conjugation symmetry (C symmetry) and parity symmetry (P symmetry) and especially focuses on the CP - violation in the B meson system. More on the physics behind the BaBar experiment can be seen in [60] and detailed information about the design can be seen in [61]. Here I will focus on the ECAL system of BaBar since it is a good example for a large detector based on Cesium Iodide scintillators (while CMS ECAL is PWO based). The EMC is built to measures photons in the energy range from 20 MeV to 8 GeV with a high energy

resolution. Due to the specifications for the EMC (see Figure 2.10) and its required size and placement inside the detector, it is using Thallium activated Caesium Iodide scintillators $CsI(Tl)$. The specifications for $CsI(Tl)$ can be seen in Figure 2.11. The EMC includes 6580 $CsI(Tl)$ crystals, 5680 in the barrel and 900 in the front end cap. They are between 26.88cm and 32.35 cm long and have an average front face area of $4.8 \times 4.7cm$ and an average back face area of $6.1 \times 6.0cm$. To enhance the light yield and the uniformity along the crystal length, they are wrapped in tyvek (spunbonded olefin paper produced by DuPont). Additionally, they are wrapped in Mylar (Polyester film, trademark of DuPont) for the electric insulation and aluminium foil for the electromagnetic shielding (see Figure 2.12).

Parameter	$B_A B_{AR}$ Design Performance
$\frac{\sigma_E}{E}$ (Stochastic Term) at 90°	1%
$\frac{\sigma_E}{E}$ (Constant Term) at 90°	1.2%
σ_θ at 1 GeV at 90°	5 mr
Efficiency at 20 MeV at 90°	85%
Efficiency at 100 MeV at 90°	95%
π/e Rejection at 500 MeV/c	few$\times 10^{-3}$
Minimum Detectable Energy	10–20 MeV
Electronic Noise/Crystal	$\leq$150 keV

Figure 2.10: Target performance for the $CsI(Tl)$ calorimeter [60].

2.5.2 Medical Imaging

The creation of images of the human body (or parts of it) by medical imaging techniques has become an essential part of modern medicine. Scintillating crystals are playing an important part in most of these machines. In x-ray radiology or computer tomography (CT), scintillators are used for x-ray detection. In whole body counters, they are used in flat arrays as gamma ray cameras for the detection and localization of radiation within a human body. In positron emission tomography (PET) devices, scintillators are used to detect the two gamma rays of positron-electron annihilation.

2.5.2.1 Positron Emission Tomography (PET)

In PET, a positron emitting, biologically active compound (usually FDG - Fludeoxyglucose, a glucose analog including the positron-emitting isotope fluorine-18) is introduced

Properties	CsI	CsI(Tl)	CsI(Na)
Radiation Length (cm)	1.86	1.86	1.86
Absorption Length (cm)	34.2	34.2	34.2
Light Yield (Photons/ MeV $\times 10^3$)	2–10	50–60	38–44
Light Yield Temperature Coef. (%/°C)	0.1	0.1	0.1
Molière Radius (cm)	3.8	3.8	3.8
Peak Emission (nm)	320	565	420
Lower Wavelength Cutoff (nm)	260	320	300
Refractive Index at Emission Maximum	1.95	1.79	1.84
Decay Time (ns)	10	940	630
Density (g/ cm^3)	4.51	4.51	4.51
Hygroscopic	slight	slight	weak

Figure 2.11: Characteristics of pure and doped *CsI* at room temperature [60].
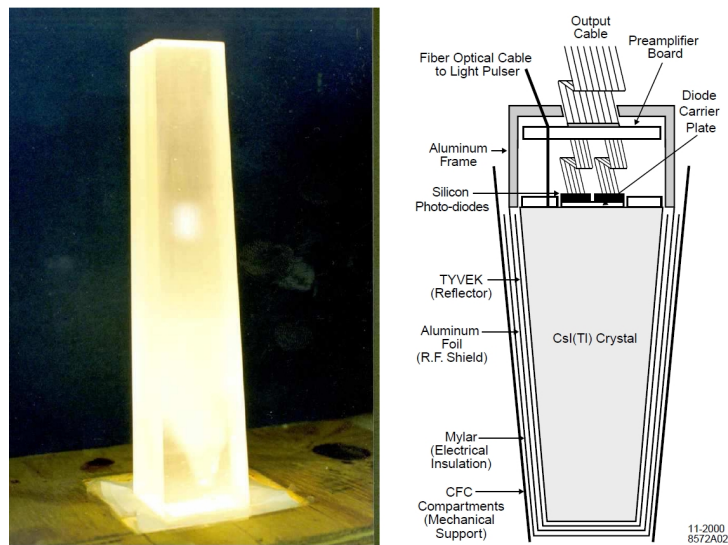
Figure 2.12: Left: Picture of a CsI(Tl) crystal lit from the bottom. Right: Schematic drawing of a CsI(Tl) crystal with different wrappings and attached electronics [62].

into the body, usually by inhalation or injection. The compound accumulates in the regions of the body with high metabolic activity, such as most types of malignant tumours. By tracking the radioisotope within the body one can get a metabolic distribution map of the investigated body part. The emitted positron of the compound is immediately annihilated by an electron which results in two photons traveling in the opposite direction. The

typical schematics of a PET camera can be seen in Figure 2.13. It usually consists of a ring of small photon detectors. When two detectors see a 511 keV photon in time coincidence, a line of all the possible positions in between these two detectors can be drawn (also called line of response LOR). After a number of different coincidences, a 2D density map emerges and if several detector rings are stacked up a 3D image can be drawn. At the moment, the best spatial resolution of commercial PET systems is in the range of 3mm. In the recently introduced time of flight (TOF) PET systems, the resolution could be further improved by measuring the time difference of the arriving two 511 keV photons in coincidence which would give the exact emission point along the LOR. For that technique to work, one has to further optimize the time resolution of the detector system.
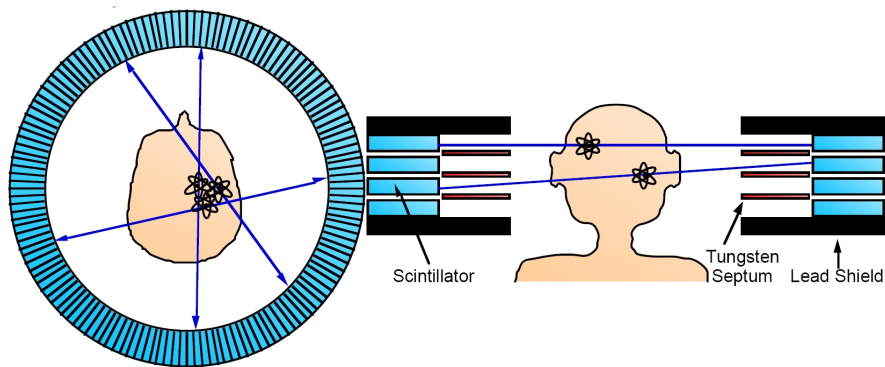
Figure 2.13: Schematic of a PET detector setup. The 511 keV photon pair from the positron- electron annihilation is detected in coincidence within a ring of photon detectors [48].

ClearPEM Sonic

The ClearPEM-Sonic [63] is a dual-modality PET/US scanner which includes a ClearPEM breast scanner [64] and an Aixplorer US system produced by Supersonic Imagine. The idea behind the project is the combination of the advantages of the different imaging modalities like ultrasound (US) and PET imaging. While the standard US imaging technique provides good real-time structural information of soft tissue without radiation, PET provides sensitive metabolic information.

Other Applications

Heavy inorganic scintillators have a wide range of applications. Apart from high energy physics and medical imaging, the can be seen in radiation monitoring systems, e.g. in nuclear power plants or other nuclear facilities. They are also used in homeland security applications, especially X-ray imaging applications at boarder or airport check points but also for the monitoring of radioactive material transports. Another big field of applications

is in material sciences where they are used as detectors for gamma rays coming from all kind of X-ray spectroscopy techniques. One common technique for example is the X-ray fluorescence (XRF) spectroscopy (but also energy dispersive x-ray spectroscopy (EDX, EDS) where the characteristic x-rays emitted from each element when bombarded with electrons or gamma rays is detected by a scintillator (usually sodium iodide doped with thallium, but also semiconductor or gas based detectors are used). The electron or gamma ray bombardment ejects electrons of the inner shell of the specimen, the electron hole is then filled by electrons of higher shells (usually K or L shell) and the energy difference of the electron between these two shells is emitted by the characteristic x-rays with the wavelength $\lambda = h \cdot c / E$. If the energy spectrum of these x-rays is plotted one gets specific lines for each element of the investigated sample. An example can be seen in Figure 2.14 where the EDX spectrum of the silicon nitride layer of one of our crystal samples was investigated.
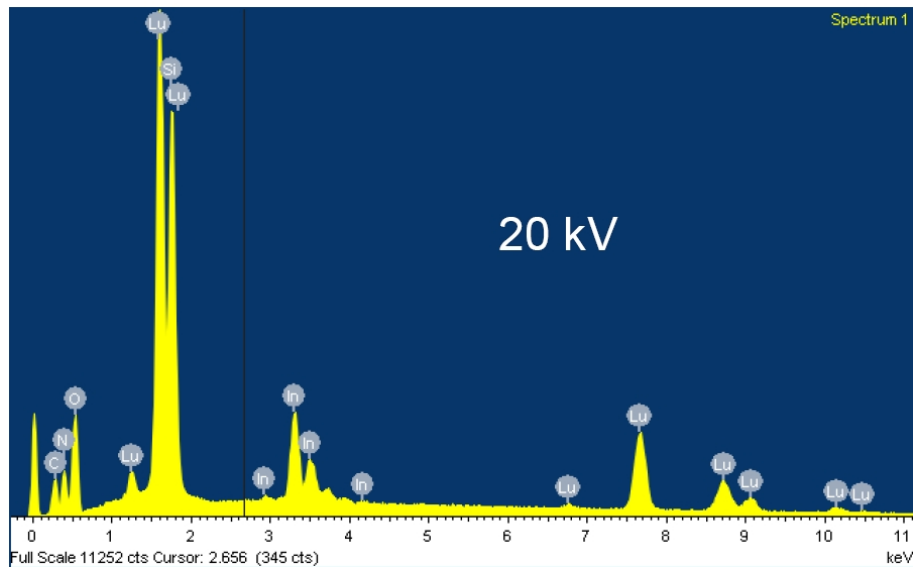
Figure 2.14: Energy dispersive x-ray spectroscopy (EDX) of the silicon nitride layer of one of our photonic crystal test samples. The $K\alpha$ and $K\beta$ lines (and 2nd orders of each of them) can be seen as the characteristic x-ray lines.

Chapter 3

The Theory of Photonic Crystals

Contents

3.1   Introduction into Photonic Crystals

Photonic Crystals (PhC) are natural or artificial materials which have a periodic arrange-
ment of different dielectric materials, in one, two, or three dimensions (see Figure 3.1).
The spatially arrangement hereby is in the range of the wavelength of the photon which
is wished to be manipulated. While PhC can be found in Nature in various forms (see
opals, butterfly wings [65] etc.) the first time PhCs were described in literature was in
1987 by Eli Yablonovitch [66] and Sajeev John [67]. Their intention was to develop a
material which shows similar effects on photons as semiconductors to electrons. While
Yablonovitch worked on the manipulation of spontaneous emission of electron transitions
in semiconductors, John worked on the localization of photons. In the meanwhile, many
other applications were arising but the basic principle of PhCs is always the same, light is
scattered at the interfaces where the index of refraction changes. The scattered waves can
now interfere constructively or destructively with each other. The stationary properties
of the light that is allowed to travel are called modes. While the modes of propagation

in a homogeneous medium are plane waves, the modes of a periodic medium are known as Bloch modes. A Bloch mode can be seen as a standing wave field produced by the multiple coherent scatterings of a wave by the periodic structures of a PhC lattice.

Under certain conditions band gaps (also called stop bands) can arise, which means that the formation of any modes is suppressed in the regarding energy range. To describe the modes of a PhC a band plot is usually used, which relates the energy of the photon against the wave vector of each photon.
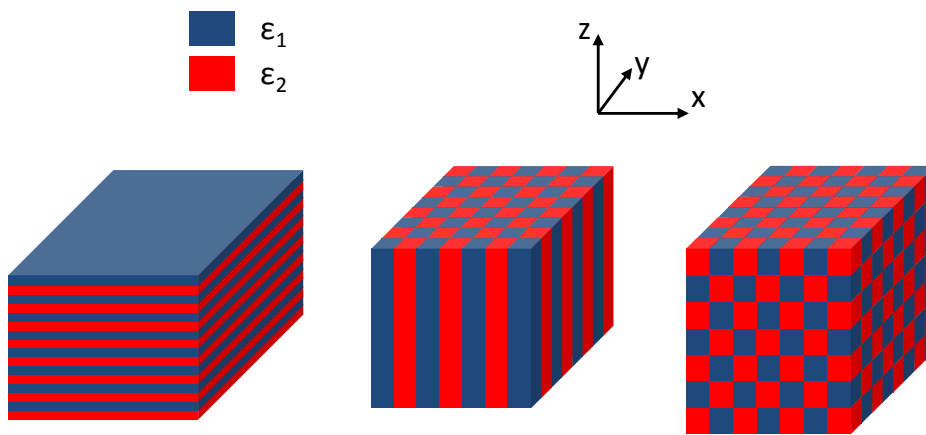
Figure 3.1: Principal layout of a one-, two- and three dimensional photonic crystal structure (from left to right).

3.1.1 One Dimensional Photonic Crystals

The simplest case of PhCs is the one dimensional crystal (see left picture in Figure 3.1). It shows periodicity only in one dimensions and uniformity in the transversal directions. According to the Fresnel equations a plane wave propagating perpendicular to the periodicity of the structure undergoes partial reflections every time the index of refraction changes. If the thickness of the structure is half the size of the wavelength in the according media the light will undergo destructive interference. This principle is known as the 1D Bragg condition and was exploited in dielectric mirrors long before the term photonic crystal emerged.

3.1.2 Two Dimensional Photonic Crystals

As the name indicates, it shows periodicity in two dimensions and uniformity in the third (see middle picture in Figure 3.1). Photonic crystal effects can therefore only be observed in the dimensions of the periodicity. Other than in the one dimensional case, in 2D PhCs two different polarization modes can be seen, transversal magnetic (TM-modes) and transversal electric modes (TE-modes). This is only valid as long as the wave propagates in the plane of the periodicity; if it propagates differently we have a mixture of the two polarizations.

3.1.3 Three Dimensional Photonic Crystals

The variation of the index of refraction in three dimensions (see right picture in Figure 3.1) allows also the manipulation of the light in all directions. The most prominent structures today are the woodpile [68] and the opal structure [69]. Since the 3D PhC is very challenging to manufacture, it is usually preferred to work with PhC slabs of 2D-PhC structures.

3.1.4 Photonic Crystal Slabs

Like discussed in the sections before, it is desired to have control of light in all three dimensions which is usually just achieved by three dimensional PhCs. Since the production of such structures is still very challenging, PhC slabs are a good compromise. PhC slabs consist of a layer of periodic structures in one- or two dimensions. The periodic structures are usually realized as air holes or air gaps within a high index of refraction material.

3.2 Electromagnetic Waves in Periodic Dielectric Media

3.2.1 Maxwell's Macroscopic Equations

The propagation of light in a photonic crystal can be described by the four macroscopic Maxwell equations. In a differential form and in SI units they are [70]:

$$\triangledown \cdot \mathbf{B} = 0 \qquad \triangledown \times \mathbf{E} + \frac{\partial \mathbf{B}}{\partial t} = 0 \tag{3.1}$$

$$\triangledown \mathbf{D} = \rho \qquad \triangledown \times \mathbf{H} - \frac{\partial \mathbf{D}}{\partial t} = \mathbf{J} \tag{3.2}$$

When we assume that free charges and electric currents are absent (ρ and $\mathbf{J} = 0$) and add the dependency of the position vector $\mathbf{r}$ and the time t we get the Maxwell equations in the form of Formulas 3.3 and 3.4:

$$\bigtriangledown \cdot \mathbf{B}(\mathbf{r},t) = 0 \qquad \bigtriangledown \times \mathbf{E}(\mathbf{r},t) = -\frac{\partial \mathbf{B}(\mathbf{r},t)}{\partial t} \tag{3.3}$$

$$\bigtriangledown \mathbf{D}(\mathbf{r},t) = 0 \qquad \bigtriangledown \times \mathbf{H}(\mathbf{r},t) = \frac{\partial \mathbf{D}(\mathbf{r},t)}{\partial t} \tag{3.4}$$

Where $\mathbf{r} = (x, y, z)^T$ which is the Cartesian position vector to describe a position of a point in space. To solve the Maxwell equations from Formula 3.4 one needs to relate the displacement $\mathbf{D}$ to the electric field $\mathbf{E}$ and the magnetic field density $\mathbf{B}$ to the magnetic field $\mathbf{H}$. This can be done by the constitutive equations which relate $\mathbf{D}$ to $\mathbf{E}$ 3.5 and $\mathbf{B}$ to $\mathbf{H}$ 3.6:

$$\mathbf{D}(\mathbf{r},t) = \epsilon_0 \epsilon(\mathbf{r})\mathbf{E}(\mathbf{r},t) + \mathbf{P}(\mathbf{r},t) \tag{3.5}$$

$$\mathbf{H}(\mathbf{r},t) = \frac{1}{\mu_0}\mathbf{B}(\mathbf{r},t) - \mathbf{M}(\mathbf{r},t) \tag{3.6}$$

The definition and regarding units of each symbol can be seen in 3.1. Without magnetic or anisotropic dielectric materials, the constitutive equations have the following form:

$$\mathbf{B}(\mathbf{r},t) = \mu_0 \mathbf{H}(\mathbf{r},t) \tag{3.7}$$

$$\mathbf{D}(\mathbf{r},t) = \epsilon_0 \epsilon(\mathbf{r})\mathbf{E}(\mathbf{r},t) \tag{3.8}$$

A summary of the definitions and units used in all the different Maxwell equations can be seen in tabular 3.1.

A PhC is made of several macroscopic regions where each region consists of a different homogeneous dielectric media. The permittivity ϵ_r and the permeability μ_r therefore vary with the position vector $\mathbf{r}$. In an ideal PhC ϵ_r and μ_r are periodic.

To further simplify the Maxwell equations, a set of assumptions can be made in the case of ideal photonic crystals:

1. It is assumed that there is no source inside the PhC, so we can set $\rho = 0$ and $\mathbf{J} = 0$

2. Within the PhC we just have weak radiation field strengths, which mean that the induced polarization of the medium remains proportional to the electric field.

Symbol	Meaning	SI Units
E	electric field	$\left[\frac{V}{m}\right]$
H	magnetic field	$\left[\frac{A}{m}\right]$
B	magnetic field density	$[T]$
D	electric flux density or displacement	$\left[\frac{C}{m^2}\right]$
P	polarization density	$\left[\frac{C}{m^2}\right]$
M	electric current density	$\left[\frac{V}{m^2}\right]$
J	electric current density	$\left[\frac{A}{m^2}\right]$
ϵ_0	permittivity of free space, constant	$\left[\frac{F}{m}\right]$
	(also dielectric constant)	
ϵ_r	relative electric permittivity	dimensionless
	(also relative dielectric constant)	
μ_0	permeability of free space, constant	$\left[\frac{H}{m}\right]$
μ_r	relative permeability	dimensionless

Table 3.1: Table definitions and units used in the Maxwell equations

3. The dielectric constant at position **r** and frequency ω ($\epsilon(r,\omega)$) does not depend on the light frequency ω therefore $\epsilon(r,\omega)$ reduces to $\epsilon(r)$.

4. The crystal is isotropic and macroscopic which means, that on a macroscopic scale, the index of refraction does not change. If needed, PhCs with anisotropic dielectric constants can be computed as well which was done in the work of [71].

5. There is no absorption in the PhC materials therefore $\epsilon(r)$ is always real.

Further we can relate **E** to **D** and **H** to **B** by the equations 3.8 and 3.7 respectively. With all this assumptions in place the maxwell equations (3.1) become:

$$\bigtriangledown \cdot \mathbf{H}\left(\mathbf{r}, t\right) = 0 \tag{3.9}$$

$$\bigtriangledown \times \mathbf{E}\left(\mathbf{r}, t\right) + \mu_0 \frac{\partial \mathbf{H}\left(\mathbf{r}, t\right)}{\partial t} = 0 \tag{3.10}$$

$$\bigtriangledown \left[\epsilon\left(\mathbf{r}\right) \mathbf{E}\left(\mathbf{r}, t\right)\right] = 0 \tag{3.11}$$

$$\bigtriangledown \times \mathbf{H}\left(\mathbf{r}, t\right) - \epsilon_0 \epsilon\left(\mathbf{r}\right) \frac{\partial \mathbf{E}\left(\mathbf{r}, t\right)}{\partial t} = 0 \tag{3.12}$$

When $\mathbf{E}\left(\mathbf{r}, t\right)$ or $\mathbf{H}\left(\mathbf{r}, t\right)$ in Formula 3.10 or Formula 3.12 gets eliminated by substitution into each other we get Formula 3.17 and 3.18. As an example, the derivation is shown for Formula 3.17: First, the Equation 3.12 gets divided by $\epsilon\left(\mathbf{r}\right)$:

$$\frac{1}{\epsilon\left(\mathbf{r}\right)} \bigtriangledown \times \mathbf{H}\left(\mathbf{r}, t\right) = \epsilon_0 \frac{\partial \mathbf{E}\left(\mathbf{r}, t\right)}{\partial t} \tag{3.13}$$

Second, the curl of it is calculated:

$$\bigtriangledown \times \left(\frac{1}{\epsilon\left(\mathbf{r}\right)} \bigtriangledown \times \mathbf{H}\left(\mathbf{r}, t\right)\right) = \epsilon_0 \frac{\partial}{\partial t} \bigtriangledown \times \left(\mathbf{E}\left(\mathbf{r}, t\right)\right) \tag{3.14}$$

Then Equation 3.10 is inserted into it which results in:

$$\bigtriangledown \times \left(\frac{1}{\epsilon\left(\mathbf{r}\right)} \bigtriangledown \times \mathbf{H}\left(\mathbf{r}, t\right)\right) = -\epsilon_0 \mu_0 \frac{\partial^2}{\partial t^2} \mathbf{H}\left(\mathbf{r}, t\right) \tag{3.15}$$

Finally we can get rid of $\epsilon_0 \mu_0$ by substituting $\frac{1}{c^2}$ for it which can be derived from Formula 3.16 which states that the light velocity in free space can also be defined as the inverse of the square root of the permittivity of free space and the permeability of free space. The result will be an equation entirely defined by $\mathbf{H}\left(\mathbf{r}, t\right)$ (see Formula 3.17). An according derivation of Formula 3.10 and Formula 3.12 leads to an equation which is defined only by $\mathbf{H}\left(\mathbf{r}, t\right)$ (see Formula 3.18).

$$c = \frac{1}{\sqrt{\varepsilon_0 \mu_0}} \tag{3.16}$$

$$\bigtriangledown \times \left(\frac{1}{\epsilon\left(\mathbf{r}\right)} \bigtriangledown \times \mathbf{H}\left(\mathbf{r}, t\right)\right) = -\frac{1}{c^2} \frac{\partial^2}{\partial t^2} \mathbf{H}\left(\mathbf{r}, \mathbf{t}\right) \tag{3.17}$$

$$\frac{1}{\epsilon\left(\mathbf{r}\right)} \bigtriangledown \times \left(\bigtriangledown \times \mathbf{E}\left(\mathbf{r}, t\right)\right) = -\frac{1}{c^2} \frac{\partial^2}{\partial t^2} \mathbf{E}\left(\mathbf{r}, \mathbf{t}\right) \tag{3.18}$$

In this set of equations the electric field $\mathbf{E}$ and the magnetic field $\mathbf{H}$ are linear functions of space and time. By expanding the field into a set of harmonic modes we can separate the time and spatial dependence. By employing a complex valued field we can write a harmonic mode as a spatial pattern times a complex exponential:

$$\mathbf{H}(\mathbf{r}, t) = \mathbf{H}(\mathbf{r}) e^{-j\omega t}$$
$$\mathbf{E}(\mathbf{r}, t) = \mathbf{E}(\mathbf{r}) e^{-j\omega t} \tag{3.19}$$

Inserting the equations 3.19 into 3.9 - 3.12we get for the two divergence equations:

$$\bigtriangledown \cdot \mathbf{H}(\mathbf{r}) = 0 \tag{3.20}$$
$$\bigtriangledown [\epsilon(\mathbf{r}) \mathbf{E}(\mathbf{r})] = 0 \tag{3.21}$$

And the two curl equations become:

$$\bigtriangledown \times \mathbf{E}(\mathbf{r}) - j\omega\mu_0 \mathbf{H}(\mathbf{r}) = 0 \tag{3.22}$$
$$\bigtriangledown \times \mathbf{H}(\mathbf{r}) + j\omega\epsilon_0\epsilon(\mathbf{r}) \mathbf{E}(\mathbf{r}) = 0 \tag{3.23}$$

Now we derive a formula entirely in $\mathbf{H}(\mathbf{r}, t)$ or in $\mathbf{E}(\mathbf{r}, t)$ like we did before to get Formula 3.17 and Formula 3.17. By dividing equation 3.23 by $\epsilon(\mathbf{r})$ and take the curl of it and then use equation 3.22 to get rid of $\mathbf{E}(\mathbf{r})$ we can decouple the magnetic from the electric field. Also the permittivity and permeability of free space can be expressed by the speed of light in vacuum (see Formula 3.16). This would give us an equation entirely described by the magnetic field (see Formula 3.24) or electric field (see Formula 3.25).

$$\bigtriangledown \times \left(\frac{1}{\epsilon(\mathbf{r})} \bigtriangledown \times \mathbf{H}(\mathbf{r}) \right) = \left(\frac{\omega}{c} \right)^2 \mathbf{H}(\mathbf{r}) \tag{3.24}$$

$$\frac{1}{\epsilon(\mathbf{r})} \bigtriangledown \times (\bigtriangledown \times \mathbf{E}(\mathbf{r})) = \left(\frac{\omega}{c} \right)^2 \mathbf{E}(\mathbf{r}, \mathbf{t}) \tag{3.25}$$

Formula 3.26 and Formula 3.27 which are derived from Formula 3.10 and Formula 3.12

can now be used to recover either the magnetic or the electric modes from one of the two equations 3.24 and 3.25.

$$\mathbf{E}\left(\mathbf{r}\right) = \frac{j}{\omega\epsilon_0\epsilon\left(\mathbf{r}\right)} \bigtriangledown \times \mathbf{H}\left(\mathbf{r}\right) \tag{3.26}$$

$$\mathbf{H}\left(\mathbf{r}\right) = -\frac{j}{\omega\mu_0} \bigtriangledown \times \mathbf{E}\left(\mathbf{r}\right) \tag{3.27}$$

The eigenvalue problem in the two equations 3.24 and 3.25 is also known as the Helmholtz equation. The solution of these Helmholtz equations for a given periodic structure $\epsilon(r)$ is a set of modes for each given frequency which can be plane waves of the form:

$$\mathbf{H_k}\left(\mathbf{r}\right) = \mathbf{H_0}\left(\mathbf{r}\right)e^{-i\mathbf{k}\cdot\mathbf{r}} \tag{3.28}$$

Where the wavevektor $\mathbf{k}$ is indicating the propagation direction. A closer look on the computation of the Eigen modes of a PhC is given in the next chapter.

3.3 Eigenmodes of a Photonic Crystal - Photonic Bands

3.3.1 Wave Equations and Eigenvalues

A PhC can be seen as a periodic dielectric function of the form $\varepsilon(\boldsymbol{r}) = \varepsilon(\boldsymbol{r} + a_{1,2,3})$ where $\boldsymbol{r}$ is a Cartesian position vector and $a_{1,2,3}$ are the primitive lattice vectors (see Chapter 3.3.2 about the reciprocal lattice). Due to the spatial periodicity, we can expand $\varepsilon(\boldsymbol{r})$ into a Fourier series. For this we have to introduce the primitive reciprocal lattice vectors $b_{1,2,3..}$ and the reciprocal lattice vectors G:

$$\frac{1}{\varepsilon(\mathbf{r})} = \sum_{\mathbf{G}} \kappa(\mathbf{G})e^{i\mathbf{G}\cdot\mathbf{r}} \tag{3.29}$$

Like shown in chapter 3.2.1 the wave equation for magnetic fields $\mathbf{H}\left(\mathbf{r}\right)$ (3.24) describes the harmonic modes in a mixed dielectric medium. This formula can now also be seen as an eigenvalue problem in the form of $\mathbf{T}x = \lambda x$. The eigen-operator $\mathbf{T}$ would be a differential operator which takes the curl, divides by $\epsilon\left(\mathbf{r}\right)$, and then takes the curl again:

$$\mathbf{T}\left(\mathbf{H}\left(\mathbf{r}\right)\right)\widehat{=}\bigtriangledown \times \left(\frac{1}{\epsilon\left(\mathbf{r}\right)}\bigtriangledown \times \mathbf{H}\left(\mathbf{r}\right)\right) \tag{3.30}$$

Equation 3.24 formulated as an eigenvalue problem would then look like that:

$$\mathbf{T}\left(\mathbf{H}\left(\mathbf{r}\right)\right) = \left(\frac{\omega}{c}\right)^2 \mathbf{H}\left(\mathbf{r}\right) \tag{3.31}$$

The eigenvectors $\mathbf{H}\left(\mathbf{r}\right)$ are the harmonic modes. The multiplicative constant $\left(\frac{\omega}{c}\right)^2$ in Formula 3.31 are eigenvalues which are proportional to the square of the frequency of the harmonic modes $\mathbf{H}\left(\mathbf{r}\right)$. The Bloch-Floquet theorem[*] for periodic media [72] defines now that the wave equation (Equ. 3.24) can be written as:

$$\mathbf{E}\left(\mathbf{r}\right) = \mathbf{E}_{\mathbf{n}\boldsymbol{k}}\left(\mathbf{r}\right) = e^{i\boldsymbol{k}\mathbf{r}}\mathbf{u}_{\mathbf{n}\boldsymbol{k}}\left(\mathbf{r}\right) \tag{3.32}$$

$$\mathbf{H}\left(\mathbf{r}\right) = \mathbf{H}_{\mathbf{n}\boldsymbol{k}}\left(\mathbf{r}\right) = e^{i\boldsymbol{k}\mathbf{r}}\mathbf{v}_{\mathbf{n}\boldsymbol{k}}\left(\mathbf{r}\right) \tag{3.33}$$

Here, $\mathbf{E}\left(\mathbf{r}\right)$ and $\mathbf{H}\left(\mathbf{r}\right)$ are characterized by the wave vector $\mathbf{k}$ which lies within the first Brillouin zone (BZ) and a band index n. $\mathbf{u}_{\mathbf{n}\boldsymbol{k}}$ and $\mathbf{v}_{\mathbf{n}\boldsymbol{k}}$ are periodic vectorial functions which satisfy the relationship of the periodic lattice:

$$u_{nk}(r + a_i) = u_{nk}(r) \tag{3.34}$$

$$v_{nk}(r + a_i) = v_{nk}(r) \tag{3.35}$$

$\mathbf{E}\left(\mathbf{r}\right)$ and $\mathbf{H}\left(\mathbf{r}\right)$ from 3.32 and 3.33 can be expanded into a Fourier series just like we did with $\epsilon^{-1}(r)$ in 3.29:

$$E_{kn}(\mathbf{r}) = \sum E_{kn}(\mathbf{G})e^{i(k+\mathbf{G})\cdot\mathbf{r}} \tag{3.36}$$

$$H_{kn}(\mathbf{r}) = \sum H_{kn}(\mathbf{G})e^{i(k+\mathbf{G})\cdot\mathbf{r}} \tag{3.37}$$

---

[*]Same as Bloch's theorem for a wavefunction of a particle placed in a periodic potential

$E_{kn}(\mathbf{G})$ and $H_{kn}(\mathbf{G})$ are the expansion coefficients in the reciprocal space. By substituting equation 3.37 and 3.29 into 3.25 we get the eigenvalue equations for the expansion coefficients $H_{kn}(\mathbf{G})$:

$$-\sum_{G'} \kappa(\mathbf{G} - \mathbf{G}')(k + \mathbf{G}) \times \left\{(k + \mathbf{G}') \times (H_{kn}(\mathbf{G}')\right\} = \left(\frac{\omega_n(k)}{c}\right)^2 \mathbf{H}_{kn}(\mathbf{G}) \qquad (3.38)$$

To obtain the expansion coefficients for $E_{kn}(\mathbf{G})$ the technique is similar and can be looked up in [73]. This method is called the plane wave expansion method (PWE). In numerical calculations, the summation in the equation for $H_{kn}(\mathbf{G})$ 3.38 are calculated until a sufficiently large number of $\mathbf{G'}$ and then the eigenvalue problem for each wavevektor $\mathbf{k}$ is solved.

The discrete eigenvalues $\omega_n(\boldsymbol{k})$ indicated by $n = 1, 2, 3..$ are continuous functions of $\boldsymbol{k}$. When $\omega_n(\boldsymbol{k})$ is plotted versus the wave vector $\boldsymbol{k}$ we get the band- or dispersion diagram of the regarding PhC structure (see band diagram in 3.3.3). The Eigen solutions are periodic functions of $\boldsymbol{k}$ which means that the solution for $\boldsymbol{k_1}$ is the same as for $\boldsymbol{k_1} + G$ where G is the is the primitive reciprocal lattice vector as mentioned before. Due to this periodicity only the Eigen solutions for $\boldsymbol{k}$ within the primitive cell of this reciprocal lattice has to be computed. This region is also called the first Brillouin zone and is explained in the next Chapter (see 3.3.2).

3.3.2 The Reciprocal Space and the Brillouin zone

In solid state physics, a lattice is often represented as a reciprocal lattice (RL) which is the Fourier transform of the spatial function of the original lattice. The Brillouin zone (BZ) is a primitive cell in reciprocal space where the boundaries are defined by planes related to points on the reciprocal lattice (see Figure 3.2 and Figure 3.3). The high symmetry points within the BZ are labelled according to Table 3.2. The reciprocal lattice vectors of the two PhC patterns used in this work can be calculated according to the formulas shown in Tabular 3.3. In photonics, but also in solid state physics, the BZ description in is important since a periodic structure can be completely characterized by just looking into the solutions of the first Brillouin zone. Wave vectors outside the BZ are folded by the edges of the BZ and can be therefore represented by a wave vector inside the BZ again.

.

Table 3.2: Critical points of the first Brillouin zone of a reciprocal lattice which are points of high symmetry and are therefore of special interest in photonics and solid state physics [74].

Symbol	Description
Γ	Center of the Brillouin zone
M	Center of an edge
X	Center of a face
K	Middle of an edge joining two rectangular faces

.

Table 3.3: Transformation of the reciprocal lattice vectors for two dimensional square and triangular patterns. $\hat{x}$ and $\hat{y}$ are the independent lattice vectors and a is the lattice constant.

	Real Lattice	Reciprocal Lattice	RL length
Square lattice	$\boldsymbol{a}_1 = a\hat{x}$	$\boldsymbol{b}_1 = (2\pi/a)\hat{x}$	$2\pi/a$
	$\boldsymbol{a}_2 = a\hat{y}$	$\boldsymbol{b}_2 = (2\pi/a)\hat{y}$	
Triangular lattice	$\boldsymbol{a}_1 = a\hat{x}$	$\boldsymbol{b}_1 = (2\pi/a)(\hat{x} - \sqrt{3}/3\hat{y})$	$4\pi/(a\sqrt{3})$
	$\boldsymbol{a}_2 = (\hat{x} + \sqrt{3}\hat{y})$	$\boldsymbol{b}_2 = (4\pi/a)(\sqrt{3}/3)\hat{y}$	
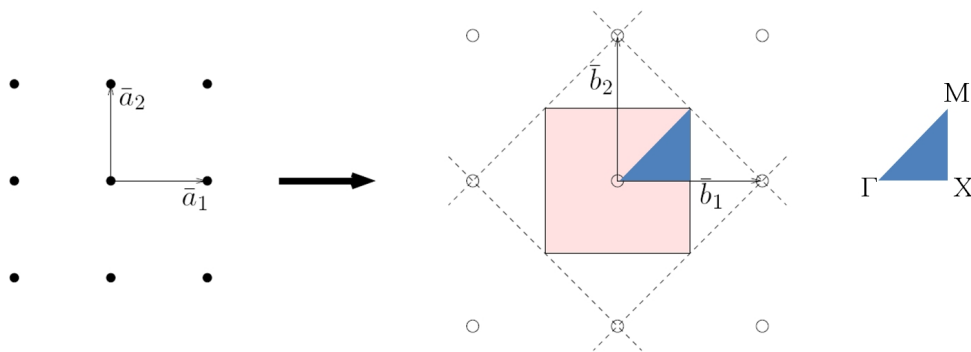
Figure 3.2: Square lattice and corresponding reciprocal lattice with highlighted Brillouin zone (red). The blue area is the irreducible first BZ with the corners M, K and X.
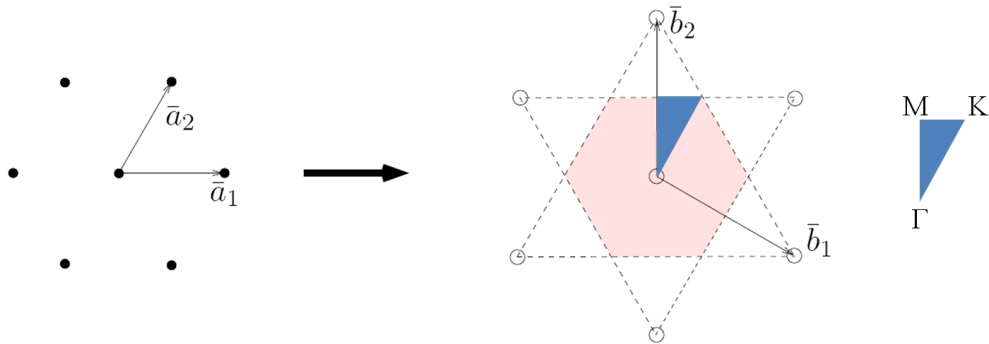
Figure 3.3: Triangular lattice and corresponding reciprocal lattice with highlighted Brillouin zone (red). The blue area is the irreducible first BZ with the corners M, K and Γ.

3.3.3 Band Diagrams

The discrete eigenvalues $\omega_n(\boldsymbol{k})$ indicated by $n = 1, 2, 3..$ are continuous functions of $\boldsymbol{k}$. When $\omega_n(\boldsymbol{k})$ is plotted versus the wave vector $\boldsymbol{k}$ we get the band- or dispersion diagram of the regarding PhC structure. Therefore the band diagram relates the photon energies $\omega(k)$ of each mode to the corresponding propagation direction k. For a 2D-PhC with triangular holes of air in silicon nitride (IR=1.85) with infinite extension in the z-direction the band diagram looks like shown in Figure 3.4. The PhC pattern structure used in this plot can be seen in 3.3. The hole diameter was chosen to be $0.3a$ and the index of refraction of the substrate is 1.85 (silicon nitride) just like the pattern used in one of our samples (pattern Nr. p1, see Chapter 6). The fields in a 2D PhC structure can be divided into two polarizations: TM (transverse magnetic) and TE (transverse electric). In the TM mode the magnetic field is in the xy plane and the electric field is perpendicular to z and in the TE mode, the electric field is in the plane and the magnetic field is perpendicular to z. In reality, the thickness of the PhC structure is limited. PhC structures with finite thickness are called photonic crystal slabs or planar photonic crystals. The finite thickness introduces some different behaviours to the PhC and therefore a PhC slab cannot be treated as a purely two dimensional PhCs. If we take the example of Figure 3.4 and limit the thickness to $1.6a$ the modes look different (see Figure 3.5). In this plot, the modes are categorized in even and odd modes instead of TE and TM modes. The reason for that is that modes are not completely parallel or vertical when going away from the $z = 0$ plane. But due to the continuity of fields, even modes are mostly TE and odd modes are mostly TM and are therefore also called TE-like and TM-like modes respectively [76].
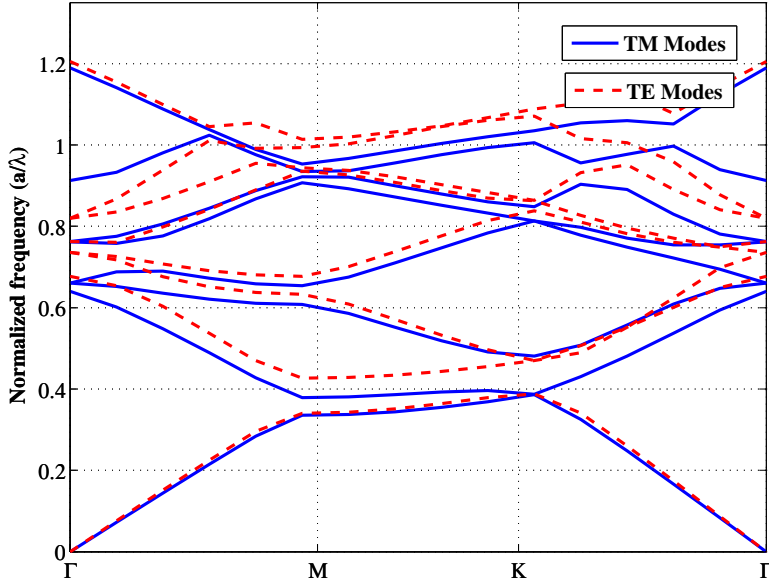
Figure 3.4: Band diagram of a 2D triangular PhC with a hole diameter of $0.3a$ and an index of refraction of the substrate of 1.85 (silicon nitride). The bands are calculated with the help of the MPB package [75]

The green solid line in Figure 3.5 represents the light line. The light line indicates the boarder to the light cone ($\omega \geqslant ck_{||}$) which is the region where modes can irradiate into air. In air (or vacuum) this relation is simply $\omega(k) = k_0 c$. Modes in that region are also called leaky since they "leak" into the ambient medium. The principle of photonic crystal light extraction enhancement in this work is based on leaky mode optimization. There exists also a second effect which supports extraordinary light extraction due to photonic band gaps (called band gap effect, for more details see references [77] and [78]), but the effect is negligible in this work since the low index of refraction contrast of our samples (silicon nitride/air - 1.85/1.0) does not favor complete band gaps. Therefore, all modes which can be seen above the light line (in the grey shaded region) lose their energy to the background and are therefore radiation modes (or leaky modes). The band diagrams in this work are calculated using the freely available MIT Photonic-Bands (MPB) tool which is a software package released under the GPL (GNU General Public) license. The MPB software calculates Eigen states and eigenvalues of the Maxwell equations in the frequency domain. For that it applies a Fourier transform over an infinite repetition of the unit-
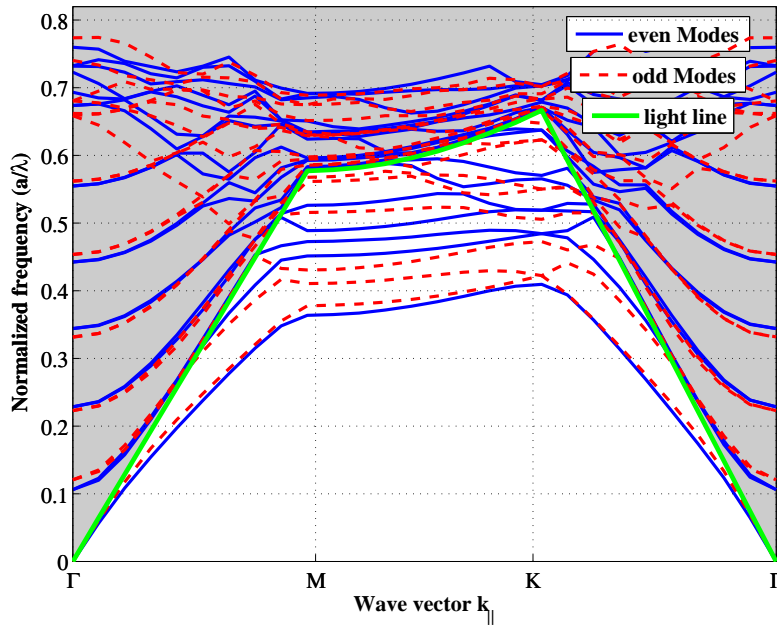
Figure 3.5: Band diagram of a triangular PhC slab with a hole diameter of $0.3a$, a thickness of $1.6a$ and an index of refraction of the substrate of 1.85 (silicon nitride). The 18 bands are calculated with the MPB software package [75]. The pattern parameters are according to the PhC design p1 (see Chapter 6). P1 has a lattice constant of $a = 280nm$ which results in a normalized frequency of 0.66 at an emission wavelength of $420nm$. It can be seen, that a large fraction of the modes are placed above the light line which means that they can radiate into the ambient air.

cell (smallest entity of the PhC pattern) in all three directions to avoid discontinuities. For three dimensional problems like the PhC slab we are using, this can introduce some problems since the unit-cell is not repeated in the z-direction. For PhC slabs, MPB can therefore only calculate the guided modes (below the light line) with high accuracy. As a solution, the unit cell size is extended into the z direction by several lattice constants $(3-8a)$ which reduces the influence of the z-periodicity on the leaky modes to a negligible amount [79].

3.4   Light Diffraction by PhC Gratings

When describing the incident light with the wave vector k_i having the length $|k_i| = n_i k_0$ where k_0 is the vacuum vector length $k_0 = 2\pi/\lambda_0$, Snell's law is equivalent to the conservation of the length of the in-plane k vector $k \parallel$ which is the vacuum vector multiplied by the index of refraction of the regarding material: $|k_\parallel| = n k_0$. Therefore only light with an in-plane k vector length smaller than $k_0 n_{cry} sin\Theta_C = n_{amb} k_0$ can radiate into the ambient medium (see Figure 3.6).
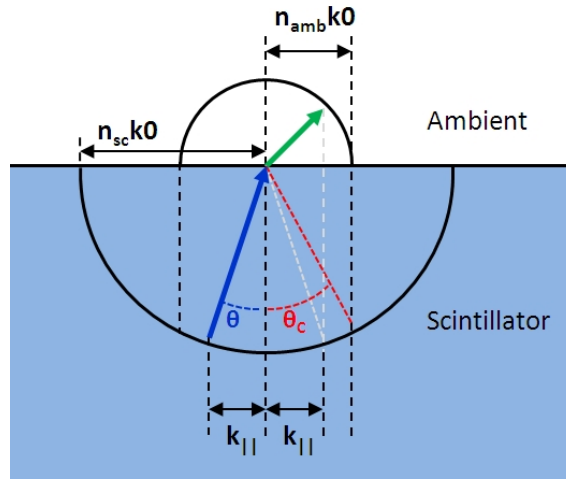
Figure 3.6: K-vector diagram of a scintillator/ambient interface. Due to Snell's law, light can only escape the crystal when the angle is smaller than the critical angle $\Theta < \Theta_c$. Snell's law can also be derived from the conservation of the in-plane vector $k_{/parallel}$ which is the k-vector component parallel to the interface. The vacuum vector length is $K_0 = 2\pi/\lambda_0$ which does not change in the case of air. In the diagram we can see that for light in the ambient medium $k_{/parallel}$ cannot get bigger than $n_{amb} k_0$ and therefore light having a bigger angle than Θ_c will be internally reflected.

To overcome this limit, a theoretical investigation of photonic crystal structures as diffraction gratings on top of scintillators was reviewed in the work of [13][17][80]. Photonic crystals are a periodic arrangement of two different materials in one-, two- or three dimensions. In the present work, two dimensional PhC structures are used for the light yield improvement on heavy inorganic scintillators (HIS). The measurements and simulations are based on an actual sample which has been produced in cooperation with the Lyon Institute of Nanotechnology (INL). The photonic crystal slab on top of our scin-

tillator operates as a diffraction grating. That means, that the photonic crystal "Bragg scatters" the light out of the scintillator, leading to higher extraction efficiencies [14]. A two dimensional PhC structure can be described by its reciprocal lattice vectors G_i. The reciprocal lattice vector G can be derived by Fourier transformation of the real lattice (see Figure 3.7) where the length of it is defined as $G_0 = 2\pi/a$ for a triangular pattern. These vectors couple light wave propagation in the photonic crystal and the resulting mode is called a Bloch mode [81] which is a linear combination of in-plane harmonic waves. The diffraction condition to air is then described as $|k_\parallel + nG| < k_0$. The main harmonic ($k_\parallel$) couples to other harmonics by the reciprocal lattice vector G, if the resulting vector ($k_\parallel + nG$) lies within the air circle (radius $= k_0$), the mode propagates into air and is called leaky [12] (see Figure 3.8). The integer n determines which harmonic is responsible for the diffraction. Looking to these modes in a dispersion diagram (also called band diagram), light diffraction can be explained as modes who exist above the light line [82]. A dispersion diagram relates the photon energies $\omega(k)$ to the corresponding propagation direction k. In air (or vacuum) this relation is simply $\omega(k) = k_0 c$ which is called the light line when plotted in the dispersion diagram (see Chapter 3).

a   b
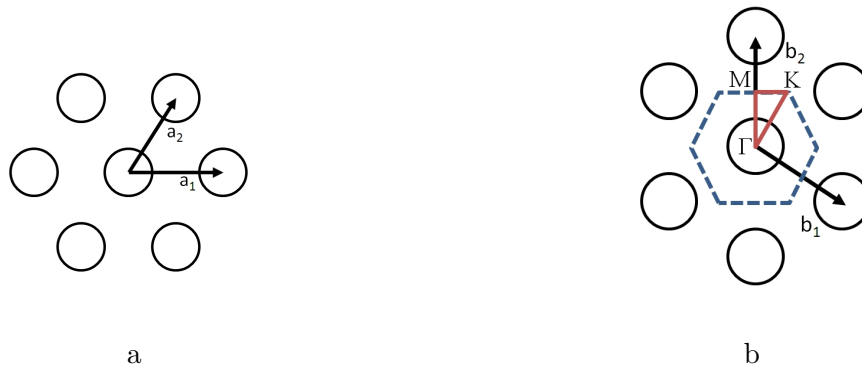
Figure 3.7: The real lattice (a) of the triangular PhC pattern with the lattice vectors $a1$ and $a2$ which vector length is the lattice constant a. In (b) the reciprocal lattice of the same structure can be seen. The length of b1 and b2 can be calculated as: $|b| = 2\pi/a$. The dashed hexagon represents the Brillouin zone and the red triangle the irreducible Brillouin zone.
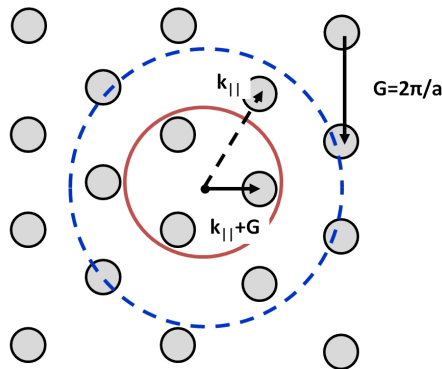
Figure 3.8: Ewald construction for a Bloch mode diffracted in the PhC slab. Light within the crystal having an in-plane wave vector $k_\parallel$ (dashed pointer) cannot couple to the ambient air because its in-plane k-vector lies outside the air circle (red solid circle, radius = $n_{air}k_0$). Due to the presence of the periodic grating, the light can couple along the reciprocal lattice points to other harmonics (solid pointer). If the resulting vector lies within the air circle, the mode radiates into air (compare diffraction condition to air: $|k_\parallel + nG| < k_0$).

3.5   Summary

This chapter deals with the mathematical description of electromagnetic waves in periodic media as it is the case for photonic crystals. Photonic crystal structures are able to change the laws of light diffraction at an interface of two materials of different index of refraction. In our case we want to extract light out of a crystal which is otherwise reflected by total internal reflection. The theoretical description in this chapter shows that the periodic arrangement of materials in a PhC slab can lead to the formation of harmonic modes. If these modes are superposed to the incoming wave it can lead to increased light extraction of otherwise partially or totally reflected photons. The modes within a PhC can be calculated by solving the Maxwell equations for electromagnetic waves in periodic media. The Ewald construction shows pictorially how an incoming wave can be refracted towards the outside of a crystal by the means of Bloch modes which exists within the PhC slab.

Chapter 4

Heavy Inorganic Scintillator Modelling

Contents

In this chapter, an approach to model the heavy inorganic scintillators (HIS), which are later used for our photonic crystal samples, is introduced. The exact knowledge of the path a photon takes from its birth until absorption or detection is of great importance for the optimization of the light extraction of a scintillating crystal, especially if one wants to see the effect of a photonic crystal grating. In general, the properties of absorption and diffusion of a scintillator have the largest influence on the way light propagates. These parameters can be specified with the absorption and diffusion length ($\lambda_{abs}, \lambda_{diff}$) which specifies the length (in this work always measured in cm) where $1 - e^{-1}$ or 63% of the light is absorbed or diffused respectively. In addition, the surface of the scintillator has to be treated differently due to a certain roughness of the sidewalls and edges of the scintillator which leads to additional diffusion and altered reflection and transmission. Because most of these parameters could not be measured directly on our crystal samples, we followed an indirect measurement technique. This so called model fitting (or matching) approach is using a Monte Carlo model of the scintillator and compares a directly measurable quan-

tity (usually the light yield) of a real world sample to the simulated values of the same crystal configuration (see also [2] and [38]). The unknown parameters of the model are then changed within a certain range until the simulation model gives the best fit to the measured values of each of the investigated crystal arrangements. For this technique it is important, that the number of different crystal configurations (different sized sidewalls, different outcoupling medium, different wrapping) is larger than the number of unknown parameters to avoid over-fitting. In our case we had a LSO crystal with the dimensions of $2.6 \times 1.2 \times 7mm^3$ which gave us three different sized side walls where a different light yield could be obtained. In addition, we used three different contact agents for the optical connection between the scintillator and the photomultiplier tube which gave us nine different crystal configurations. The measured light yield of these nine configurations was then compared to the light yield of the according simulation to narrow down the unknown parameters.

4.1   The Monte Carlo Model-Matching Technique

For the design and optimization of heavy inorganic scintillator (HIS) based detector systems, simulation tools are becoming more and more important. Experimental optimization techniques are usually expensive and time consuming since they involve several iterations of crystal growing, cutting, polishing and measuring. Simulating the properties of a scintillator with a Monte Carlo (MC) program on the other hand is a cheap alternative and is therefore used a lot in the research and development of scintillation based detector systems. But there are limits to the accuracy and reliability of MC simulations since there are still a lot of unknown components in the whole HIS based detector setup. In [38] the difficulties for HIS Monte Carlo simulations are due to the following four points:

1. The high index of refraction (IOR). Due to the high IOR ($n > 1.8$) a large part of the light is trapped inside the crystal by total internal reflections (TIR). Therefore the condition and the properties of the surface (roughness, edge damages and scratches) can make a significant effect on the light output of the scintillator. All these inhomogeneities are hard to determine and therefore a problem when one wants to model such a setup.

2. Wrapping or depolishing. For a better light output, HIS are usually wrapped in a diffusing or reflecting material and in addition some of the sidewalls can be depolished. Depolished surfaces and manually applied wrappings are introducing a number of

unknown parameters and uncertainties to the HIS model and this is therefore hard to simulate [83] [84].

3. Anisotropy. A number of scintillating crystals are showing an anisotropic behaviour, which means that the index of refraction, absorption and scattering will be dependent on the direction of the light inside the crystal. Even though modern simulation tools (like LITRANI) can handle anisotropy until a certain level, the problem of measuring the right anisotropic parameters and the crystal lattice orientation still remains.

4. Scattering. Light scattering in HIS are caused by lattice distortions or impurities of the crystal. The simulation requires knowledge of the exact scattering coefficient which is difficult to measure directly.

Due to all these problems, the usual approach in HIS MC simulations is a model matching technique. For the model matching one tries to simplify the experimental setup as much as possible to avoid all sources of uncertainties and states which cannot be reproduced by the MC program. Then, several measurements are performed with one well understood and controllable parameter changing in each measurement. The resulting light yields are then compared to the MC simulation model which is undergoing the same change of the setup for each run. The unknown and/or uncertain parameters of the simulation are then adapted until the measurement and simulation results of all runs fit together. In [2] and [38] this approach was used to determine the light collection efficiency η and the associated absolute light yield. In [38] the different measurements were performed by changing the index of refraction of the coupling media between the crystal and the PMT window and in [2] the orientation and the wrapping changed in addition.

4.2 The LITRANI Simulation Program

4.2.1 Monte Carlo Computer Simulations

Monte Carlo computer simulations are named after the gambling city Monte Carlo because they are calculations based on random numbers, similar to games of chance. The interactions of radiation with matter occur randomly but the interactions occur with known probabilities. A computer simulation which takes these probabilities into account can

simulate individual radiation events and also the excitation, light emission and light prop-
agation of a scintillator. A Simulation with a large number of events can give a precise
prediction of the parameters of the modelled system. In this work the LITRANI Monte
Carlo computer simulations is used to study the light yield and angular distribution of
heavy inorganic scintillators and the effects of wrapping and optical contact materials. In
addition it is used for the model matching technique to discriminate parameters of the
crystal which cannot be measured otherwise.

4.2.2 Basic Characteristics of LITRANI

LITRANI [85] is a Monte-Carlo program based on ROOT [86]. In this work the newest
version of LITRANI was used called SLITRANI which stands for "'Super LIght TRans-
mission in ANIsotropic media"'. Any three dimensional setup which can be described
by the TGeo [86] class of ROOT can be used as a setup in SLITRANI. Each volume
can be of a different material and each material can have a different dielectric constant,
absorption length and diffusion length which may be dependent on the wavelength. In
addition, wavelength shifting and Rayleigh scattering can be simulated. In contrast to
other Monte Carlo light ray tracing programs, LITRANI can use an anisotropic dielectric
constant and absorption length. To produce photons in SLitrani one has various possi-
bilities: spontaneous emission of photons, photons coming from an optical fibre, photons
generated by ionizing particles, photons generated by gamma rays of energy of 0.1 to 1
MeV or photons generated by an high energy electromagnetic shower. As detectors one
can have any volume and material inside the setup. In general all photons are tracked
until they are absorbed or detected. In addition several photon statistics are recorded like
the amount, arrival time, wavelength and material of absorption or reflection.

4.2.3 Self-build Extensions to LITRANI

Angular distribution:
The standard version of SLITRANI does not record the angle of the photon at each
interface. Since the angular distribution is of special interest for our purpose, we changed
the source code in a way to keep track of the angle incoming and outcoming of an interface
which is of interest. Since we assume random polarization we just store the angle between
the normal vector of the surface and the traveling path of the photon.

    Full access to photon statistics:
For a better understanding of all the factors influencing the light distribution, reflection,

absorption and output, we introduced a variable into the source code which stores the information of birthplace, initial emission angle, number of reflections from the wrapping and number of reflections at the out-coupling interface. The variable can be accessed after the simulation for analysis, plotting or debugging.

Additional Light Extraction due to Rough Surfaces:
LITRANI can model an arbitrary combination of specular and diffuse reflection at any interface of two different materials. In the case of rough surfaces, diffusion may not always be a sufficient model to describe the light propagation correctly since the not perfectly flat surfaces of a scintillator are also showing some additional diffraction effects resulting from random phase variations induced by reflections from micro-topographic surface features [87][88] [89]. In the self-build LITRANI extension, an additional parameter can be chosen for each interface to enable additional light extraction of rough surfaces.

Photonic Crystal Light Extraction:
The photonic crystal induced light extraction cannot be simulated by the LITRANI program. Therefore the reflection properties of a PhC structure are calculated with special PhC software (see Chapter 5). The resulting reflection properties are then implemented as a look-up table into LITRANI.

4.3   Model Optimization

4.3.1   The LITRANI Setup
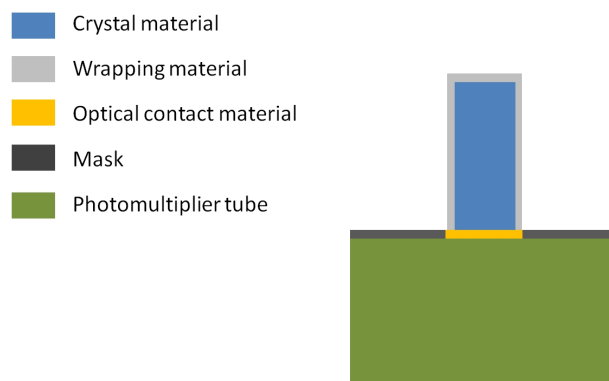
Figure 4.1: The schematics of a general setup of a standard light yield measurement. The LITRANI model is based on our light yield bench which is using a PMT XP2262B [90] photomultiplier tube.

The different elements in LITRANI (crystal, photodetector, wrapping, etc.) are three dimensional objects that are provided by the ROOT geometry package [86]. The ROOT geometry package was designed as a tool for building detector geometries in general (Other Monte Carlo engines are based on the same geometry package like GEANT3, GEANT4 and FLUKA). In Figure 4.1 a schematic drawing of the different main parts of a light yield measurement setup can be seen. The photons in the scintillating crystal can be produced in various ways. While the photon emission point can be random or fixed, the emission direction can be isotropic or directed. In addition a gamma source can be added to the setup. In our setup and in all simulations in this thesis, a Cs137 gamma source has been used which was placed $10mm$ away on the lateral sides of the crystal (like in the real world setup). Other parameters necessary for the photon generation by gamma excitation like the photo-electric cross section, the gamma-absorption length, and the emission spectrum were taken from the thesis of [37] for LYSO crystals.

a   b   c
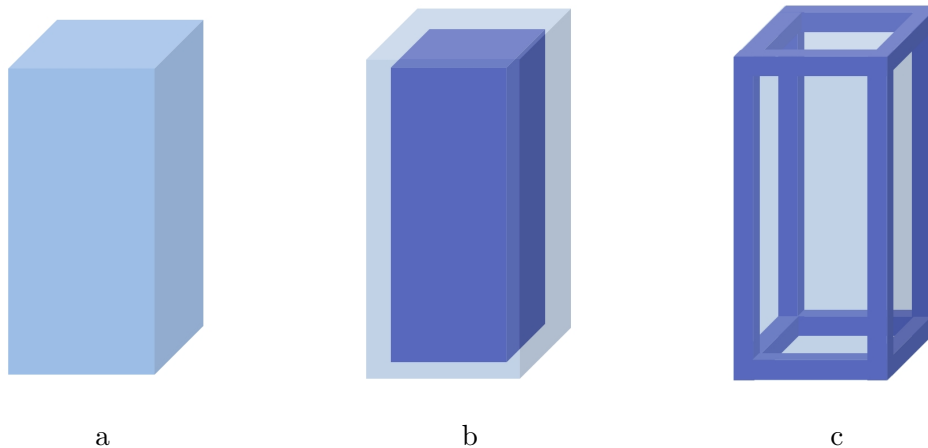
Figure 4.2: The different simulation models used for the parameter optimization procedure. To the left a homogeneous crystal is shown (a). The model shown in the middle (b) consists of two different materials, a core material and a shell material which models a different diffusion of the surface due to scratches and a certain roughness. The right model (c) consists of a different material at the edges to model imperfections coming from edge damages. In addition, the surface and edge model was combined into a fourth model consisting of three different materials with different diffusion parameters.

4.3.2   The LITRANI Crystal Model

This work was strongly focused on improving the crystal simulation parameters. Therefore, the configuration for the photomultiplier, the wrapping or the gamma emitting source has

not been changed from previous simulation setups and are adapted from the work of [2] and [37]. While the model matching technique of [2] was mainly based on the absorption and diffusion length of a $2 \times 2 \times 10 mm^3$ scintillator and different wrapping parameters, our model is based on a crystal type of half the volume (LYSO, $1.2 \times 2.6 \times 7 mm^3$) and on measurements without wrapping but with different contact agents (air, water, optical glue). Due to the small size of our crystal, wrapping which has to be applied manually is harder to manufacture in a constant fashion. Another reason for the change of the method was that on a small crystal, the light is much more often bouncing between the sidewalls before it gets absorbed, therefore, the optical properties of the surface is becoming much more important when the crystal size shrinks. For the model-fitting technique, four different crystal models has been studied (see Figure 4.2).

The light absorption of scintillator materials is an important parameter. In the work of [37] the technique of measuring the difference of the light transmission of the longer and shorter axis of the same crystal was used to determine the attenuation length of a $2 \times 2 \times 8 mm^3$ LYSO scintillator together with the index of refraction. In the case of a smaller aspect ratio of the crystal ($1.2 \times 2.6 \times 7 mm^3$) like in our case, the light diffusion and absorption inside a scintillating crystal could not be measured directly. The reason for that was the size of the beam diameter of the transmission bench which is slightly bigger than the crystal we were using.

4.3.3 Rough Surface Modelling

The optical parameters of the surface of a scintillator are an important characteristic, especially if the size of the scintillator is a fraction of the scintillators absorption length. Depending on the wrapping and out coupling medium, light can be reflected up to 50 times in the worst case before it gets absorbed or extracted. Small changes in the surface properties, like the polishing grade, crystal defects, or scratches can therefore have a large impact on the path the photon takes finally. Standard Monte Carlo light ray tracing programs like LITRANI can model an arbitrary combination of specular and diffuse reflection at the interface of two different materials. This is only accurate until a certain point, since the not perfectly flat surfaces of a scintillator (mean value of roughness, with reference??) is also showing some diffraction effect resulting from random phase variations induced by reflections from micro-topographic surface features. This effect has been published the first time by [87] and has been used in several different approaches to model rough surfaces in general [88] [89], but also especially for scintillator applications [91] [92]. In another

approach [93], the optical behaviour of different surface states of a BGO crystal has been measured using special crystal geometry, a laser light source and a photodetector array. The measured values were then implemented as a look-up table into the simulation code.

4.3.4   The Optimization Procedure

The basic idea was to make a computer model adapted to a small ($< 50mm^3$) scintillating crystal in LITRANI. Previous models could not reproduce simple measurement results like the ratio between the light yield of two different sized surfaces of one crystal without wrapping and contact agent. E.g. the ratio of the B and S side of the unwrapped crystal with air contact was measured as 1.42 (see Table 4.2) which was much lower in all previous models we had. The reason for that was expected to be the rough surface and edges which have a stronger effect on the overall result when the crystal is small. To know the optical properties of the surface of a scintillator is especially important if one wants to understand and design a photonic crystal, since there, the angle and amount of photons hitting the extraction surface is varying at a wide range when changing these parameters. For the optimization procedure we compared the light yield measurements of a LYSO crystal with the physical dimensions of $1.2 \times 2.6 \times 7mm^3$ to the simulation results of our Monte Carlo model. For that we used the measurements of the three different sized sides with three different contact agents (air, water, optical grease characterized by their index of refraction which was 1.0, 1.33 and 1.42 respectively) which results in nine different measurements. In addition, these 9 different measurements were taken from three different crystals of the same physical dimensions ($1.2 \times 2.6 \times 7mm^3$) manufactured by the same company. Three non-consecutive measurements were taken from each configuration and each crystal and the average was computed out of these nine measurements. The values can be seen in Table 4.2.

Table 4.1: The three different sides of the LYSO crystal and their abbreviation which is used in the chapters and tables later on. B=big, L=long and S=small.

Crystal Dimensions:	B	$6.97 \times 2.73mm^3$
	L	$6.97 \times 1.28mm^3$
	S	$1.28 \times 2.73mm^3$

Table 4.2: The light yield [$photons/MeV$] of the three different sides of a $1.2 \times 2.6 \times 7mm^3$ sized LYSO crystal (abbreviation according to Table 4.1) measured with three different contact agents. Each configuration was measured three times to give a total number of nine measurements for each configuration and where the mean was taken from.

Orientation	Water		Grease		Air	
	STDV	MEAN	STDV	MEAN	STDV	MEAN
B	649.5	10456.2	948.8	11912.6	303.7	4791.3
L	296.7	10081.6	734.2	11334.8	168.2	4318.1
S	500.0	7474.5	118.9	8339.9	186.4	3371.7

The Crystal Parameters

As shown in Figure 4.2, the crystal itself was subdivided into three different parts (bulk, surface and edges) which are all having different diffusion coefficients but were identical in all other crystal properties. The parameters used to model the LYSO crystal with our standard dimensions of $1.2 \times 2.6 \times 7mm^3$ can be seen in Table 4.3. For the additional light extraction caused by the surface roughness, two additional parameters were introduced which are different for the edges and the rest of the surface. When observed with an optical microscope, surface and edge damages in the range of $1\mu m$ for the surface and $50\mu m$ for the edges were visible and therefore underlining this approach. In our approach, the value of additional diffusion is describing the probability in % that a photon is randomly scattered when it hits the edge or surface. The extraction factor describes the probability that a photon is getting extracted at the surface due to surface roughness. This additional surface effects can be explained by Beckmann's and Kirchhof's theory of light scattering on rough surfaces [87] [88] and is usually a positive factor if light is traveling from a medium of high index of refraction (IR) towards a medium of a low IR.

4.3.5   Parameter Restrictions

To reduce the number of variables in the fit, the absorption (attenuation) coefficient was assumed to be fixed within a certain range for the whole crystal. This could be justified by transmission measurements performed by [37] where the light transmission for the long side of a LYSO crystal is compared to the transmission of the short distance of a $2mm \times 2mm \times 8mm$ LYSO crystal. The attenuation in this case is caused by the absorption of the bulk material, the diffusion of the bulk material and the additional diffusion by the surface roughness. In Formula 4.1 the three different components causing the attenuation in an transmission measurement are shown. By measuring the transmission of the short and

Table 4.3: LYSO model parameters used in the LITRANI simulations. The diffusion and absorption length of the base material are the most important parameters and has been modelled also in previous simulations [2] [37]. A different parameter for surface diffusion and the edge diffusion was introduced. This approach was driven by visible surface and edge damages in the range of $1\mu m$ for the surface and $50\mu m$ for the edges could be observed with an optical microscope. The value of additional diffusion is describing the probability in % that a photon is randomly scattered when it hits the edge or surface. The extraction factor describes the probability that a photon is getting extracted at the surface due to surface roughness. This additional surface effects can be explained by Beckmann's and Kirchhof's theory of light scattering on rough surfaces [87] [88] and is usually a positive factor if light is traveling from a medium of high index of refraction (IR) towards a medium of a low IR. The calculated values for our model are given in Table 4.5.

Parameter	Unit
Substrate Diffusion Length	$[cm]$
Substrate Absorption Length	$[cm]$
Additional Edge Diffusion	$[\%]$
Additional Surface Diffusion	$[\%]$
Additional Edge Extraction Factor	$[\%]$
Additional Surface Extraction Factor	$[\%]$

long distance of our crystal ($1.2mm \times 2.6mm \times 7mm$) one could theoretically also separate the diffusion from the surface by the diffusion and absorption from the bulk material. But due to the small size of that crystal the measurements could not be performed in the necessary precision to make this calculation. For the limits of the attenuation length we were therefore referring to actual literature. The work of [94] and [37] found the absorption length for LYSO between $30 - 40$ by different approaches. Since the crystals we were using were different than the crystals which have been used in these two publications, we extended the limits for the attenuation length to $\lambda_{att} = 25...45cm$ which could be restricted by transmission measurements.

$$\lambda_{att} = \left(1 - e^{\frac{l_c}{\lambda_{abs}}}\right) + \left(1 - e^{\frac{l_c}{\lambda_{diff}}}\right) + D_{surf} \tag{4.1}$$

- λ_{att} ... attenuation coefficient $[cm]$

- λ_{abs} ... bulk absorption length $[cm]$

- λ_{diff} .. bulk diffusion length $[cm]$

- D_{surf} ... additional diffusion by the surface$[\%]$

Having the attenuation length fixed within a certain range leaves us still three parameters to optimize: The additional diffusion coefficient of the surface, the additional extraction coefficient of the surface and the additional diffusion coefficient of the edges. This leaves a three dimensional parameter room. In the optimization procedure the measured light yield of the nine different configurations (three different sides with three different contact agents) were compared to the according simulation results while scanning over a given range of the three parameters. The deviation of the simulated and measured light yield was added together for all nine configurations and was then used as a measure of the quality of the fit. The best fit was searched by scanning over a meaningful range of these three parameters which was computational very expansive. If each parameter was split up into twenty different values this would have left 8000 simulations for each of the nine configurations, where one simulation had to be of 200000 photons to give statistically correct results. The simulation of 200000 photons in our LITRANI model takes about five minutes on a 3GHz processor which would mean that the whole optimization would take at least $8000 * 9 * 5min = 250$ days. For that reason, the simulations were performed on the CERN batch computing service in a highly parallel manner. When the minimum in the $20 \times 20 \times 20$ parameters space was found, it was refined by searching in an even smaller grid and also the parameters which were assumed to be fixed first were varied within a small range to get an even better fit.

4.3.6   Simulation Results

In our simulations, the three unknown main parameters (additional surface diffusion - S_{diff}, additional surface extraction - S_{extr}, additional edge diffusion - E_{diff}) where varied between a given range. For each parameter set, the cumulated error of the nine different crystal configurations (three sides of different sizes with three different contact agents) was calculated as a quality measurement for the fit. The cumulated error consists of the sum of errors for each configuration. As an example in Figure 4.3 the ratio between the light yield of the grease- and air coupled small side of the crystal is plotted. The measurement for this configuration results in a ratio of 2.45 which restricts the additional surface diffusion factor to a value of about 80 but it does not restrict the additional surface extraction factor in any way (all the values along the black dashed line in Figure 4.3 are possible). Therefore several different configurations have to be taken into account to further restrict these parameters. As an example, the minimum in the fit of the LY ratio of the big (B) side and the small (S) side of the crystal is different (see dashed line in Figure 4.4) and

together with the simulations from Figure 4.3 a smaller parameter range can be found. The range of possible parameters gets smaller with every additional crystal setup which is taken into account, e.g. when overlying the plots of 4.3 and 4.4, S_{diff} and S_{extr} are already confined to a small area. When adding all errors of the nine configurations while scanning through the S_{diff} and S_{extr} parameter range one gets a plot like shown in Figure 4.5. The minimum in the cumulated error is found at a surface diffusion factor of 80 which means that the surface area (modeled as $50\mu m$ thick) has 80 times more diffusion as the base material which leads to a diffusion probability of 0.57%. The additional surface extraction factor (S_{extr}) has been found at 2.7 %. The black dashed ellipse around this point indicates the region of the error which is the accuracy of the light yield measurements and can be restricted to $\pm 5\%$. When looking to the corresponding absolute light yield which was simulated for that parameter region (see Figure 4.6), we get an value between 33000-37000 $[pht/MeV]$ which is in good agreement with values of actual literature [2][35]. For clarity in these plots only two parameters are shown. The third parameter (E_{diff}), which is not shown in these plots was also varied between zero and complete diffusion and was found to fit best when having about five times the diffusion probability of the surface.
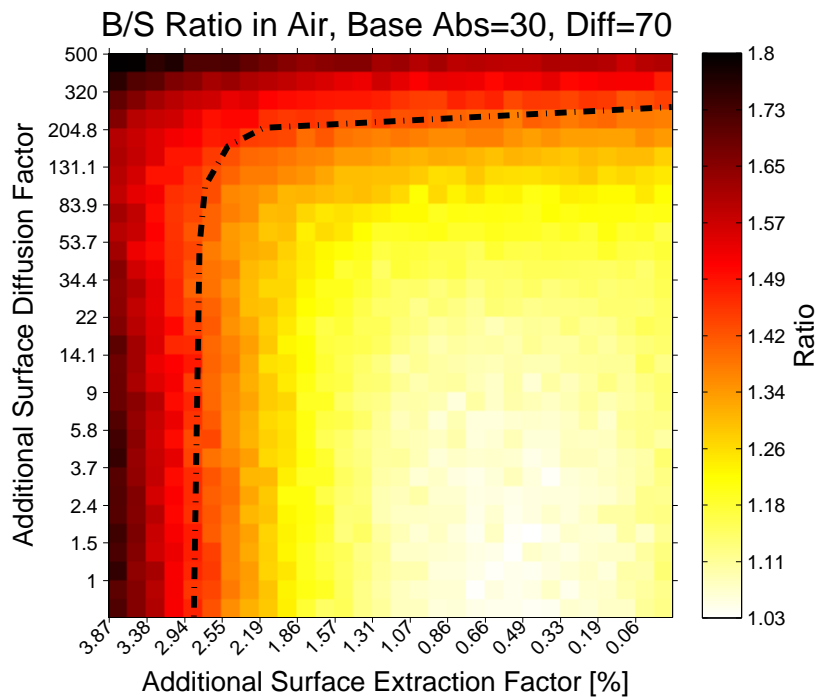
Figure 4.3: Ratio of the simulated light yield between the big (B) and the small (S) size of the crystal when having air as a coupling medium. The measured ratio of the light yield between the S and B side is 1.41 which is shown as the parameter range along the black dashed line. It is obvious, that with only this configuration, a clear minimum in the parameter space cannot be found since the model fits with the same minimum in deviation all along the black line. As a consequence, the simulation of different configurations has to be taken into account when using this model fitting technique.
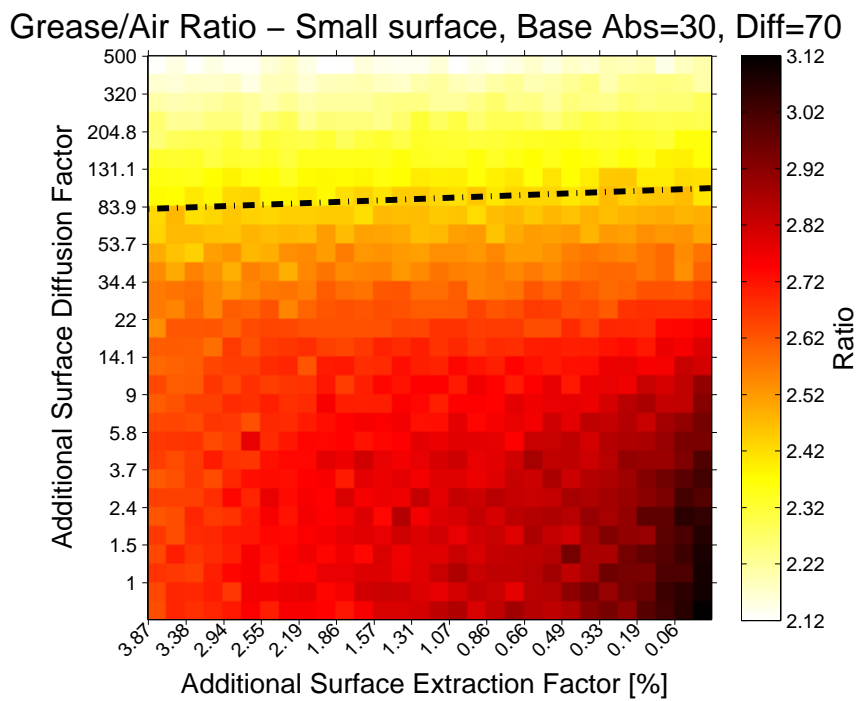
Figure 4.4: Ratio of the simulated light yield between grease- and air coupled crystals when using the small (S) side towards the PMT. The measured value of this ratio is 2.45 which correspond to the parameters along the black dashed line. Again, we can see that with only this measurement, one cannot find a clear minimum, since the model matches the measurements with the same error all along the line.
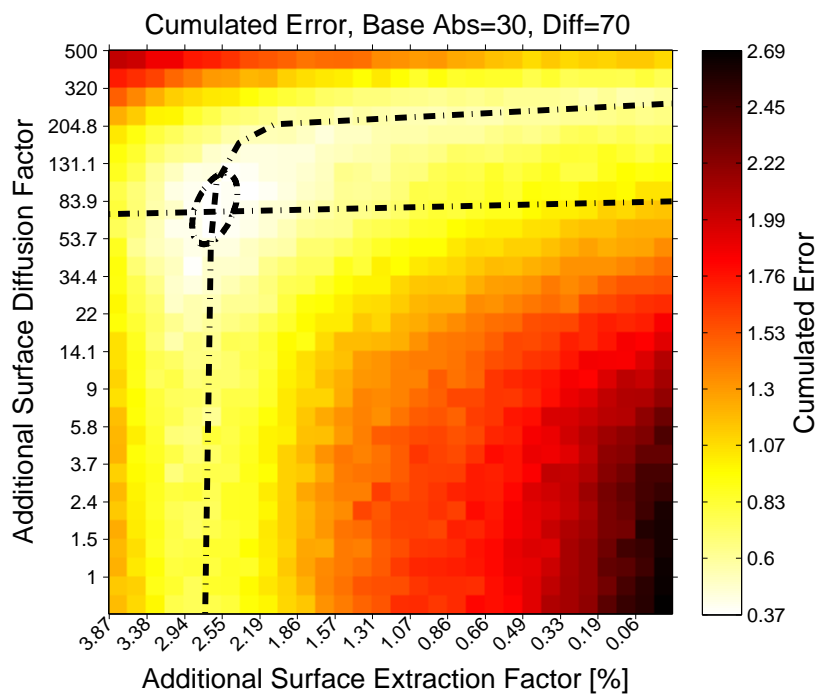
Figure 4.5: Combined error of the nine different configurations as a function of the surface diffusion (SD, y-axis) and the additional extraction Factor (AEF, x-axis). A clear minimum (black dashed circle) can be seen in the area around SD=80× and AEF=2.7%.
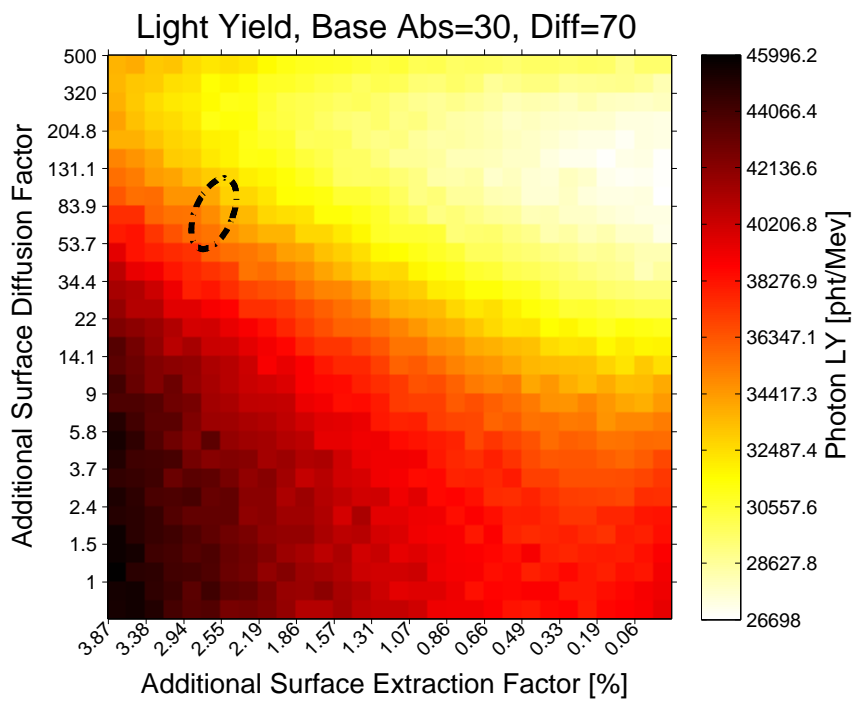
Figure 4.6: Simulated absolute light yield as a function of the surface diffusion (y-axis) and the additional extraction Factor (x-axis). The area of the best fit (black dashed circle) which was established in Figure 4.5 covers an absolute light yield of 33000-37000 photons/MeV.

When looking to the simulation results of this model after the fitting process, we can see that the values are showing a good agreement to the measurements (see Table 4.4). The LYSO model parameters which were resulting in the best fit (Figure 4.5) can be seen in Table 4.5. A comparative bar plot of the measured light output and the simulated light yield can be seen in Figure 4.7.

Table 4.4: The simulated light yield data from the LITRANI model compared to the measurements from Table 4.2. The simulated and measured light yield data show a maximum deviation of 8% and a mean deviation of $\pm 3.2\%$ for all orientations and contact agents. The contact agents were air, water and grease with a index of refraction of 1.0, 1.33 and 1.41 respectively.

O	Water			Grease			Air		
	Measure	Simulat.	Diff.	Measure	Simulat.	Diff.	Measured	Simulat.	Diff.
B	10456	10494	0.4	11913	11440	4.1	4791	4662	2.8
L	10082	9378	7.5	11335	10534	7.6	4318	4376	1.3
S	7475	7302	2.4	8340	8225	1.4	3372	3320	1.6

Table 4.5: Optimized LYSO model parameters of the LITRANI simulations. The diffusion and absorption length of the base material are in good agreement with other models of LYSO [2][37]. A different parameter for surface diffusion and the edge diffusion was introduced since obvious edge damages in the range of $50\mu m$ could be observed with an optical microscope. The value of additional diffusion is describing the probability in % that a photon is randomly scattered when it hits the edge or surface. The extraction factor describes the probability that a photon is getting extracted at the surface due to surface roughness. This effect can be explained by Beckmann's and Kirchhof's theory of light scattering on rough surfaces [87] [88] and is usually a positive factor if light is traveling from a medium of high index of refraction (IR) towards a medium of a low IR.

Parameter	Unit	Value
Substrate Diffusion Length	$[cm]$	70
Substrate Absorption Length	$[cm]$	30
Additional Edge Diffusion	$[\%]$	2.0
Additional Surface Diffusion	$[\%]$	0.56
Additional Edge Extraction Factor	$[\%]$	2.7
Additional Surface Extraction Factor	$[\%]$	2.7
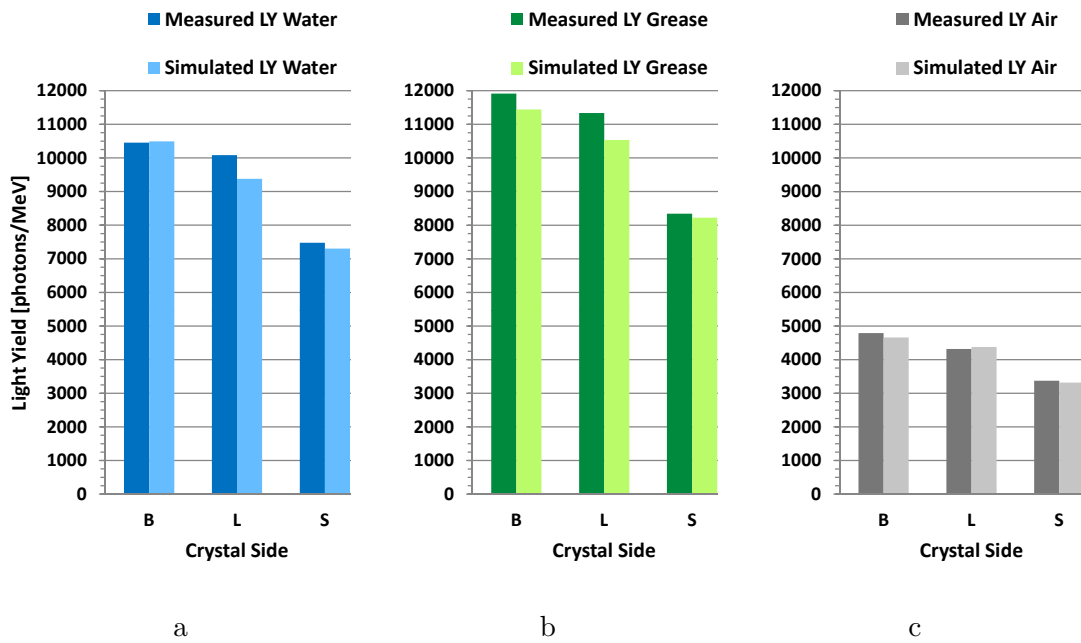
Figure 4.7: Comparison of the light output of the simulation with the light output of the measurements of the different crystal configurations (Bar plot of the values from Table 4.4).

4.4 The Angular Light Distribution Simulation

The determination of the angular distribution within a scintillator is an important task when one wants to design a PhC grating for the light extraction improvement. The modelling of the different diffusion and absorption parameters has a big influence on the performance of such a structure. The angular distribution can change dramatically with this parameters especially when the surface state of the crystal changes. In Figure 4.10 and Figure 4.11 an example is shown where a LYSO scintillator with perfect surface polishing is compared to a crystal with a rough surface finish. It can be seen, that the angular distribution within the scintillator is similar between the two configurations until the angle of total internal reflection (Θ_c). In the case of perfect surface conditions, the photons are much more populated after Θ_c since they travel in a total reflection mode and therefore are going to recur several times at the outcoupling surface. In the case of rough surfaces, the photons are changing slightly their angle every time they hit a surface and are therefore ending up with an angle which allows transition to the outside after several reflections already. The angle Θ in the plots are measured between the impinging or emitted photon and the normal to the surface (see Figure 4.8) which means that the photons with lager Θ are getting more populated (see Figure 7.12) and therefore one usually gets the characteristic shape of an angular distribution which is plotted in Figure 4.10 and Figure 4.11.
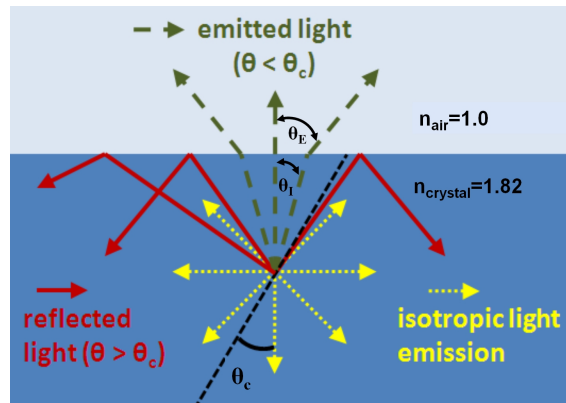
Figure 4.8: The definition of the angles at a scintillator-air interface. The impinging angle Θ_I and the resulting emission angle Θ_E is measured between the normal of the surface and the photon path. Photons impinging with an angle larger than the total reflection angle Θ_c cannot escape the crystal.

The angular distribution of light within an unstructured scintillator is mainly governed by the dimensions of the crystal, index of refraction, the surface polishing grade and the
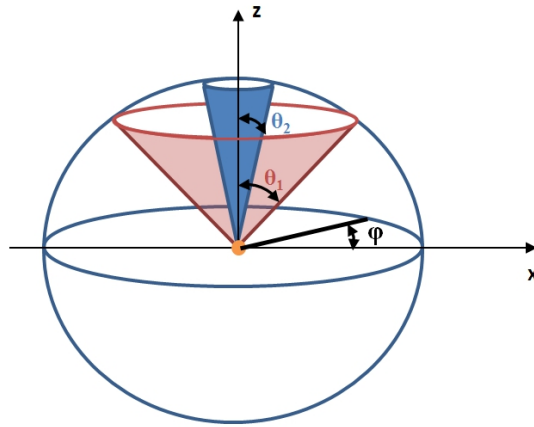
Figure 4.9: For an isotropic light emitter, photons with an larger angle Θ are more populated which can be seen when comparing the different sizes of the light cone from photons with the angle Θ_1 and Θ_2. The azimuth angle is usually denoted with the Greek letter ϕ.

type of wrapping for the lateral faces. In the presence of a PhC grating at the out-coupling side of the scintillator, the angular distribution can change as well (see Chapter 5). The reason for that is mainly that the light diffraction efficiency of a PhC is dependent on the light propagation angle, therefore certain angles will be diffracted stronger than others and this will change the outside angular distribution.

4.4.1   Internal Angular Light Distribution

In addition to the angular distribution of the emitted light, it is of great importance to have a good understanding of the light which propagating inside the crystal together with the parameters influencing it. For example, the PhC performance changes with the angular distribution of light inside the crystal due to an angular dependence of the light extraction efficiency. While the angular distribution outside of the crystal can be measured (see Sub-Chapter 7.3) the internal distribution of light which is impinging on the crystal air interface cannot be measured directly. By the means of Snell's law, the angular distribution from the outside can be of course mapped to the distribution in the inside (assuming a perfect crystal surface) of the crystal but just to the angle of total internal reflection, since all other light is not traceable from the outside. But for the simulation of the PhC interface, the angular distribution of the whole angular range inside the crystal is needed. Some of the parameters and properties of a wrapped LYSO crystal are well understood and has been optimized in the work of [2], [37] and [1]. But in the

case of a crystal without wrapping, like used in our setup, the surface state (depolishing grade) of the crystal has to be taken into account as well, since it mainly governs the path a photon takes within the crystal. In Figure 4.10 the internal light distribution is shown in the case of a uniform crystal and a crystal model using the additional surface diffusion and extraction parameters. It can be seen, that the result does not change until the angle of total internal reflection (TIR, $33 degrees$) but changes dramatically above this angle. This is the effect of TIR which leads to total reflection modes where photons are reflected between the sidewalls of the crystal until they get absorbed by the base material. In reality, the total reflection modes are not that strong, since the photon gets diffused with a certain probability every time it gets reflected by the surface, therefore the angular distribution changes as can be seen in Figure 4.10 (red dashed line). When looking now to the angular distribution of the emitted light of these two configurations (see Figure 4.11), it can be seen that this effect is not visible on the outside, since the majority of the extracted photons coming in both cases from the impinging angular range before the total reflection angle ($0 - 33 degrees$) and this distribution is almost the same in both cases.

4.5 Conclusion

The aim of the work in this chapter was to develop a LITRANI based scintillator model to simulate the light propagation of small (several tenths of cubic millimetres) heavy inorganic scintillators. The light distribution inside and outside a scintillating crystal is of great interest when it comes to optimizing the light collection in a detector system. This knowledge is especially important when it comes to photonic crystal gratings at the light out-coupling side of a scintillator, since the light extraction performance is dependent on the angle of the impinging photon and the recurrence of reflected photons. Based on the measurements of a $1.2 \times 2.6 \times 7 mm^3$ sized LYSO scintillator we have tested different simulation models to reproduce the measurement results of our $1.2 \times 2.6 \times 7 mm^3$ large LYSO sample. By measuring the light output of the three different shaped sidewalls of the crystal with three different light coupling agents respectively, we could obtain nine independent measurement configurations. To reproduce these results in our model, we saw that we had to move from the uniform crystal model towards a crystal model which has different light propagation properties for the surface and the edges. By introducing additional light diffusion for the surface and edges and an additional light extraction factor for all surfaces, the measured light yield of the different configurations could be reproduced by our simulations with an average deviation of $\pm 5\%$. The values of the different crystal
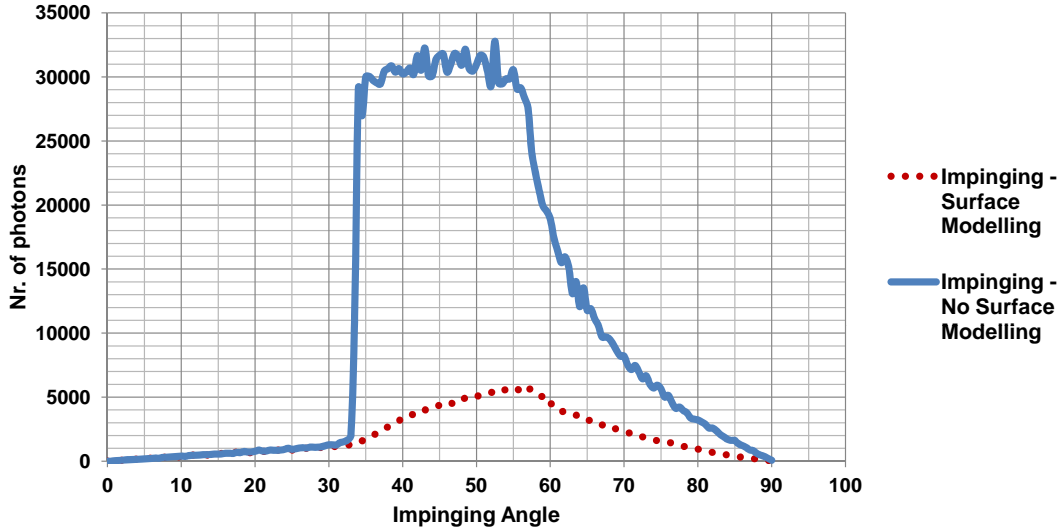
Figure 4.10: Comparison of the impinging photons at the extraction surface of a LSO scintillator. A LYSO scintillator of the dimension $1.2 \times 2.6 \times 7mm^3$ was used in that simulatiom. The solid blue line shows the distribution inside a scintillator with a theoretical perfect surface state. The red doted line shows the distribution of a crystal with approximated real surface parameters like modeled by our approach. One can see a big difference, the photons traveling in total reflection mode are much more populated in the ideal scintillator since there they are reflected between the sidewalls until they get absorbed by the crystal while in second case they are much more likely to leave the crystal since the surface roughness is changing the reflection angle every time the photons hit the surface. Apart from that, the two distributions are similar in the range of $0 - 33$ degrees which explains the almost matching angular distribution of extracted photons in the next plot.

parameters (see Figure 4.5) were calculated in an optimization routine where the values where scanned in a successive way to figure out the best fit between the measurement and the simulation (see comparison between measurements and simulations in Figure 4.7). To show the difference between a model without special surface treatment and our model including additional surface- and edge diffusion and additional surface light extraction, an angular distribution of both models was computed and is shown in Figure 4.10. The plot shows that for the impinging photon distribution inside the crystal there is a big difference for angles larger than the total reflection angle. The accurate simulation of this distribution is of great importance for the correctness of the following PhC simulations in this work since a photonic crystal grating has also an extraction effect on photons impinging in a
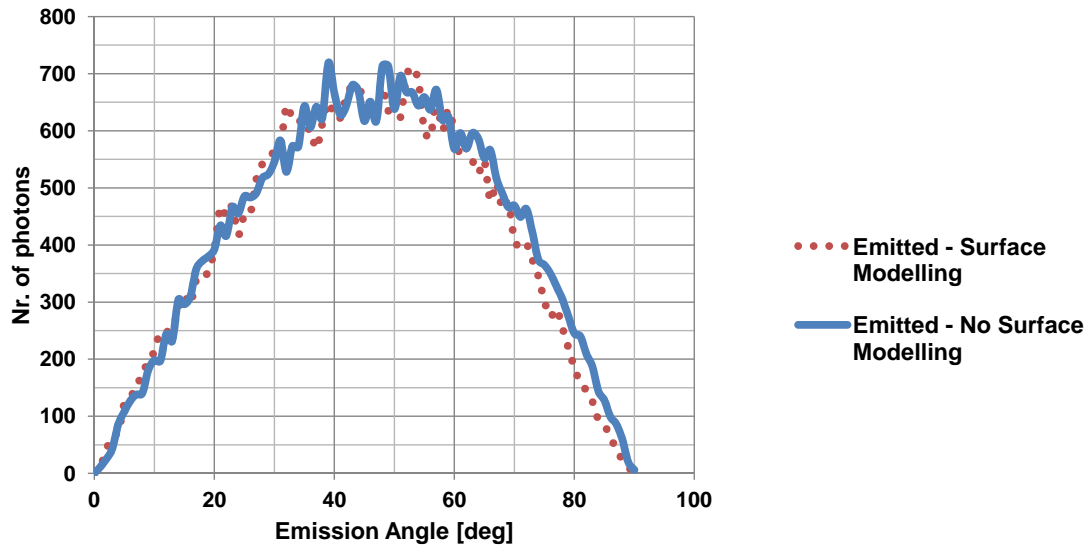
Figure 4.11: Comparison of emitted light between a un-wrapped LSO scintillator with and without special surface treatment (also compare the impinging photons in Figure 4.10 which are from the same simulation model). The curves are very alike since most of the photons are coming from the impinging angular range before the total internal reflection (33 degrees) which is similar for both cases.

larger angle than the total reflection angle. The current model parameters are fitted to the crystal type we have used for our experiments. Therefore these parameters cannot be used for a general crystal model, since the type of crystal and the exact state of the surface roughness will change from sample to sample. That means that for other types of crystals the measurements have to be repeated but the corresponding optimization routine can be reused of course.

Chapter 5

Photonic Crystal Simulation

Contents

The simulation of photonic crystal structures in one-, two-, or three dimensions is a complex and non-trivial problem. Numerous mathematical techniques were developed during the last decades. Many commercially and freely available software packages exist. They can be used to simulate photonic bands, scattering matrices, field patterns, light extraction efficiencies, reflection and transmission coefficients or resonant cavities of photonic crystals. Their applicability depends mainly on the exact application and every technique has its advantages and disadvantages. A good overview of the different computational methods and modelling tools can be seen in [95]. In our work only two different software packages were used to calculate the PhC properties of the extraction gratings. To calculate the photonic bands of a PhC slab in Chapter 3 the MIT MPB package has been used [75]. For the calculation of field patterns and extraction efficiencies the CMFR package has been used [96]. The principles of these two simulation tools are summarized in the following sections.

5.1   MPB - MIT Photonic Bands

The freely available MIT Photonic-Bands (MPB) tool which is a software package released under the GPL (GNU General Public) license. MPB uses a fully-vectorial, three-dimensional algorithm to compute the definite-frequency Eigen states of Maxwell's equations in arbitrary periodic dielectric structures. The number of Eigen states and band numbers can be chosen by the user. The algorithm applies a Fourier transform over an infinite repetition of the unit-cell (smallest entity of the PhC pattern) in all three dimensions. The disadvantage of that method is, that for three dimensional problems like the PhC slab we are using, this can introduce some problems since the unit-cell is not repeated in the z-direction. For PhC slabs, MPB can therefore only calculate the guided modes (below the light line) with high accuracy. As a solution, the unit cell size is extended into the z direction by several lattice constants $(3 - 8a)$ which reduces the influence of the z-periodicity on the leaky modes to a negligible amount [79].

5.2   CAMFR - CAvity Modelling FRamework

For the simulation of the PhC structures a Rigorous Coupled Wave Analysis (RCWA) algorithm implemented in the CAMFR [96] software package was used. CAMFR is a common tool for the electromagnetic study of nano scaled gratings in multilayer structures. The software is based on an Eigen mode expansion algorithm and works for one- or two dimensional PhC gratings. The RCWA algorithm uses a unit-cell which can have any arbitrary geometry. An example of an unit-cell can be seen in Figure 5.1. In the RCWA method, special boundary conditions have to be applied in directions where the unit cell is not repeated periodically. For that reason, usually the perfect matching layer (PML) approach is used. A PML represents a non-physical material that absorbs waves without any reflection, at all frequencies and angles of incidence [97]. The sides of the of the computation unit-cell where no PML is applied are assumed to be periodically repeated in the according directions. The PhC layer in the RWCA method is implemented as a Fourier expansion of slices of the index of different index of refractions in the xy-plane (see Figure b in 5.1). The accuracy of the method increases with the number of slices. As a disadvantage, the computational effort increases as well and therefore it is recommended to keep the number of slices to a reasonable amount. The input and output fields of the whole structure is computed by matching the boundary conditions and are then computed by the scattering matrix technique [98].

a   b
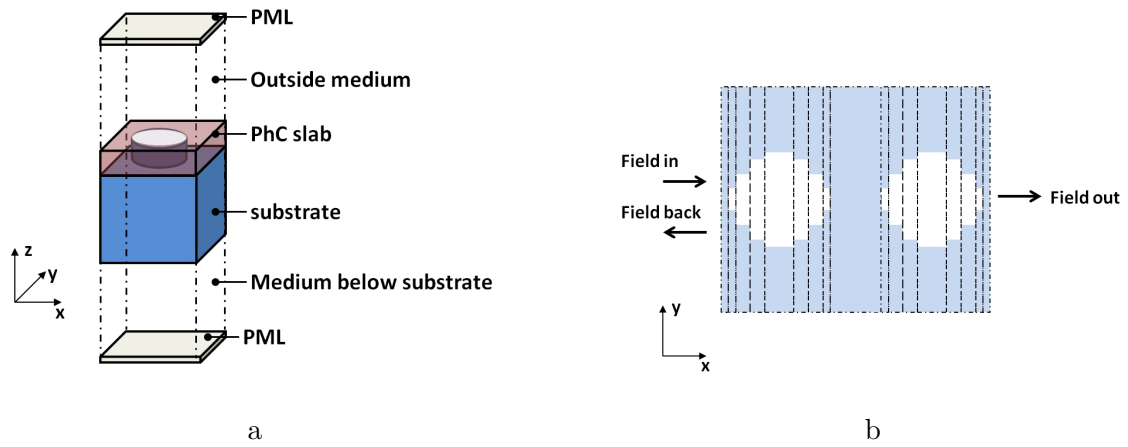
Figure 5.1: (a) Computational unit-cell enclosed by perfectly matched layers in z direction and infinitely periodically repeated in the x- and y-directions. (b) Fourier expansion of the PhC structure in the xy-plane.

In CAMFR, a unit-cell is divided into slices perpendicular to the direction of propagation. In each slice, the refractive index is constant in the propagation direction. The different sections are then joined with the scattering matrix technique [98] to model non uniformity in propagation direction.

5.3 CAMFR Simulations

5.3.1 Photonic Crystals in Combination with Scintillators

At the present we do not know any light ray tracing software which can simulate photonic crystals. Therefore these two parts has been separated. The PhC slab has been simulated with a photonic crystal simulation toolkit named CAMFR. The optical transition and reflection properties were calculated using this software and then integrated as a lookup table into the source of the Monte Carlo program LITRANI [85]. LITRANI was used to study the light propagation within a heavy inorganic scintillator setup. It traces photons throughout any combination of three dimensional shapes with different optical properties. The photons can be generated by different types of sources and will be tracked from the birth until absorption or detection. In our case, the emission light was produced using 662keV photons from a point source (Caesium-137) in a distance of 1cm. The photo absorption coefficients were taken from the NIST database [99], the index of refraction, attenuation and diffusion coefficients of the crystal were taken from laboratory measure-

ments. The photonic crystal diffraction effect depends on the angle of the photon which is impinging on the PhC and the number of times they reappear when they get reflected. In particular the reflection property of a PhC slab varies with the inclination angle Θ (angle between the photon direction and the normal of the interface at the impinging point), the azimuth angle ϕ and polarization (transversal electric TE, or transversal magnetic TM) of the photon. Our simulation has shown the strongest dependency on the inclination angle Θ, therefore we have been averaging the photons over all polarizations and azimuth angles to give us a simplified model where the distribution as well as the reflectance is only a function of Θ. An example of an angular distribution plot can be seen in Figure 5.2.

5.3.2 The Optimization Procedure

The photonic crystal structure was optimized for a maximum in light extraction efficiency when applied to a LYSO crystal with the dimensions of $1.2 \times 2.6 \times 5 mm^3$. The simulated angular distribution of the impinging photons inside the scintillator at the extraction surface can be seen in Figure 5.2.
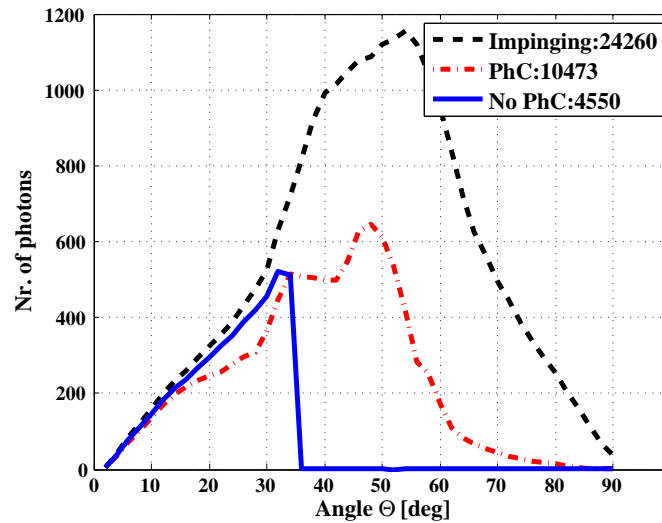
Figure 5.2: The angular distribution of impinging photons at the crystal air interface and the different distributions of photons which get extracted in the presence of a PhC grating or no grating. The overall number of impinging photons is shown as the black dashed line. The number of extracted photons for the PhC sample is shown as the red dot-dashed line. The solid blue line is from the unstructured reference crystal.

The plot shows the distribution of photons in relation to the incident angle Θ (angle

between the incident photon and the normal to the surface). One can see that a majority of impinging photons (black dashed line) reach the surface with an angle of 30 to 70 degrees, which is characteristic for LSO crystals in air since the total internal reflection angle is 33 degrees and most photons are traveling above that angle. At 67 degrees, the photon density decreases again, since above that angle they can be extracted again after a second reflection (assuming orthogonal surfaces of the crystal). The CAMFR simulation tool calculates the power transmission coefficients of the PhC slab with respect to the incident angle. A plot of this transmission coefficients of a plain crystal air structure and a PhC structure can be seen in Figure 5.8. The different polarizations and azimuth angles are averaged in this plot. The number of extracted photons is then calculated by multiplying the number of photons impinging on a unstructured surface with the corresponding transmission coefficient of a PhC structure (see red dashed line in Figure 5.2). We have designed and optimized three different PhC structures, two consisting of triangular placed holes (see Fig. 5.3) and one consisting of squared shaped pillars(see Fig. 5.4). For each PhC design, the light diffraction properties at a fixed wavelength are governed by the following parameters:

- Index of refraction of the bulk material

- Index of refraction of the filling material

- Lattice constant a

- Filling factor f
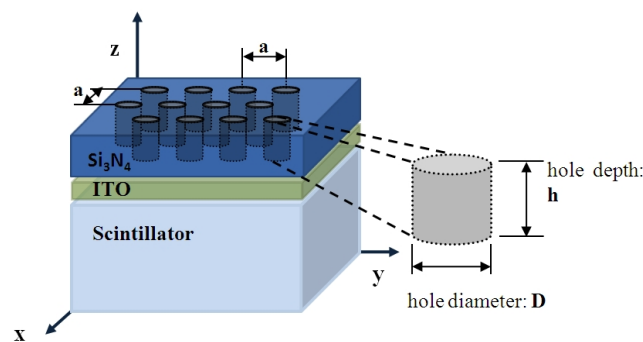
Figure 5.3: Design of the PhC structure of triangular placed air holes in a slab of silicon nitride.

The filling factor is the ratio between the area of the bulk material and the outside medium. The index of refraction of the bulk and outside material is fixed since we have
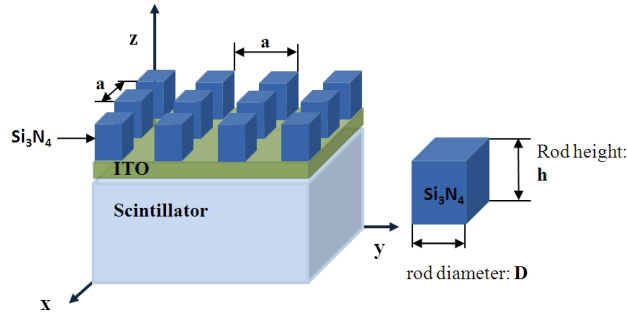
Figure 5.4: Design of the PhC structure square pillars of silicon nitride surrounded by air.

silicon nitride (Si_3N_4, refractive index at 420nm=1.85) deposited as the pattern transfer material and we have air on the outside. Therefore there are three parameters left to optimize: the lattice constant, the filling factor and the pattern thickness. In a 3-D scan of the parameter space the light output was optimized. A certain dimensional tolerance in the PhC construction was also taken into account in the parameter search since we had 10-15% deviation of the filling factor in the previous PhC samples produced with the e-beam lithography approach. The dependency of the extraction efficiency on the lattice constant a and the hole diameter d can be seen in Figure 5.5. It was found that the best thickness for the triangular pattern was 450nm. Since the other PhC patterns were etched on the same scintillator, this thickness was fixed at 450nm for the squared pillar samples as well. The results of the optimized parameters can be seen in table 5.1. All parameters have been designed for a wavelength of $\lambda = 420nm$ which is the peak emission wavelength of a LSO/LYSO crystals.

5.3.3   Reflection and Radiation Patterns

The reflection properties of a photonic crystal have been calculated for all possible angles resulting in a 2D plot of intensities, where the reflection is a function of the k-vectors Kx and Ky of the impinging light. In addition a 2D map is calculated which shows the radiation pattern of transmitted light in the ambient air (see Figure 5.10). For the better understanding of the Kx/Ky plots of the following 2D radiation and reflection patterns, the polar coordinate definition is plotted in Figure 5.7.
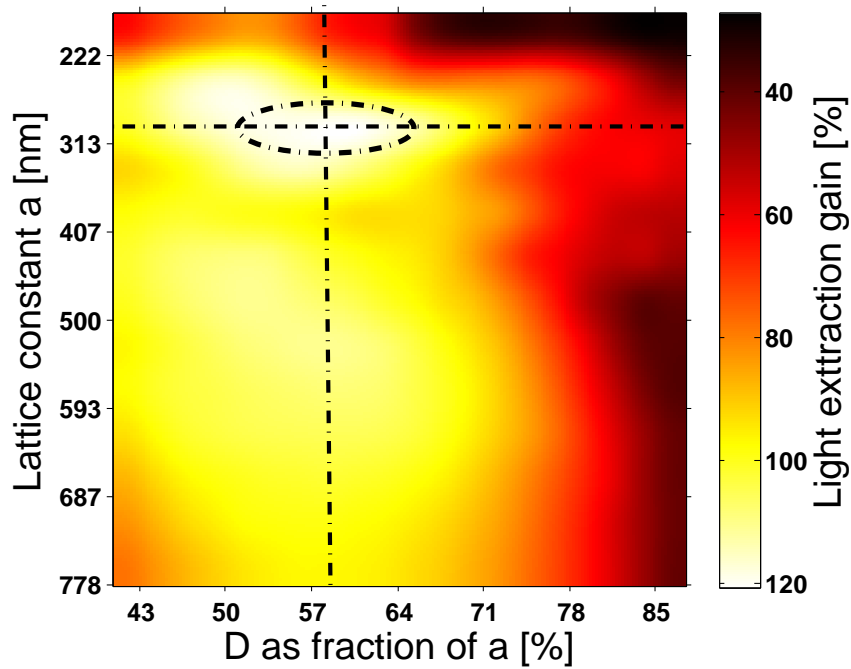
Figure 5.5: Light extraction gain of a triangular PhC structure as a function of the lattice constant a and the hole diameter D at a slab thickness of 450nm (Interpolated from a 30 × 30 grid). The gain is with respect to the amount of light which is extracted from an unstructured reference LSO crystal in air surrounding. The maximal extraction efficiency is found at a Lattice constant of 300nm and a hole diameter of 180nm. This optimization procedure was performed for different thicknesses in a grid of 30nm within a range of 100-750nm. The best results were obtained at a PhC slab thickness of 450nm.
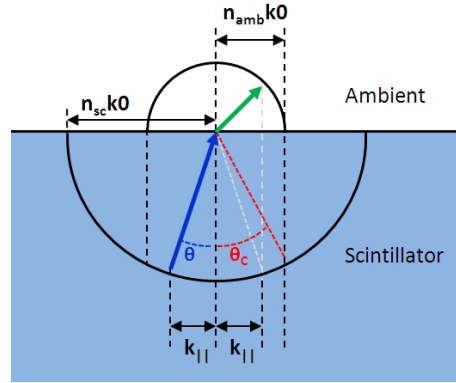
Figure 5.6: K-vector diagram of a scintillator/ambient interface. Due to Snell's law, light can only escape the crystal when the angle is smaller than the critical angle $\Theta < \Theta_c$. This relation, which is also known as Snell's law, can also be derived from the conservation of the in-plane vector $k_{/parallel}$ which is the k-vector component parallel to the interface. The vacuum vector length is $K_0 = 2\pi/\lambda_0$ which does not change in the case of air. In the diagram we can see that for light in the ambient medium $k_{/parallel}$ cannot get bigger than $n_{amb}k_0$ and therefore light having a bigger angle than Θ_c will be internally reflected.
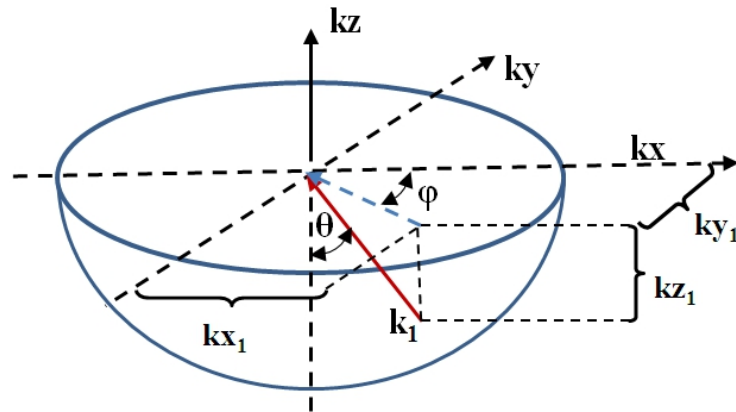
Figure 5.7: Definition of the polar coordinate system used in the calculations. A photon with the k-vector k_1 impinges at the interface. It has the inclination angle Θ and an azimuth angle φ and can also be defined by its in-plane components k_x and k_y.
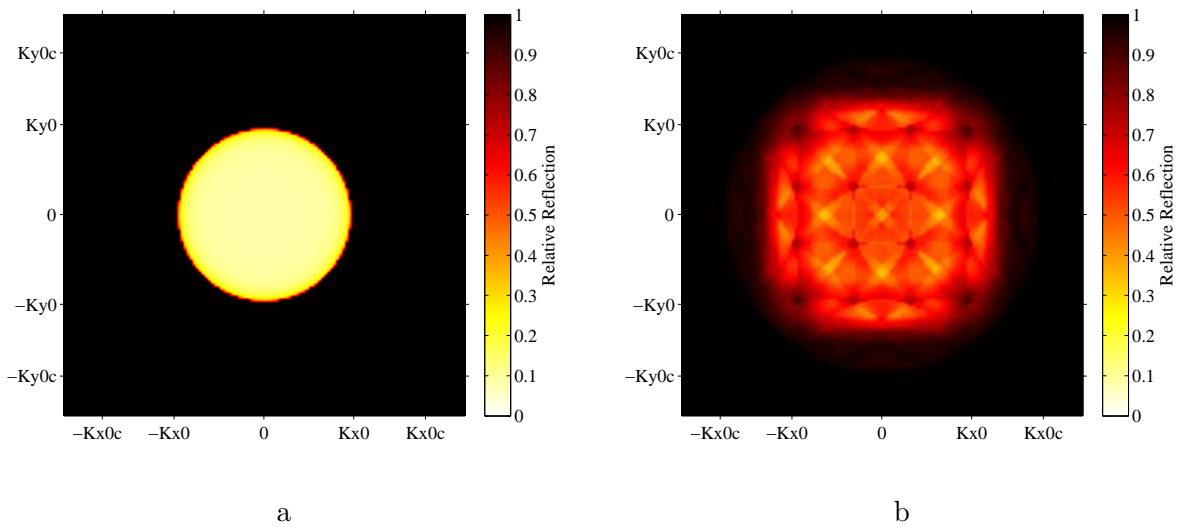
Figure 5.8: **Left:** 2D - Reflection map (unpolarized $= (TM + TE)/2$) plotted over photons impinging on a classical LYSO/air interface. For k-vectors $> kx0$ there is no transmission to the outside due to total internal reflection. **Right:** The photonic crystal is designed for transmission also outside the air cone ($|k| > k0$). As a drawback one can see that the reflections within the air cone are bigger than for the unpatterned structure. Kx0 is the k-vector size in air and Kx0c is the k-vector size in the crystal (compare Figure 5.6).
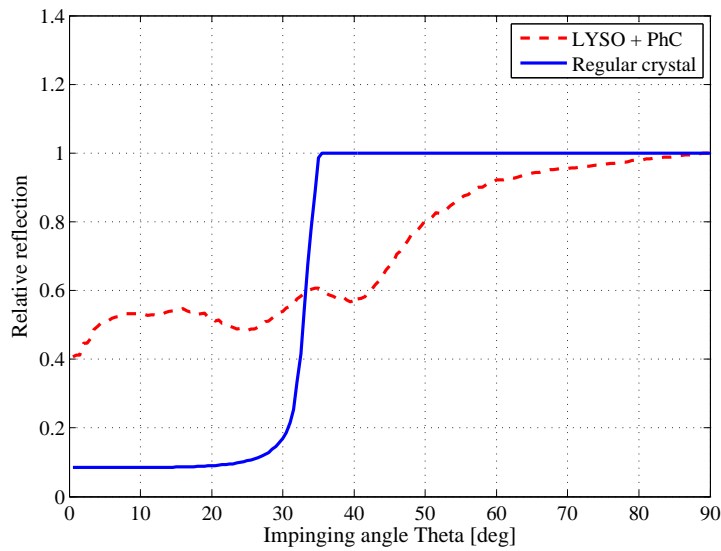
Figure 5.9: Reflection for unpolarized light as a function of the inclination angle Θ averaged over all azimuth angles φ (compare Figure 5.8). Apart from the enhanced transmission for light with $\Theta > 33$ degrees it also shows that the PhC structure reflects a significant amount of light within the range of 0-33 degrees compared to the unstructured sample. But due to the nature of the angular distribution of light impinging on a crystal surface (light wit $\Theta > 33°$ are much more prevalent), the PhC structure still shows a gain over the regular structure.

Radiation Pattern

The simulation results plotted in Figure 5.10 and Figure 5.11 show the extraction performance of a PhC sample compared to an unstructured sample as an angular distribution plot. In this configuration, which was a square pattern of silicon nitride pillars, the PhC showed a gain of about 6-7% over the whole Θ range for an isotropic emitter. The extraction performance of an actual scintillator with this extraction surface treatment would be different since we do not have isotropic emission from inside the crystal. Instead we have a lot of photons traveling in a total reflection mode and impinging on the surface several times. These photons can be extracted by the PhC but not by the conventional crystal. Therefore the performance of such a PhC structure is mostly dependent on the angular distribution inside a scintillating crystal. And this distribution is also dependent on the shape of the crystal and the type of wrapping. The choice of which pattern we were using in the final sample was made based only on the expected over all light yield gain and was not dependent on the angular distribution. Basically the plot in Figure 5.5 which shows the light extraction gain in dependence of the PhC parameters was giving us the restrictions for the design. The radiation pattern was not taken into account since the first step of our approach was just to show the PhC effect on the light yield perforamnce which was easier to fabricate and to show. Once this step is accomplished, the next step would be the design of an optimized angular distribution of the extracted photons, for example to optimally fit the angular response of a photodetector.

a
b
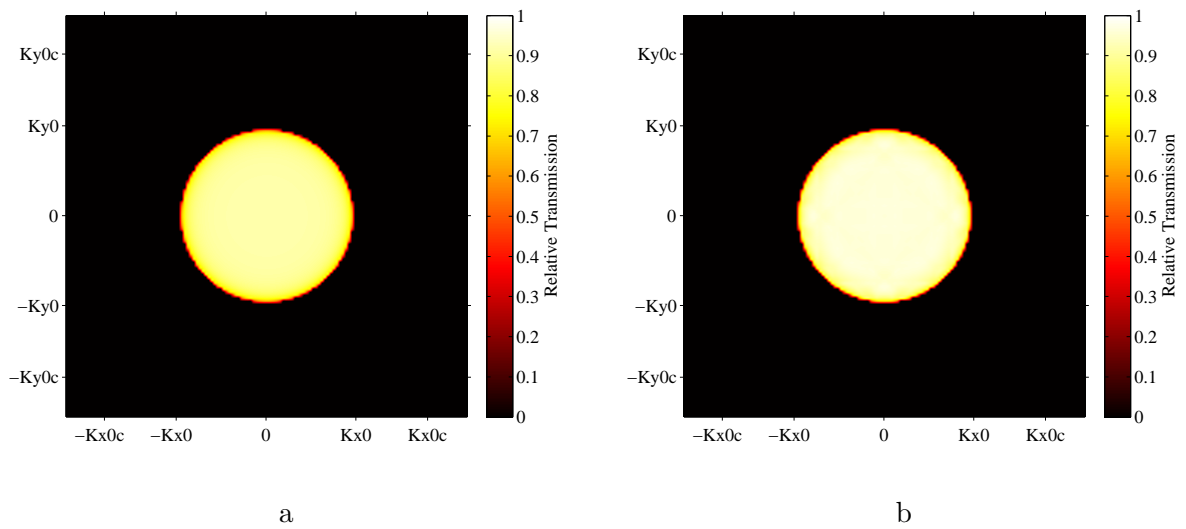
Figure 5.10: Left: Radiation pattern into air of a unpatterned LYSO/air interface. Right: Radiation pattern of the PhC enhanced interface. Both plots are calculated for an isotropic and un-polarized light emitter. Kx0 is the k-vector size in air and Kx0c is the k-vector size in the crystal (compare Figure 5.6).
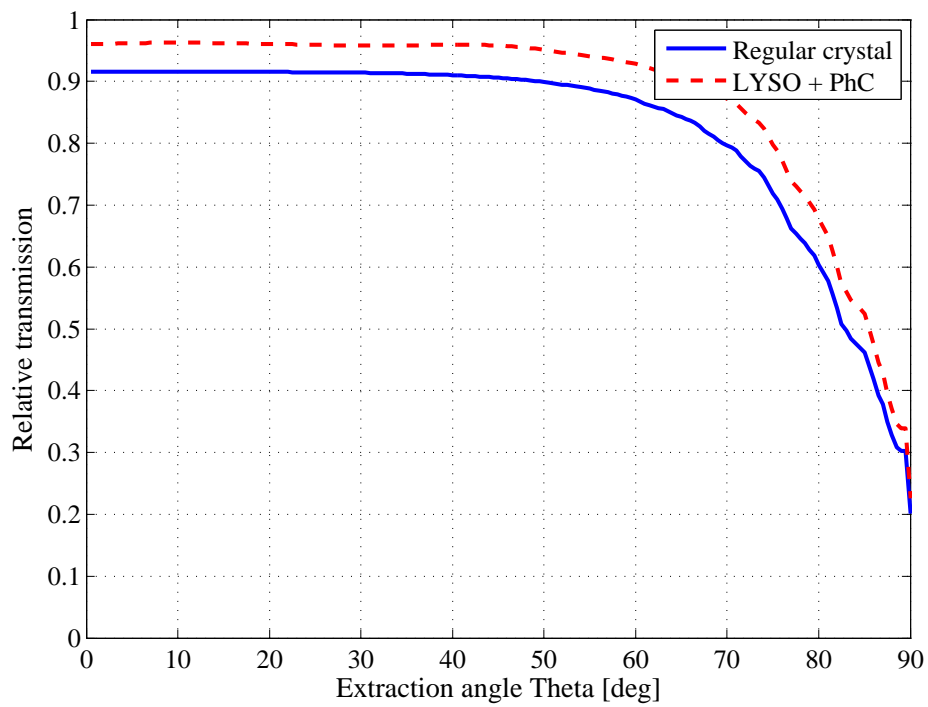
Figure 5.11: Transmission for un-polarized light as a function of the inclination angle Θ averaged over all azimuth angles φ (compare Figure 5.10). The PhC shows a gain of about 6-7% over the whole Θ range for an isotropic emitter.

5.4   Simulation Results

The optimization procedure was done for two different patterns, the triangular hole structure and a square pillar structure (see Figure 5.3 and Figure 5.4). The plot in Figure 5.5 shows the performance of the PhC in dependence of the lattice parameters. A clear maximum was found for a lattice constant of 300nm and a hole diameter of 180nm. Since the optimization routine also showed a good performance in other regions we designed a second triangular pattern at $a = 450nm$ and $D = 200nm$. A third structure with a square pattern was designed in addition, since this type of pattern can be produced in about a tenth of the time it needs to produce the triangular pattern in the electron beam lithography process. Regarding to our simulations, the square pattern is about 20% less effective compared to the triangular hole structure but the increase in the lithography process time made it a potential candidate for large area designs and therefore it had to be tested. All the design parameters of the three PhC structures and the regarding light extraction gain are summarized in Table 5.1.

Table 5.1: Design parameters for the three different lattice types and the regarding simulated light extraction gain. The Lattice constant a, the hole or gap diameter D and the thickness have been optimized to maximize the light extraction for the square and triangular pattern. The second triangular pattern was chosen to have a larger PhC pattern in case the parameters of the triangular pattern No. 1 turns out to be too small for the lithography.

Lattice type	Lattice constant $a[nm]$	hole or gap diameter $D[nm]$	Extraction gain
square (see Fig. 5.4)	640	120	100%
triangular 1 (see Fig. 5.3)	300	180	120%
triangular 2 (see Fig. 5.3)	450	200	100%

5.5 PhC influence on the Timing
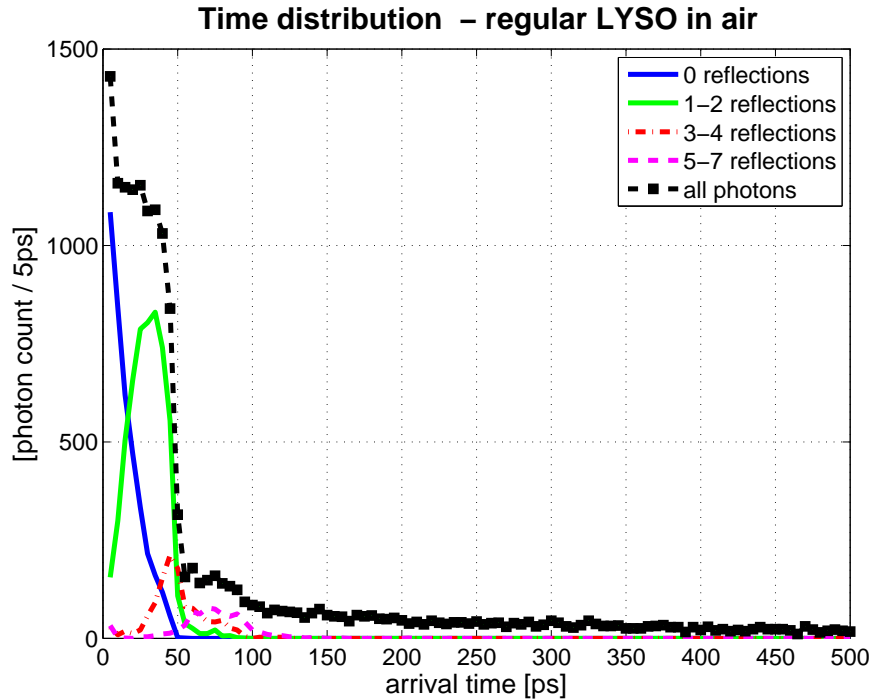
Figure 5.12: Time distribution of photons extracted at the exit surface of an unstructured crystal with no wrapping and no glue. The histogram shown in this plot has a bin size of 5ps. The black curve represents all photons, while the colored lines distinguish between the amounts of lateral reflections a photon has undergone before getting extracted. The arrival time is defined as the time it takes from the birth of the optical photon until it gets extracted. 160000 photons have been produced for this plot.

One of the main motivations of this work besides the enhancement of the number of extracted photons was the improvement of the timing performance of a scintillator. The basic idea is, that with a PhC grating, the photons are getting extracted the first time they hit the outcoupling side of the crystal. This theoretically increases the number of fast photons and decreases the number of photons getting back reflected and reappearing later. On the other hand there is the chance that the PhC structure also extracts a large fraction of late photons which has been undergoing multiple reflections of the side walls and therefore lowers the timing performance. With our Monte-Carlo tool (LITRANI) we can study the timing of the photons at any part of our conventional setup. PhC effects like band gaps or the extra ordinary light extraction cannot be simulated by the standard

version of LITRANI. Therefore, to study the influence of the PhC grating in this setup, the
LITRANI program was extended in a way that the reflection properties of a PhC grating
could be reproduced at any surface of the simulation setup. The following simulations are
taken from a PhC design which is a square pattern of silicon nitride pillars which has a
lattice period of 620nm and an air gap of 200nm in between. This design was chosen since
it corresponds to the development of one of our PhC samples. For simplicity, the PhC
reflection-map was implemented as a 1D vector mapping the PhC transmission behaviour
to the inclination angle Θ like shown in Figure 5.9.
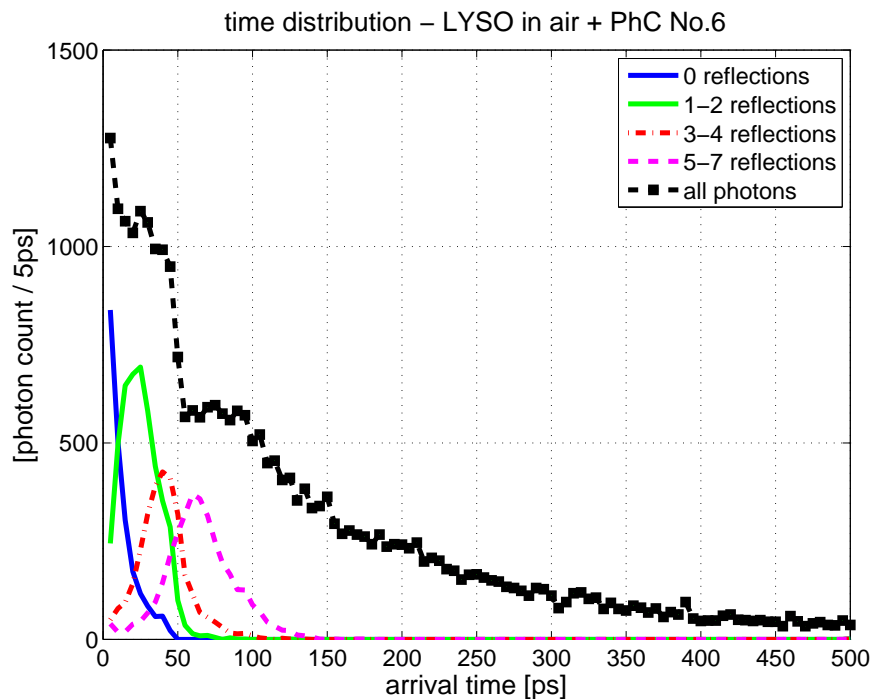
Figure 5.13: Time distribution of photons extracted at the exit surface of an LYSO crystal
having a PhC (Pattern No. 6 - see Chapter 6) at the Exit surface, again no wrapping
and no glue. The black curve represents all photons, while the coloured lines distinguish
between the amounts of lateral reflections a photon has undergone before getting extracted.
The histogram shown in this plot has a bin size of 5ps.

This means that the current version does not distinguish between different azimuth
angles. This approximation is valid since the photons of our crystal are equally distributed
over all azimuth angles at the exit surface. In Figure 5.12 the arrival time of photons
at the exit surface of an un-structured LYSO sample with the standard dimensions of

$1.2mm \times 2.6mm \times 5mm$ is shown. The arrival time is defined as the time a photon takes from its birth to reach the exit surface and get extracted. The black curve in the plot represents all photons while the coloured lines distinguish between the amounts of lateral reflections a photon has undergone before getting extracted. It can be seen, that it is very unlikely for photons to get extracted when they have already been reflected more than two times at the lateral surfaces. This can be explained by the fact, that light which has encountered already two reflections within a cuboid crystal is most likely to continue to be in the mode of total internal reflection (unless it gets diffused or scattered). This is of course only true if one does not use diffusive wrapping. In the PhC case (see Figure 5.13) this is different, the extraction face of the crystal has different reflection properties than the other fife sidewalls of the crystal, therefore also total reflection modes can be coupled to the outside once the hit the PhC structure. While we gain in the number of extracted photons, the PhC also extracts total reflection modes which has been encountering already many reflections and therefore are very slow. It is also visible, that the PhC decreases the number of direct photons (no lateral reflections), this can be explained by the reflection properties of the PhC for normal angle ($\Theta = 0°$) incidence (see reflection properties in Figure 5.9). To get an idea about the timing differences of the two configurations, a direct comparison of the time distribution of all extracted photons can be seen in 5.14 and a comparison of the timing of cumulated photon number can be seen in 5.15. At an approximate arrival time of 65ps the number of photons is already larger at the PhC sample than at the unstructured reference sample. In this simulation the total number of photons was set to 160000 to get appropriate statistics. The absolute gain of the number of photons between the PhC sample and the reference sample was calculated as a factor of 1.6. This can be calculated from Figure 5.15 as the ratio between the 14.5% of photon extraction (equals 23200 photons) from the PhC sample and the 9% photon extraction (which equals 14800 photons in the plot) of the unstructured reference sample. For a real world sample with an absolute light yield of 37000 photons/MeV this would mean 3330 photons for the reference sample and 5365 for the PhC sample which is in good agreement with values we observe in our measurements (see Chaper 7). The arrival time distributions in Figure 5.14 and Figure 5.15 are from a PhC design which could be observed after the lithography (lattice period of 620nm and a air gap of 200nm). This means that it is not an optimal pattern for the light extraction. When taking the original PhC design for this simulations (See Table 5.1) we actuially can show that the arrival time distribution is much better which is shown in Figure 5.16 and Figure 5.17.
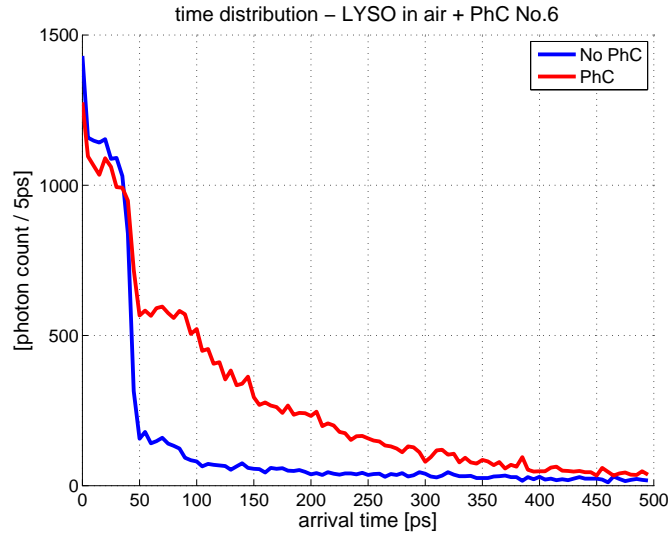
Figure 5.14: Comparison of the time distribution of all extracted photons of the two different configurations (see Figure 5.12 and Figure 5.13). The very fast component ($<$ 50*ps*) is lower at the PhC sample since the PhC surface has lower transmission for light hitting at normal incidence than the unstructured sample (compare Figure 5.9).
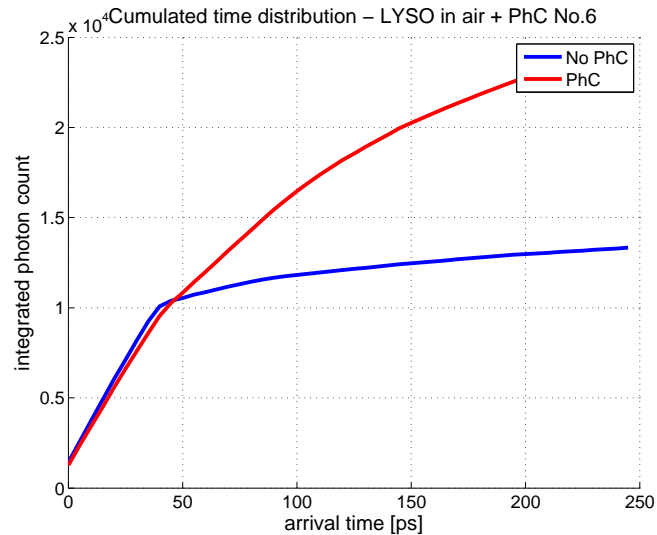
Figure 5.15: Integrated time distribution (from Figure 5.14). It can be seen, that at ∼65ps the number of photons are already larger at the PhC sample than at the unstructured sample. In this simulation the total number of photons was 160000.
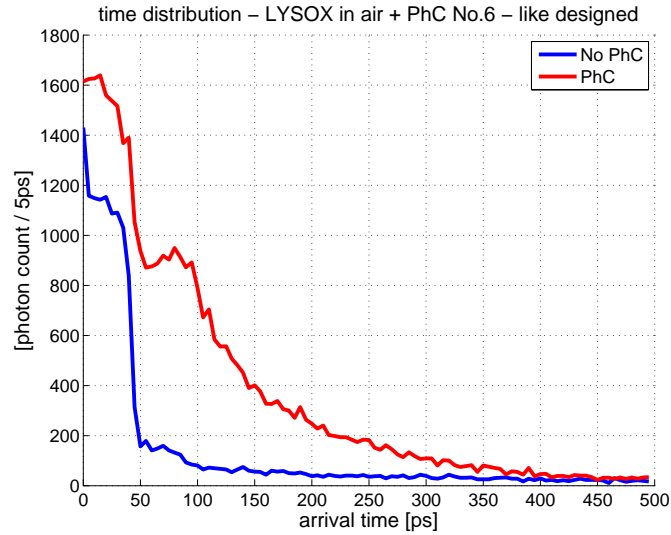
Figure 5.16: Arrival time distribution of all extracted photons of the reference crystal and an ideal PhC pattern (for the parameters see first row in Table 5.1).
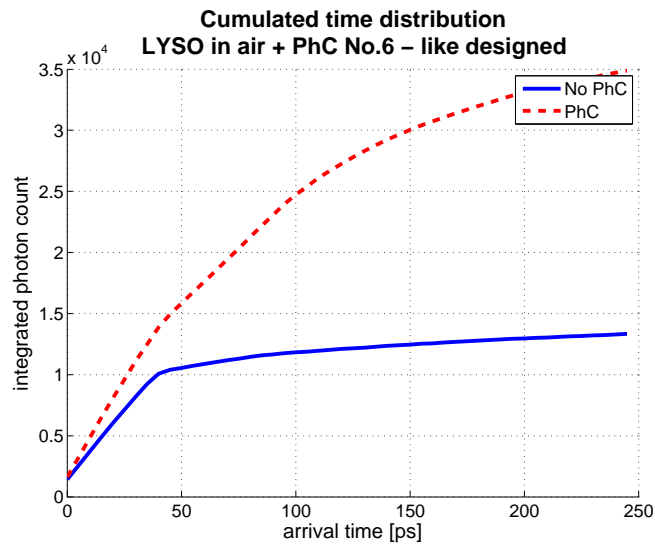
Figure 5.17: Cumulated arrival time distribution of the reference crystal and PhC (compare Figure 5.16). The PhC pattern gives already 50% more photons at an arrival time of 50ps. The overall light yield gain can also be estimated as a factor of 2.1 from this plot when comparing the number of photons at 250ps.

5.6   Conclusion

This chapter summarizes the different photonic crystal (PhC) simulation approaches of our work. The aim was to come up with a simulation method which can calculate the light extraction performance of a two dimensional PhC grating which is attached to the light out-coupling side of a heavy inorganic scintillator. The freely available CAMFR [96] simulation package was fulfilling these requirements. CAMFR is a Rigorous Coupled Wave Analysis (RCWA) tool to calculate the propagation of electromagnetic waves within one- or two dimensional periodic gratings. Two different PhC designs were tested, one triangular placed hole structure (see Figure 5.3) and one spare shaped pillar structure (see Figure 5.4) since the light extraction capabilities of both structures are similar. In particular, the triangular hole structure shows a 20% better light extraction performance but the square shaped pillar structure is eight to ten times faster in the lithography process (see Chapter 6 for details) and therefore both structures had to be tested. The two PhC structures used in our work can be characterized with three different parameters, the filling factor, the lattice constant and the pattern thickness. These three parameters were then optimized to extract as much photons from the scintillator to the outside world as possible. To see the exact effect of the PhC grating at the light out-coupling side of the scintillator, the reflection properties calculated by the CAMFR PhC program were implemented into the LITRANI Monte Carlo software. The results were showing a theoretical light yield gain of 60-120% compared to an unstructured reference sample. In addition, it could be shown, that the photonic crystal grating changes the timing distribution of extracted photons. If designed properly, this could potentially be used to improve the timing resolution of a scintillation based detector.

Chapter 6

Photonic Crystal Fabrication

Contents

The production of a PhC structure on top of a scintillating crystal is a non-trivial procedure. To the best of our knowledge, such a sample has not been produced so far. Therefore we were cooperating with the Lyon Institute of Nanotechnology (INL) which provided valuable knowledge, hands on experience and the right lab equipment for such an approach. For the PhC scintillator sample the standard nano lithography procedure for wavers using electron beam lithography was adapted to the special requirements of our base material. The whole process can be split up in four main parts: Sputtering, Resist spinning, electron beam lithography and reactive ion etching (see flowchart in Figure 6.1 and the according Figure 6.2). In the beginning of the following Chapter, an overview of the different nano lithography techniques is given. The four different lithography steps of our approach are then explained into more detail. At the end, the results of the latest PhC sample which has been developed by our group are shown. The PhC patterns were characterized based on scanning electron microscopy (SEM) images and problems and limitations of the approach are discussed.
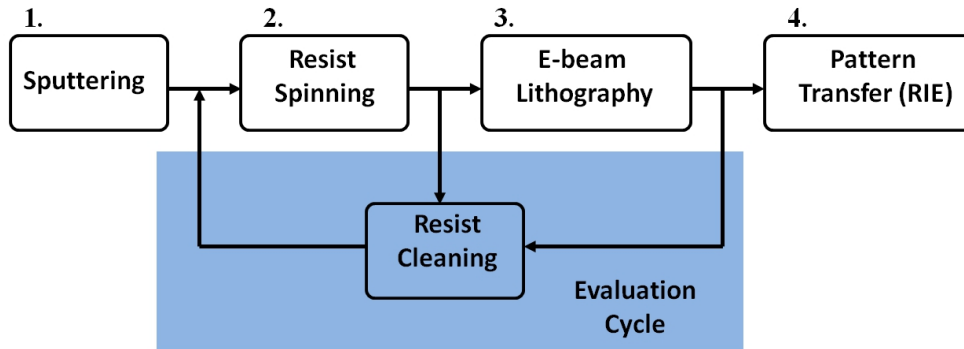
Figure 6.1: The four different steps in the PhC production. In the first step two auxiliary layers (indium tin oxide (ITO) and silicon nitride (Si_3N_4)) are deposited using sputtering technique. Afterwards, a resist is applied with spin coating. As the third step, the patterning of the resist is done using an electron beam microscope. The last step is the pattern transfer with a reactive ion etching reactor. The results of step two and step three can be evaluated and in case of errors the process can be repeated after cleaning the sample.
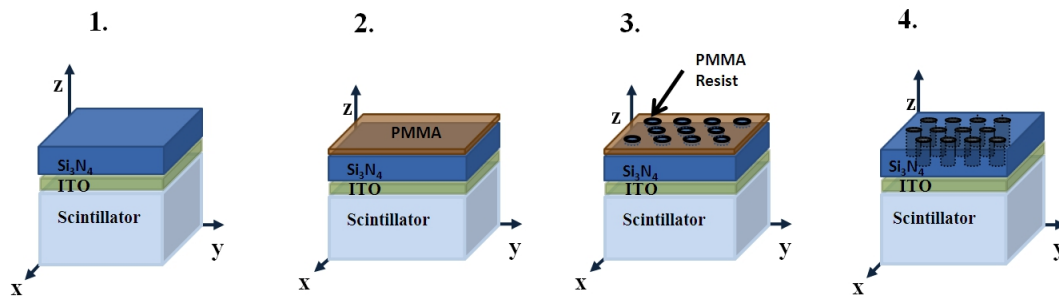
Figure 6.2: Sketch of the sample structure after the regarding four PhC production steps (compare Figure 6.1). It can be seen, that in the electron beam pattering process, just the resist is patterned while the actual PhC inside the silicon nitride is made in the last step by reactive ion etching.

6.1 Short overview of the different Nanolithography Techniques

For the pattering of materials in the nano scale, different techniques are existing. The right choice of the technique depends on several factors like cost, patterning speed and patterning area. While we have chosen to use electron beam lithography for our sample, there are several other possibilities which are shortly mentioned here.

6.1.1 Deep Ultraviolet Lithography

In deep ultraviolet lithography (DUV) light in the wavelength between $\lambda = 190nm....250nm$ is used which allows a minimum feature size of 50nm (see [100] [101]). The minimum feature size, also called resolution, is limited on the smallest image that can be projected on the waver or sample and the resolving capability of the resist. The imaging resolution is related to the wavelength λ and the numerical aperture NA of the imaging system: $Resolution \propto \frac{\lambda}{NA}$. It is mainly used in the microelectronics industry because of its high throughput. Since the mask is usually written by electron beam lithography (EBL) the DUV lithography is very slow and expensive for small amounts of samples and is therefore rarely used in prototyping.

6.1.2 Optical Interference Lithography

Optical Interference Lithography (IL) is a holographic approach where two or more coherent beams interfere to produce a standing wave in the form of the desired pattern [102]. The restriction for that approach is that the pattern has to be periodic in a way that can be reassembled by the superposition of plane waves. The advantage of Optical IL is the large area which can be exposed within a short time. The disadvantage of this method is the limitation in the pattern design since only periodic structures which can be reassembled by superposition of plane waves can be produced.

6.1.3 Nanoimprint Lithography

The nanoimprint lithography (NIL) technique combines the high throughput of a "mask-based" lithography approach with the accuracy and resolution of a low-throughput method like EBL. In the patterning process, a stamp (mold) containing the negative of the desired pattern which was previously manufactured using highly accurate but low throughput approaches is used to mechanically stamp a resist material [103]. The pattern in the resist

can then be transferred using standard pattern transfer methods like reactive ion etching (RIE).

6.1.4   Electron Beam Lithography (EBL)

The goal of EBL is the patterning of polymer based resist layer with an electron beam. The serial process exposes a single area at a time, this has the disadvantage of being slow and therefore one is limited in the overall size of the pattern. The advantage is the flexibility in the pattern design; essentially all possible 2 dimensional pattern designs can be manufactured. Because the method is using an electron beam instead of light for the resist exposure it can beat the resolution of optical lithography systems which are usually limited by the Rayleigh resolution criterion ($Resolution \propto \frac{\lambda}{NA}$). Depending on the whole system configuration, a feature size down to 10 nm can be achieved. For rapid prototyping of small quantities it is common to use a standard scanning electron beam microscope (SEM) with some additional hard- and software to get an EBL system. In the patterning process, the electron beam of the scanning electron microscope is connected to an external control system which writes the desired pattern into the resist. A special e-beam resist has to be used for that approach which is usually a polymer which is sensitive to an electron beam in the energy range of such a system ($1 - 30keV$). The exposed areas become chemically soluble and can be removed by a developing agent.

6.2   PhC Manufacturing using EBL

6.2.1   Step 1 - Sputter Deposition

Since the scintillator is not etched directly, an auxiliary layer of silicon nitrate (Si_3N_4) is applied in the first step by sputter deposition. Sputter deposition is one of several methods of physical vapour deposition (PVD). It is widely used in the semiconductor industry to deposit thin films of various materials. The silicon nitride is used later on as a transfer material for the actual PhC pattern since the scintillator itself cannot be etched by standard nano etching techniques. The Si_3N_4 is transparent in the emission wavelength of the scintillator and has an index of refraction between $1.8 - 2.0$ at 420nm (Depending on the deposition quality). In addition, an indium tin oxide (ITO) layer is sputtered in between for improving the electrical properties of the sample since ITO is a good electrical conductor and is optically transparent.

6.2.2   Step 2 - Spin Coating

Covering the substrate with an electron beam sensitive material is usually the first step after the sample cleaning. The electron beam resist has to be a high-molecular weight polymer dissolved in organic solvents. In our case we were using NANO 950 PMMA A4 [104] which is a 4% PMMA resist dissolved in Anisol. The aim in the coating step is to get a thin, uniform and defect free polymer film on top of the substrate.

6.2.2.1   Electron Beam Resist Characteristics

The electron beam resist which is commonly a polymethylmethacrylat (PMMA) or a Copolymer is characterized by a number of parameters (see Table 6.1).

Table 6.1: Overview of the different electron beam lithography resist capabilities.

Resist	Tone	Resolution	Contrast	Etch Resistance	Dilutions	Sensitive to white Light
PMMA	Positive	Very High	Low	Poor	Many	No
P(MMA-MAA)	Positive	Low	Low	Poor	Many	No
NEB-31	Negative	Very High	High	Good	Several	Yes
EBR-9	Positive	Low	Low	Poor	Single	No
ZEP	Positive	Very High	High	Good	Several	Yes
UV-5	Positive	High	High	Good	Several	Yes

An essential parameter is the tone which describes whether the exposed part or the non-exposed part of the resist becomes soluble in the photoresist developer (Positive=exposed parts gets removed, e.g. PMMA). The clearing dose (a.k.a. dose to clear) D_{cl} is defined as the amount of charge per unit of area (usually $\mu C/cm^2$) which is necessary to completely develop a large area (area larger than the range of the proximity effects). In addition a high resist contrast is desired, which describes the ratio between the minimal dose D_0 which starts having an effect on the resist to the dose which is necessary to remove 100% of the resist D_{100}. A higher resist contrast would therefore mean better vertical resist profiles.

6.2.2.2   Resist Spinning

Spin coating is a common technique to get the former mentioned properties (see Figure 6.4). The seemingly simple procedure can be quite tricky due to strict requirements towards uniformity and thickness and some unexpected resist behaviour. One of the unwanted effects in spinning is caused by the surface tension between resist and air which

is leading to boarder effects called "edge beads" (see Figure 6.4). The surface tension at the edge is an additional force directed inwards adding to the viscous force and therefore stops the flow of the resist [101]. This edge bed can cover 1mm - 2mm of the surface from the edge inwards. The thickness can be 10 - 30 times bigger than the rest of the resist. If the wafer is 10cm in diameter, this is not considered a big problem since it is just a small fraction of the overall surface. But in an industrial production line it is still considered a problem since the resist from the edge bead is containing the handling tools which usually grab the wavers at the borders. Therefore the edge bead is usually removed in an additional process. In our case, the edge bead effect has prevented us from using small crystal samples (surfaces smaller then 2mm in $\varnothing$) because there the edge effect became predominant over most part of the surface. As a result, we were using bigger crystal samples ($10mm \times 10mm$) where the border regions were skipped in the lithography. The quality of the resist layer in spin-coating is controlled by several parameters:

- Resist adhesion to the substrate

- Viscosity of the resist

- Acceleration of the spinning table

- Speed of the Spinning table

- Spinning time

The thickness is manly controlled by the spinning speed and the viscosity of the resist. In literature [105][101] the correlation between resist thickness and these two parameters is described as:

$$thickness \propto \frac{v^x}{\sqrt{\omega}} \qquad (6.1)$$

where $\omega[rpm]$ is the spinning speed in rounds per minute, v is the viscosity and x is a parameter varying between 0.4....0.6. For our ebeam resist (PMMA A4) the following spinning curve is found in the data sheet:

The curves in the figure just gives an estimate about the correlation between the thickness and the spin speed, the actual thickness can vary due to different environment variables like surface adhesion or temperature. Therefore the thickness has always to be experimentally verified. The spin speed is limited to a certain range. Like seen in Figure 6.3 it is usually between $1000...5000rpm$ since a too low or too high speed produces

E-beam-resist NANO 950K PMMA A4, in anisol (MicroChem)
Result of measurements by FTP-reflectometer
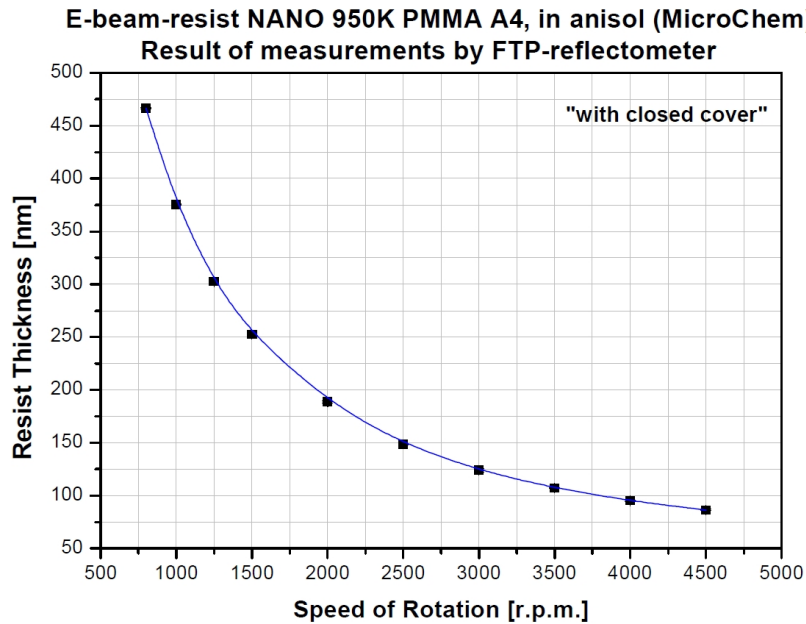
Figure 6.3: Spin speed versus film thickness curve of NANO 950K PMMA A4 [106]

irregularities in the resist layer. This means that one has to change the viscosity by concentrating or diluting the resist when the range of thicknesses given by 6.3 is not enough.

6.2.2.3   Substrate Priming

To get adequate adhesion properties on the deposited Si_3N_4 layer for the spinning of the resist one has to prepare the substrate by priming. Priming with chemical agents like hexamethyldisilazane (HMDS) or trimethylsilyldiethylamine (TMSDEA) which are usually used for silicon oxide substrates are lowering the surface hydrophilicity. For our Si_3N_4 film it is appropriate to use oxygen plasma for the activation of the surface [107]. On our sample we could achieve already good spinning results at an oxygen plasma activation time of 120s at 400W forward power and an oxygen flow of 500 sccm (standard cubic centimetres per minute).

6.2.2.4   Resist baking

The backing after the spinning is changing the resist properties in several ways. The procedure basically just consists of heating up the substrate with the resist at a predefined temperature and a certain time. The heating leads to solvent removal, stress reduction
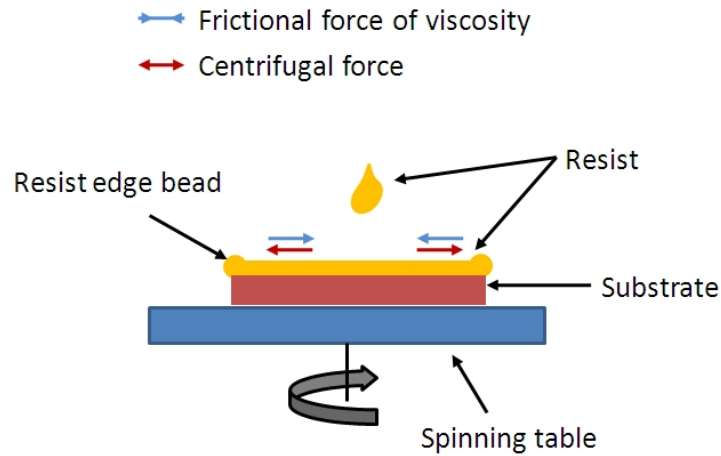
Figure 6.4: Spin-coating of the electron beam resist by pouring an appropriate amount of dissolved resist material (e.g. PMMA in anisol) in the middle of the sample substrate and spinning the table at a certain speed and time. Centrifugal forces push the resist towards the edge where excess resist is flung of. While the resist is getting thinner the centrifugal forces are getting smaller too since it is proportional to the mass of the resist. Also the solvent dries up and therefore the viscosity of the resist is getting bigger (up to 7-10 times [100],[101]). Once equilibrium between the two forces is reached the mass flow stops but the thickness is still decreasing since the resist is still drying up.

within the resist and planarization. For that, one has to heat up the resist above the glass transition temperature T_g which is usually between 90-180 degrees. In our case of PMMA resist the data sheet gives a T_g of 95-106 degrees. On the other hand one has to avoid too high temperatures which are causing a decomposition of the polymer. A heating at 180 degrees for 30 minutes turned out to be sufficient for our sample.

6.2.3 Step 3 - Electron Beam Lithography

The optical resolution requirements of our PhC structure were demanding a highly accurate lithography technique. Since our PhC design contains features as small as 200nm and requires a minimum tolerance of 10% to make it work efficiently, it comes down to a lithography method who can resolve at least 20nm structures. Also we were interested in fast prototyping of single pieces of a few different PhC designs which is enough to proof our concept in the first stage. Electron Beam Lithography (EBL) was a perfect match for our constraints and with the nano-technology lab in Lyon we had a competent partner to realize such a sample.

6.2.3.1   General Operating Principle

The goal of EBL is the patterning of polymer based resist layer with an electron beam. The serial process exposes a single area at a time; this has the disadvantage of being limited in the overall size of the pattern but brings flexibility in the pattern design. Depending on the whole system configuration feature sizes down to 10nm can be achieved. The limiting factor for the resolution here is not the diffraction of the electron beam but the forward- and back-scattering of the electrons in the resist and the substrate. For research purposes it is common to use a standard electron beam microscope with some additional hard- and software to get an EBL system. (see Figure 6.5).
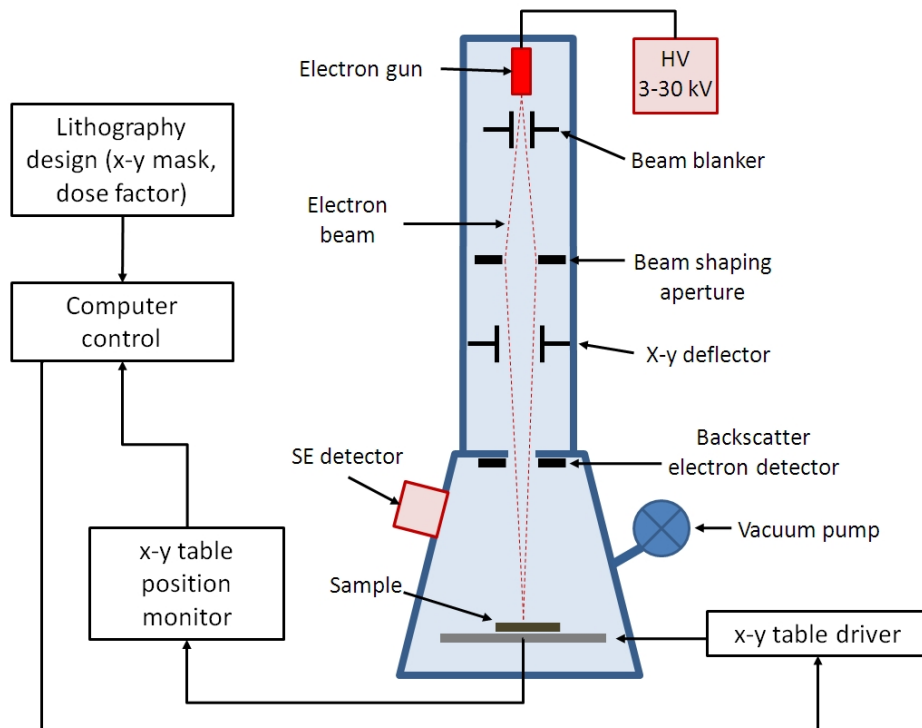
Figure 6.5: Scanning electron beam microscope in a lithography configuration. The lithography design file usually consists of a binary x-y mask in addition to some area dose information. The detector parts (secondary electron (SE) and the backscatter electron detector) are passive during the lithography but they are used for the sample alignment procedure.

6.2.3.2   Proximity Effects

The proximity effect is caused by unwanted interactions of the e-beam electrons with the resist (forward scattering) and the substrate (backscattering). According to [108] it is the main limiting factor of EBL. In figure 6.6 one can see a Monte Carlo simulation of the scattered electrons within the resist and the substrate. From the figure it becomes clear that the scattering effects correlating with the acceleration voltage and the substrate and resist material.
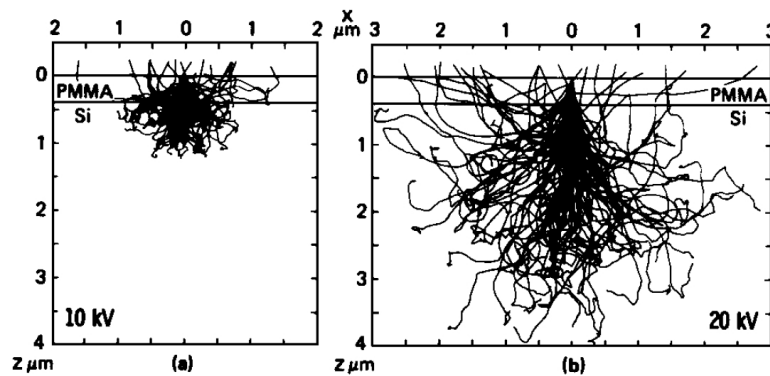
Figure 6.6: Monte Carlo simulation of 100 electrons in PMMA film on silicon [109]. It can be seen, that the amount of scattering shows a nonlinear correlation to the accelerating voltage.

Forward scattering is elastic and inelastic scattering of the incident electron and causes a broadening of the electron beam which leads to a conical exposure along the resist depth. It also generates secondary electrons in the range of 2-50eV. The source of the backscattering is the electrons which undergoes strong deflections in the substrate and may re-enter the resist from the substrate side.

6.2.3.3   Resist Development

The PMMA (polymethyl methacrylate) resist used for the EBL is a high resolution, high contrast positive tone resist designed for e-beam and deep UV lithography. Patterns are formed through photo scission of the polymer backbone, which reduces the molecular weight and increases the develop selectivity [101]. The developer used for this type of resist is a mixture of MIBK (Methylisobutylketon) and IPA (Isopropyl alcohol). The developer is usually used in the following ratios (MIBK:IPA): 1:1, 1:2 or 1:3 [110]. Mixtures containing higher amounts of solvent (MIBK) are more active and offer higher throughput, while mixtures containing higher amounts of the non-solvent (IPA) are less active and can enable

a higher resolution. The configuration for a successful development of our sample was the following: a bath in MIBK:IPA(1:1) for 45 seconds, stopping in IPA for 60 seconds and drying with N_2 afterwards.

6.2.4 Step 4 - Reactive Ion Etching

The pattern itself is then etched into the substrate by reactive ion etching (RIE). RIE uses fluorine-containing chemically reactive plasma to transfer the PhC-pattern from the PMMA resist into the Si_3N_4. The plasma is generated in a vacuum chamber by an electromagnetic field and a mixture of different reactive gases (see 6.7). In particular, the alternating electric field caused by a RF generator is stripping of the electrons of the gas. Due to their lower mass, electrons are much more deflected by the oscillating field than the heavier positive ions and are therefore more likely to be absorbed by the surrounding chamber or target. Because the chamber is grounded, the bottom plate is DC isolated and therefore builds up a negative charge. Since the positive ions from the plasma are moving in the direction of the negative bottom plate, an anisotropic etch profile can be created at the target. The anisotropic etching ensures a constant hole diameter from the top to the bottom of the PhC slab, in contrast to the typical isotropic profiles of wet chemical etching. The control of the etching rate is related to many parameters, the most important are the chamber pressure, the gas flow, and the RF power.
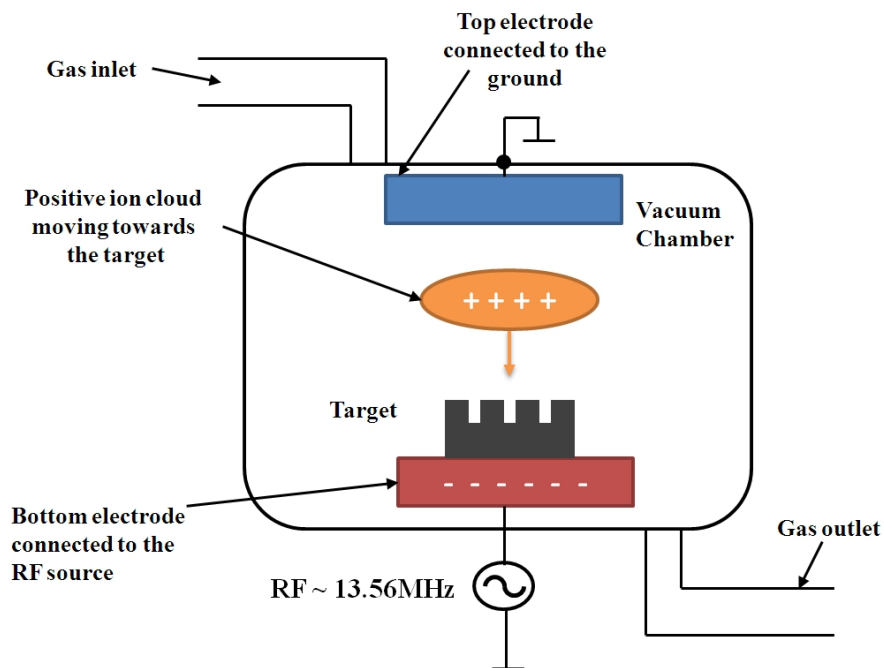
Figure 6.7: Reactive ion etching chamber (RIE). An RF generator produces plasma which is moving towards the negative charged bottom electrode which is causing an isotropic etching profile.

6.3   Lithography Results

6.3.1   PhC Pattern Parameters

Due to over and under exposure, bad electron beam calibration or bad etching configuration the actual PhC patterns deviates from the original design. These sources of error can be kept small by repeating the whole lithography steps several times and figuring out the right parameters by trial and error. This is very time consuming and has been done throughout several cycles until we got a reasonable result which is sufficient to prove the concept. To find out the quality of the lithography, the PhC parameters of the samples are usually checked by a scanning electron microscope. The lattice period is a parameter which usually fits well to the design and the accuracy is only dependent on the e-beam lithography calibration. A more prevalent error is the filling factor (size of the holes or gaps in relation to the rest of the structure) since this parameter is not only controlled by the e-beam lithography procedure but also dependent on the exposed dose and the developing and etching afterwards. The holes were made by a point exposure to speed up the lithography. This means, the hole diameter is mainly controlled by the electron dose the resist gets for each hole. In addition it depends on the beam diameter and the resist thickness and type. All this variables made it very hard to analytically estimate the hole diameter, therefore an experimental technique was used. This takes several trials to find out the right parameters to get the thickness of the actual design. The results of these trials can be seen in the scanning electron images of Figure 6.8. In Table 6.2 the comparison of the design parameters with the parameters of the actual pattern observed with the SEM can be seen.

Table 6.2: Pattern parameters of the design and the estimated parameters of the real PhC pattern observed in the SEM. To estimate the over all development we take into account the lattice period and the gap or hole diameter but also the shape of the holes or pillars. Thats the reason why p2, p5 and p6 have a good development even though the gap diameter from p5 and p6 deviates more from the design than for p3 and p4.

Pattern	P1	P2	P3	P4	P5	P6
Period measured [nm]	275	445	620	616	628	622
Period designed [nm]	280	450	640	640	640	640
Gap or hole diameter measured [nm]	215	170	120	146	200	200
Gap or hole diameter designed [nm]	170	200	110	110	110	110
overall development	−	++	−	-	++	+
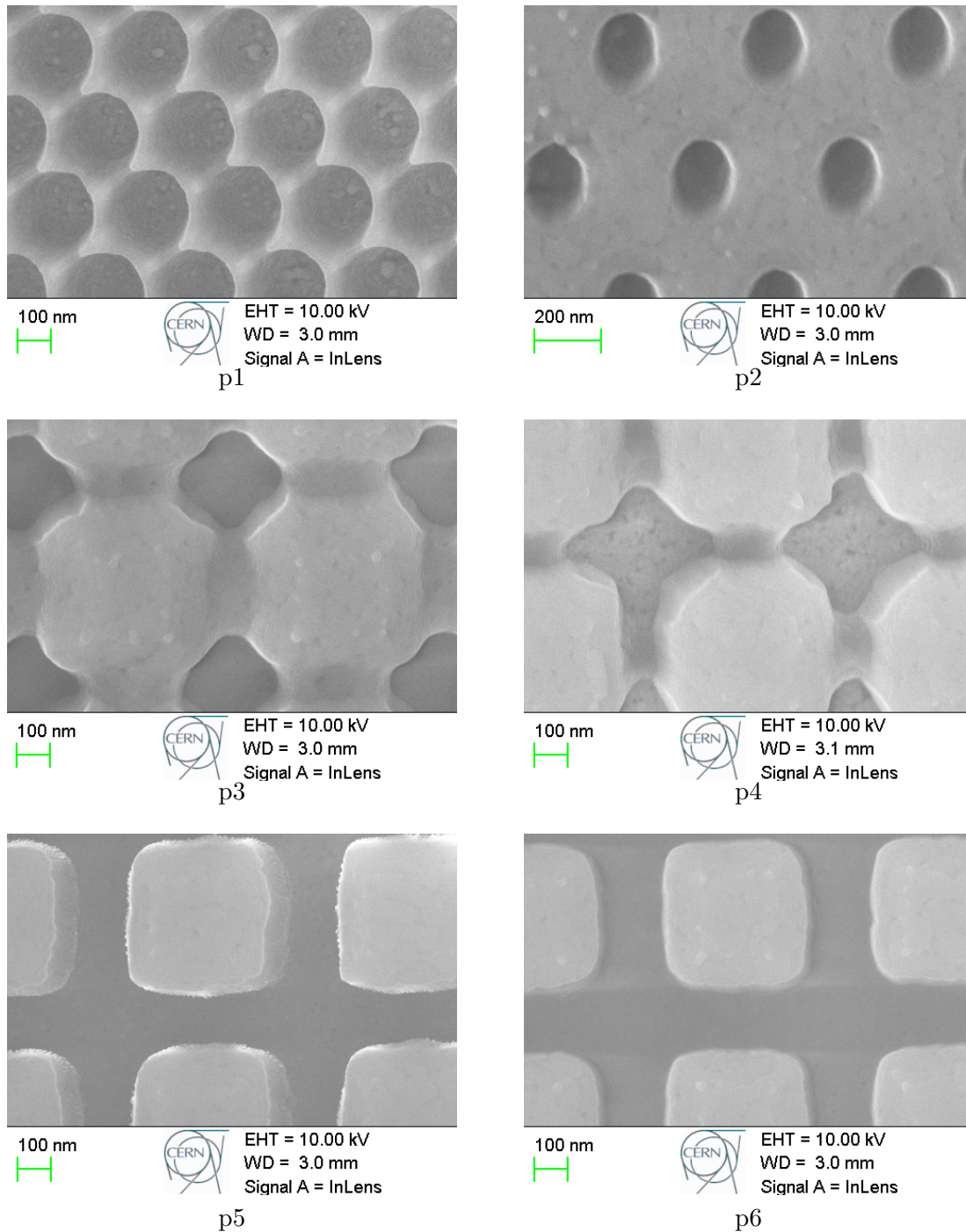
Figure 6.8: Scanning electron microscopy (SEM) images of the six different PhC structures made on top of a LSO sample. The pictures are made with a $40.000\times$ fold magnification using the inlens camera of a Zeiss SEM. The regarding pattern parameters estimated from the pictures and the regarding parameters of the design can be seen in Table 6.2.

6.4   Conclusion

This Chapter deals with the different aspects of the production process of our photonic crystal scintillator sample. To demonstrate the light diffraction effects which could be shown by our simulations, an actual sample had to be produced. In particular, a sub-wavelength scaled grating with a lattice period between $280-600nm$ and a design tolerance of $\pm 10nm$ had to be produced on top of the light out-coupling side of a scintillator. To quantify the effect using our measurement setup for $662keV$ gamma photons, it was necessary to cover several square millimetres of a scintillator. We decided to use electron beam lithography (EBL) for the nano patterning of a polymer based mask and reactive ion etching for the pattern transfer. EBL is known for fast and cheap prototyping of such structures but is limited in the patterning throughput. Since the scintillator material is an unusual material for nano lithography, we came across a number of difficulties which had to be overcome step by step involving a repetitive cycle of runs. First of all it was necessary to deposit silicon nitride on top of the scintillator as a pattern transfer material, since the lutetium oxyorthosilicate (LSO) scintillator cannot be etched by standard lithography procedures. Tests have also been showing that the conductivity of the base material is not sufficient for an accurate EBL, therefore an additional layer of indium tin oxide (ITO) was deposited to improve the electrical conductivity and to drain the charges from the electron beam. After every deposition, the silicon nitride layer had to be checked by transmission end ellipsometry measurements to ensure the transparency and index of refraction which should be at least 1.8 but can be lower due to a miss adjustment of the sputtering machine or due to impurities in the deposition chamber. Another problem was the spinning of the resist layer. Since we could not get any good results when using small (surface areas of $2-4mm^2$) scintillators in the spinning process we decided to use a big (surface area of $10 \times 10mm^2$) crystal and cut out smaller after the whole lithography process. After several trials, we figured out a set of parameters for the different lithography processes which lead to a successful development of six different PhC patterns on top of a $10 \times 10 \times 5mm^3$ large LSO crystal. Since we wanted to have individual crystals with a full PhC coverage of one side, we had to cut out the different samples using a diamond wire saw. After the cutting, the sidewalls had to be polished again which damaged two samples. Finally, we had 4 different PhC covered LSO crystals with the dimensions of $1.2 \times 2.6 \times 5mm^3$ and one reference sample cut from the same base material.

In the scanning electron images of Figure 6.8, the different pattern quality can be seen. Some patterns are overexposed and some are slightly underexposed. The summary of the pattern measurements and the deviation to the actual design can be seen in Table 6.2. To compare the result with the design, several more factors has to be taken into account then only the lattice constant (or lattice period) and the hole or gap diameter. It can be seen e.g. that pattern p3 and p4 are not completely developed and etched therefore they have different gap diameter on different areas and also the gap is not fully etched at some regions. The gaps in p5 and p6 on the other hand, even if bigger than the design, are completely etched and the pillars have an almost square shape.

Chapter 7

Characterization and Performance of the Photonic Crystal Scintillators

Contents

7.1 Characterization of the Photonic Crystal Slabs

As described in the previous Chapter, standard nano-lithography techniques like reactive ion etching (RIE) does not work on our scintillators (LYSO, LSO, BGO) since they are not chemically reactive to the plasma used in RIE. To be able to perform lithography on our scintillators two additional layers were deposited which were silicon nitride (Si_3N_4) and indium tin oxide (ITO). While ITO was used to improve the electrical conductivity of the whole setup the Si_3N_4 was deposited as an auxiliary layer for the pattern transfer. ITO and silicon nitride are known for its good transparency and has a similar index of refraction than the scintillating material [111]. To ensure the optical properties of the deposited material as well as the correct PhC parameters, we performed a series of tests

113

on them.

Since the scintillator (LYSO, LSO, BGO) cannot be etched with standard nano-lithography techniques like reactive ion etching (RIE), silicon nitride

7.1.1   Characterization of the deposited Layers

For the deposition of the ITO and Si_3N_4 layer we used a MRC-822 sputtering system. The sputtering rate as well as the quality of the applied layers can vary in between different samples. The purity and therefore also the optical properties of the ITO as well as the silicon nitride layer is influenced by the different settings of the sputtering system, like RF-power density, vacuum level and gas-flow adjustments ([112], [113]). But apart from all the values which can be controlled in the system there are also parameters which cannot be determined, e.g. the sputtering rate changes with the RF-power density $[W/cm^2]$ and therefore with the electrical conductivity of the substrate. In our case the scintillating crystal is a very good electrical insulator and therefore they change the sputtering rate when compared to electrical conducting materials. In addition we observed different optical properties of the deposited films when using PDMS as a mechanical support for small crystals inside the vacuum chamber. Due to all this uncertainties we had to evaluate the thickness and the index of refraction by additional measurements:

- Thickness Measurements:
  The thickness of the Si_3N_4 layer essentially determines the thickness of the PhC pattern since in the pattern transfer procedure the pattern is etched until the bottom (in our case ITO) is reached. Hence the control of the layer thickness is of great importance. The ITO- as well as the Si_3N_4 layer thickness was measured by successively covering parts of the sample in the sputtering and measuring the resulting step with a profilometer. With the recorded sputtering time for each deposition and their resulting thickness we could determine a sputtering rate for each configuration.

- Index of Refraction:
  The sputtering system is usually used for standard silicon wafers ($\varnothing = 10...100mm$, thickness=275-775μm) and has to be adapted to the new sample material (LYSO, LSO) and its size (¡$4mm^2$, height=5-7mm). Due to miss configurations or fluctuations of the vacuum level the quality of the sputtered materials can change [114]. To ensure a certain index of refraction, which has great significance for the PhC, we were using ellipsometry for the determination of the index of refraction of the sputtered material for each sample. For reasons not fully understood, we could measure
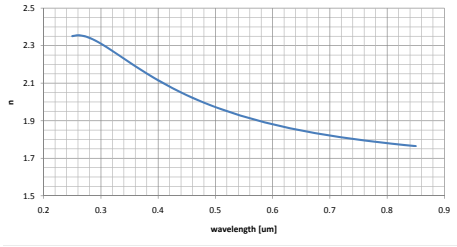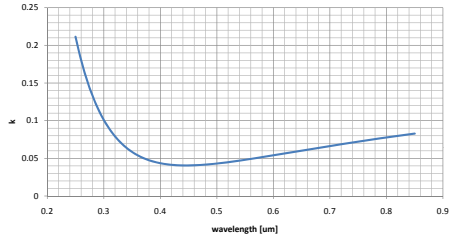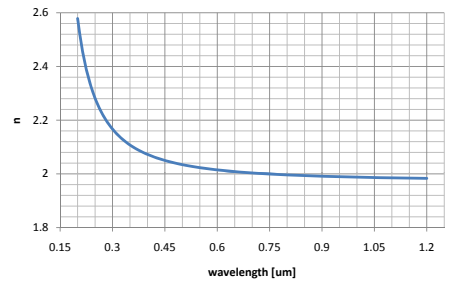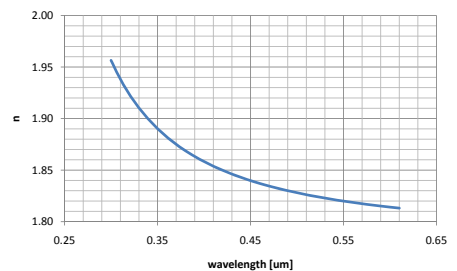
Material	Real part **n** of the refractive index of ITO	Imaginary part **k** of the refractive index of ITO (extinction coefficient)
ITO [115]		
Si_3N_4 [116]		insignificant
LYSO [37]		insignificant

Table 7.1: Imaginary and real part of the complex refractive index of the materials used in the PhC.

an index of refraction between 1.5-1.9. Most likely fluctuations in the vacuum by air leaks were causing an additional deposition of silicon oxi-nitride ($SiON_x$) and silicon oxide (SiO_2) which has a lower index of refraction (see Table 7.1 and 7.2).
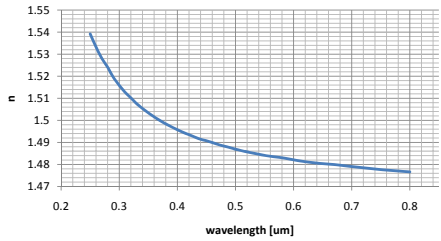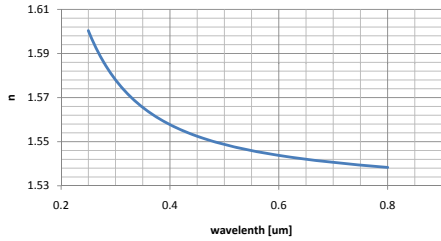
Material	Real part **n** of the refractive index of ITO	Imaginary part **k** of the refractive index of ITO (extinction coefficient)
SiON [115]		insignificant
SiO_2 [115]		insignificant

Table 7.2: Imaginary and real part of the partly complex refractive index of the materials used in the PhC.

7.1.2   Scanning Electron Microscope Imaging

To evaluate the results, all samples were observed with a scanning electron microscope (SEM) after the pattern transfer. The six different patterns which were manufactured on top of the $10mm \times 10mm \times 5mm$ large base crystal and the according SEM pictures can be seen in Figure 7.1.

Because of an uncertainty of $\pm 30\%$ in the resist thickness of the actual sample, the dose-factor for the e-beam process could not be determined exactly. This uncertainty can lead to over- or underexposure of the resist and a deviation of the pattern as a consequence. Due to this fact, we exposed several patterns with different dose-factors so that we could experimentally figure out the right dose after the lithography. The SEM pictures showed the best agreement on pattern Nr. p6 (right picture in Fig. 7.2). On pattern p3 (left picture in Fig. 7.2) we can see the same pattern when underexposed.
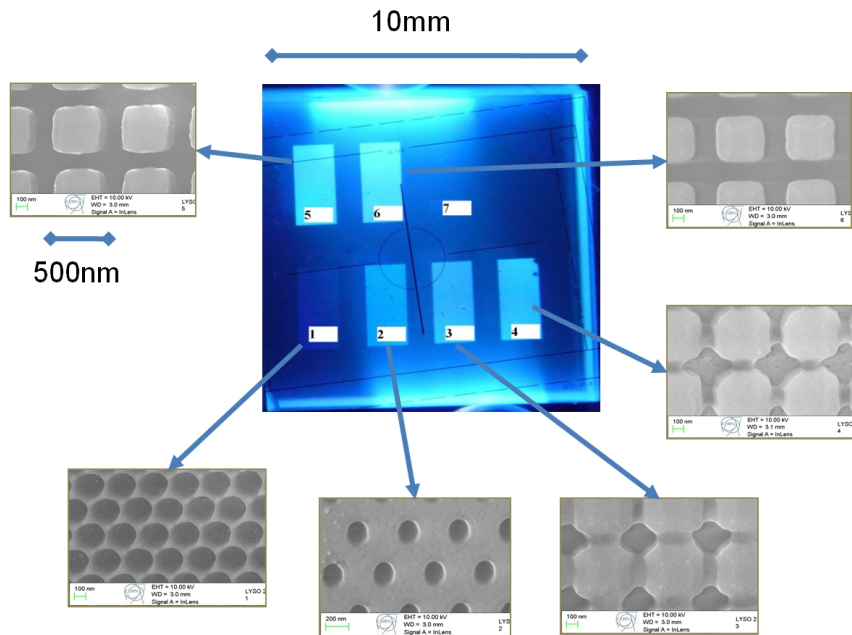
Figure 7.1: Scanning electron pictures of the six different PhC patterns produced on top of the $10mm \times 10mm \times 5mm$ large base LSO crystal.

a

b
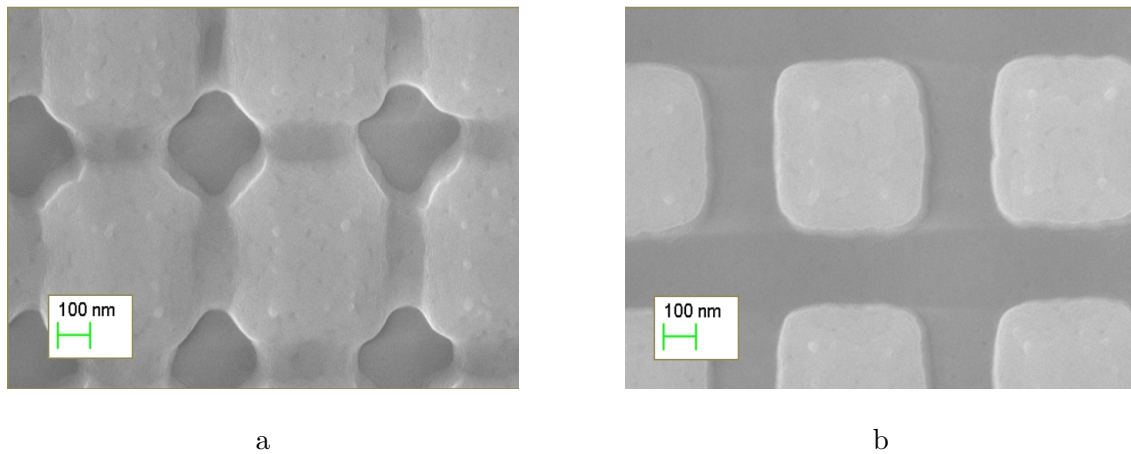
Figure 7.2: Scanning electron microscope pictures of the square pillar structure etched into the silicon nitride layer on top of the scintillator. The pattern is of the same design (design parameters: $a = 640nm, d = 500nm$) but with different dose factors. In pattern p3 (left) one can see the effect of underexposure whereas the dose factor for p6 (right) lead to the closest match to the pattern designs.

b   b
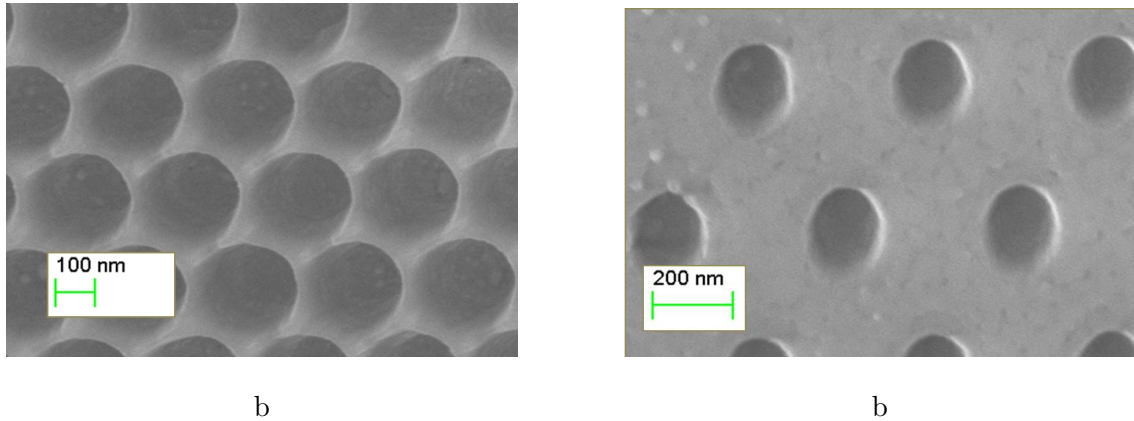
Figure 7.3: Scanning electron microscope pictures of the triangular placed PhC structure etched into the silicon nitride layer on top of the scintillator. In pattern p1 (left, design parameters: $a = 280nm, d = 170nm$) we have severe over-exposure. On pattern p2 (design parameters: $a = 450nm, d = 220nm$) we have under-exposure.

7.1.3   Pattern inspection by Energy Dispersive X-ray Spectroscopy

Energy Dispersive X-ray Spectroscopy (EDS or EDX) is a method for the chemical analysis of the sample. In this method the electron beam of a scanning electron microscope (SEM) was used to excite characteristic X-ray emission from the specimen. In particular, the electron beam ejects electrons from the inner shell of atoms and the resulting holes are replaced by electrons of higher shells. Due to the energy difference between the higher and lower shell, X-rays with a distinctive energy are released when a hole is filled. The energy can be measured using an energy dispersive spectrometer and since it is distinctive for most elements, the exact chemical composition can be related to it. For our PhC sample we used this method to investigate the quality of the deposited material which was indium tin oxide ITO and silicon nitride Si_3N_4. Due to a number of reasons (vacuum problems, outgassing, or polluted sample materials), impurities can occur inside the vacuum chamber of the sputter deposition reactor. As a result, the quality of the depositions can be changed and this can also affect the optical properties of the structures. As an example, we had to much oxygen in the vacuum chamber due to a vacuum leak which lead to the formation of a certain amount of silicon dioxide (SiO_2) and silicon oxi-nitride ($SiON_x$)which has a lower index of refraction than Si_3N_4 and therefore should be avoided. Using EDX the chemical composition of the different areas on the pattern can be investigated on small surface areas ($0.5\mu \times 0.5\mu$), for example inside and outside a hole of a PhC structure. With this method it could be checked that the holes etching was complete since you do

not see silicon in the spectrum but indium and tin which was coming from the ITO when the whole silicon nitride is etched (see Figure 7.4). For example, several samples had to be excluded because of bad optical properties of the deposited silicon nitride layer due to abnormal light absorption. Following investigations by EDX measurements showed that impurities of carbon and oxygen ini the Si_3N_4 layer were causing the observed absorption problems (see Figure 7.5).
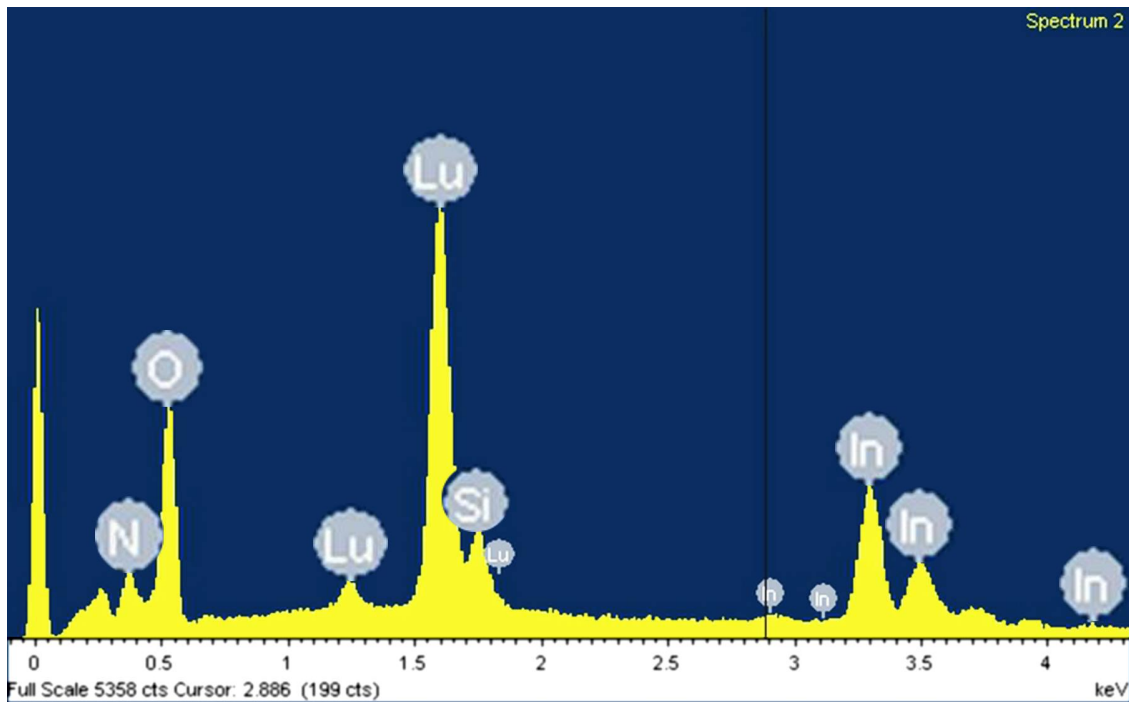
Figure 7.4: Energy-dispersive X-ray (EDX) spectrum of a fully etched silicon nitride area. In this spectrum the characteristic x-rays emitted from the sample when bombarded with electrons from the SEM is shown. The electron bombardment ejects electrons of the inner shell of the specimen, the electron hole is then filled by electrons of higher shells and the energy difference of the electron between these two shells is emitted as the characteristic x-rays of the regarding material. It can be seen, that there is almost no signal left from the silicon (Si) but a strong occurrence of indium (In) from the ITO and already some lutetium (Lu) from the LSO which is caused by electrons penetrating the only $70nm$ thick ITO layer.

a

b
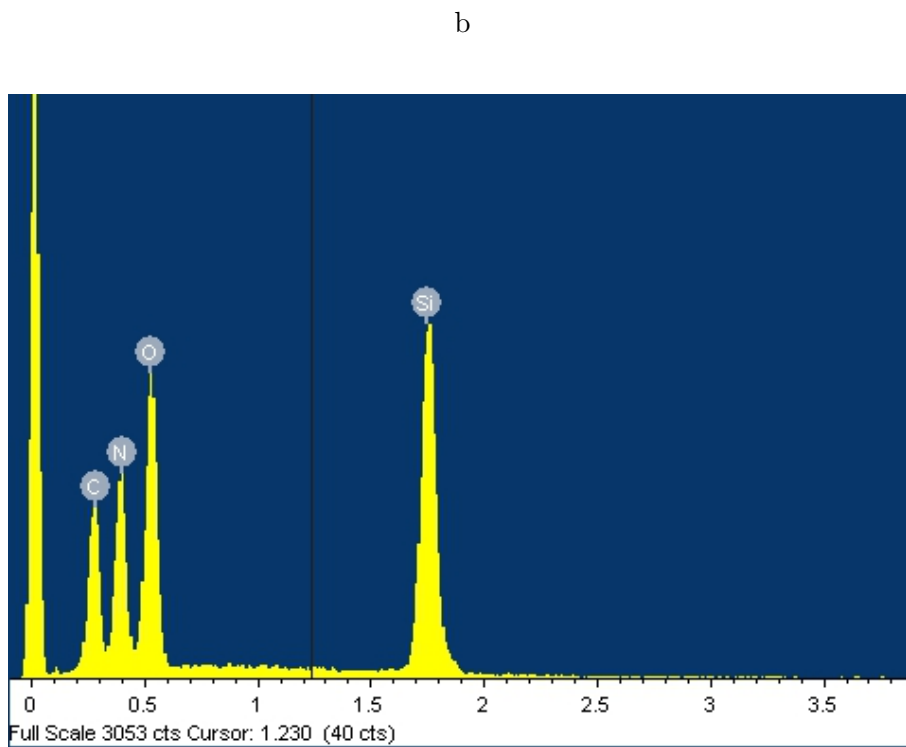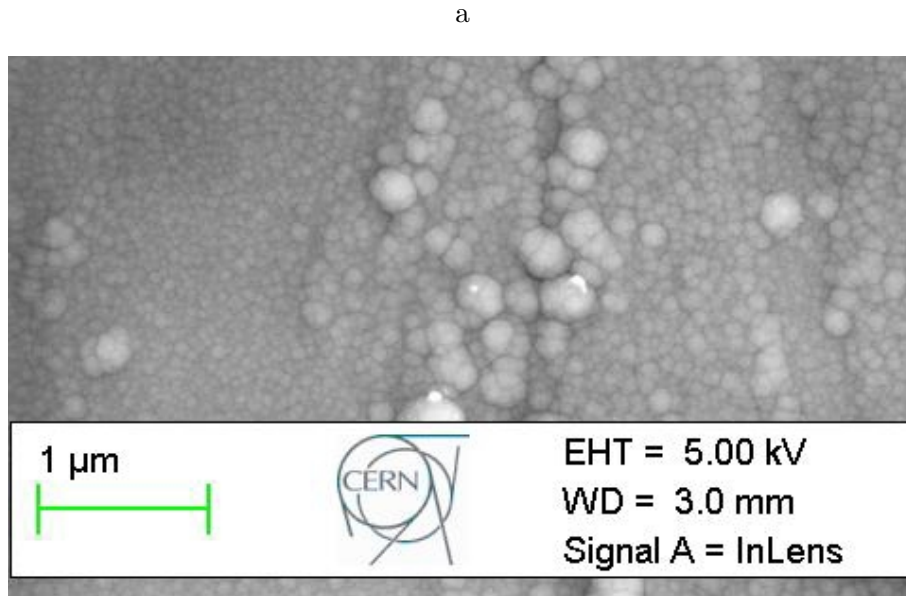
Figure 7.5: The SEM picture of a bad silicon nitride deposition area is shown in (a) and the according energy-dispersive X-ray spectrum (EDX) of it in (b). It can be seen that the surface structure is granular and is building big artefacts where an ideal deposition should be much more flat. The EDX shows, that the surface composition (investigated with a 5keV electron acceleration voltage) is containing a large fraction of oxygen and carbon which usually should not be there.

7.2 Light Yield Measurements

For the light yield measurement we measured the light output of the different samples with a XP2262 PMT [90] using a Cs137 source which produces 662keV gamma rays for excitation. A mask was prepared such that only the light coming from the PhC area was taken into account for the measurements. The whole setup was temperature stabilized at 20 degrees Celsius. Figure 7.6 shows the schematics of the setup. Six different PhC structures were prepared on top of the LSO crystal (see Figure 7.1). Pattern No.1 and No.5 did not survive the cutting and polishing process, which left us four different PhC structured scintillators with the dimensions of $1.2 \times 2.6 \times 5mm^3$. In addition, a reference crystal was cut from the same base crystal, which has been treated the same way then the PhC samples just without a pattern (including the ITO and silicon nitride layer, see area No.7 in Figure 7.1). After cutting they have been polished on all side walls. The crystals were measured with and without optical glue and with and without Teflon wrapping. In Table 7.3 the light yield and the light yield gain relative to the a reference crystal is shown. In addition the samples have been measured with optical glue, with Teflon wrapping and with glue and Teflon wrapping. The relative light yield gain which has been calculated as the ratio between the light yield of the PhC samples and the unstructured reference crystal can be seen in Table 7.5.
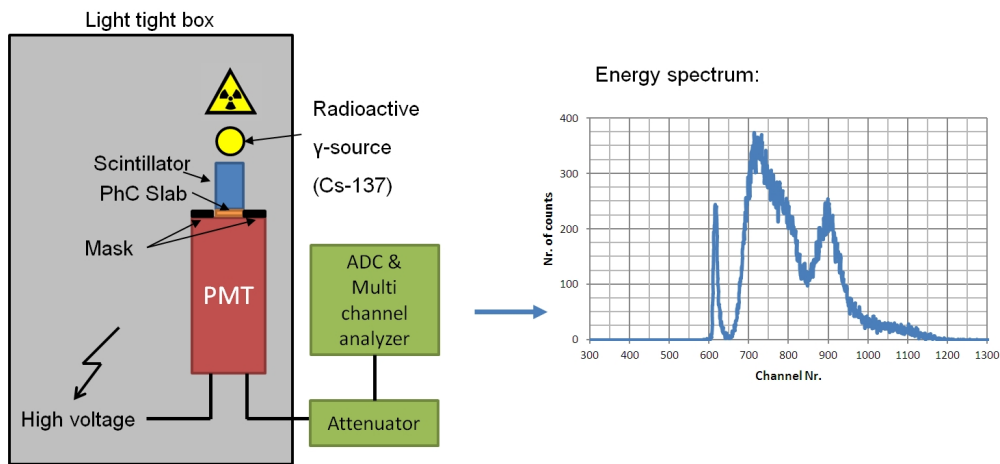
Figure 7.6: Light yield measurement setup. The light yield of the samples was measured using photons of 662keV coming from a Cs137 source. The crystals are placed on top of a XP2262 photomultiplier tube (PMT) with and without optical glue and wrapping. The PMT window has been masked to measure only the light coming from the PhC surface of the scintillator.

Table 7.3: Mean values of the light yield $[Pht/MeV]$ of the different PhC samples measured without wrapping and without optical glue. The gain is calculated as a ratio between the light yield of the PhC crystal and the reference crystal **p7-ref**. The measurement uncertainty in the setup was specified as $\pm 7\%$ and the standard deviation of the measurments is below that uncertainty.

	p7-ref	p2	p3	p4	p6
LY $[Pht/MeV]$	2168	2279	2841	2815	3383
Gain	1.00	1.05	1.31	1.30	1.56

7.2.1   Influence of the Wrapping and Optical Glue

The application of a diffusive wrapping on the sidewalls of the scintillator or an optical contact agent between the scintillator and the photo multiplier tube (PMT) changes the characteristics of the sample significantly. For our measurements Tyvek and Teflon has been used to wrap the scintillating crystals. Tyvek [117] is a sheet of flash-spun high density polyethylene fibres, a product of DuPont. Due to its diffusive light reflection properties it is favourable as a wrapping material for scintillators [118] [119]. Teflon [120], which is also a trade mark of DuPont and has similar light reflection characteristics, has been used for comparison. As an optical contact agent, RHODORSIL Paste 7 [121] has been used. The main idea behind the usage of diffuse wrapping is the improvement of the light output of the scintillator. As discussed in the introduction of this work a lot of the light which is produced in a heavy inorganic scintillator is traveling within the total internal reflection angles and cannot escape the crystal. Diffusive wrapping has different effects on the light propagation of a scintillator and is usually increasing the light output of a scintillator. The majority of these effects can be explained by the diffusion (random scattering) of light which travels within total reflection angles. The aim of the optical glue is to enlarge the light extraction cone (or decrease the number of reflected photons) of the scintillator towards the detector by avoiding the air gap. Basically, the higher the index of refraction (IR) of the optical glue, the more photons can be extracted. But this assumption only holds until the IR of the optical glue becomes as large as the IR of the PMT window. When the IR of the glue becomes larger, you lose the same amount of photons by TIR at the PMT-Glue interface which would have been gained at the crystal-glue interface. The glue used in our work is a oil based silicone paste together with inert fillers and has an index of refraction of 1.41 at the emission wavelength of our LSO scintillator. In table 7.4 the influence of these two different wrappings, with and without optical contact can be seen. While the unwrapped crystal without glue has an light yield of 2168$[Pht/MeV]$, the

usage of glue increases the light output with more than a factor of four. The application of Tyvek or Teflon wrapping improves the light output by a factor of 2.3 for both materials when using dry (no glue) contact. When using glue in addition, we gain a factor of almost 7 compared to the worst configuration. When applying wrapping and glue to our PhC covered sample, the characteristic of the internal light distribution changes and therefore the performance of the PhC structure.

Table 7.4: The light yield of the reference crystal using Teflon and Tyvek wrapping, with and without glue ($[Pht/MeV]$). All measurements were performed at a controlled temperature of 20 degrees Celsius and the light yield was measured at the $1.2mm \times 2.6mm$ large face which did not have a silicon nitride deposition. A mask was used on the PMT tube to ensure that only the light from the regarding side of the crystal is contributing to the measurement result. The measurement error for these LY measurements is within the range of $\pm 10\%$

Plain	Glue	Teflon/Air	Teflon/Glue	Tyvek/Air	Tyvek/Glue
2168	9616	5002	14781	5558	15313

Table 7.5: Light yield gain relative to the reference crystal of the four different PhC sample crystals. The crystals were measured without wrapping and optical glue, with Optical Glue only, with Teflon wrapping only, and finally with Teflon wrapping and optical Glue. Rhodosil®Paste 7 [121]was used as an optical contact agent.

	p2	p3	p4	p6
Air	1.05	1.31	1.30	1.56
Glue	0.70	0.85	0.74	0.69
Teflon	1.17	1.05	0.94	1.28
Glue + Teflon	0.96	0.93	0.92	0.99

The measurement results of these experiments are summarized in Table 7.5, where the light yield of the unstructured reference crystal is compared to the different PhC samples using optical glue and diffusive wrapping. It can be seen, that the performance of the PhC sample decreases with wrapping and glue compared to the unwrapped and dry contact configuration. The reason for that can be traced to the design of the PhC sample. This means, that the PhC has not been designed to work with glue, since it lowers the contrast of the two different materials in the PhC from 1:1.85 (Air:silicon nitride) to 1.39:1.85 (glue:silicon nitride) which has a major impact on the performance of the PhC.

The diffusive wrapping has a different effect on the extraction performance of the PhC: As shown by the simulations in Chapter 5, the current PhC design is diminishing direct (normal incidence) light extraction but still performs better than the reference since the photons which impinges at large angles are much more populated in the case of un-wrapped crystals. When using diffusive wrapping, the angular distribution changes in a way which is reducing the large angle interferences and increases the normal impinging photons which is not in favour for the current PhC design. This can also be seen in the angular distribution plot in Figure 7.7, where the red solid line shows the distribution of photons when using diffusive wrapping and glue. This plot shows that the diffusion of photons at the side wall by the wrapping is leading to an increase in the amount of photons within the extraction cone and a decrease of photons with large angles. The decreased gain in the Teflon wrapped measurements can now be explained with the change in the angular distribution: In our design the PhC pattern was optimized for large impinging angles and a consequence it performs worse for photons close to normal incidence. Using Teflon in combination with glue even shows a slightly worse performance of the PhC crystals when compared to the un-structured reference crystal (see last row in Table 7.5).
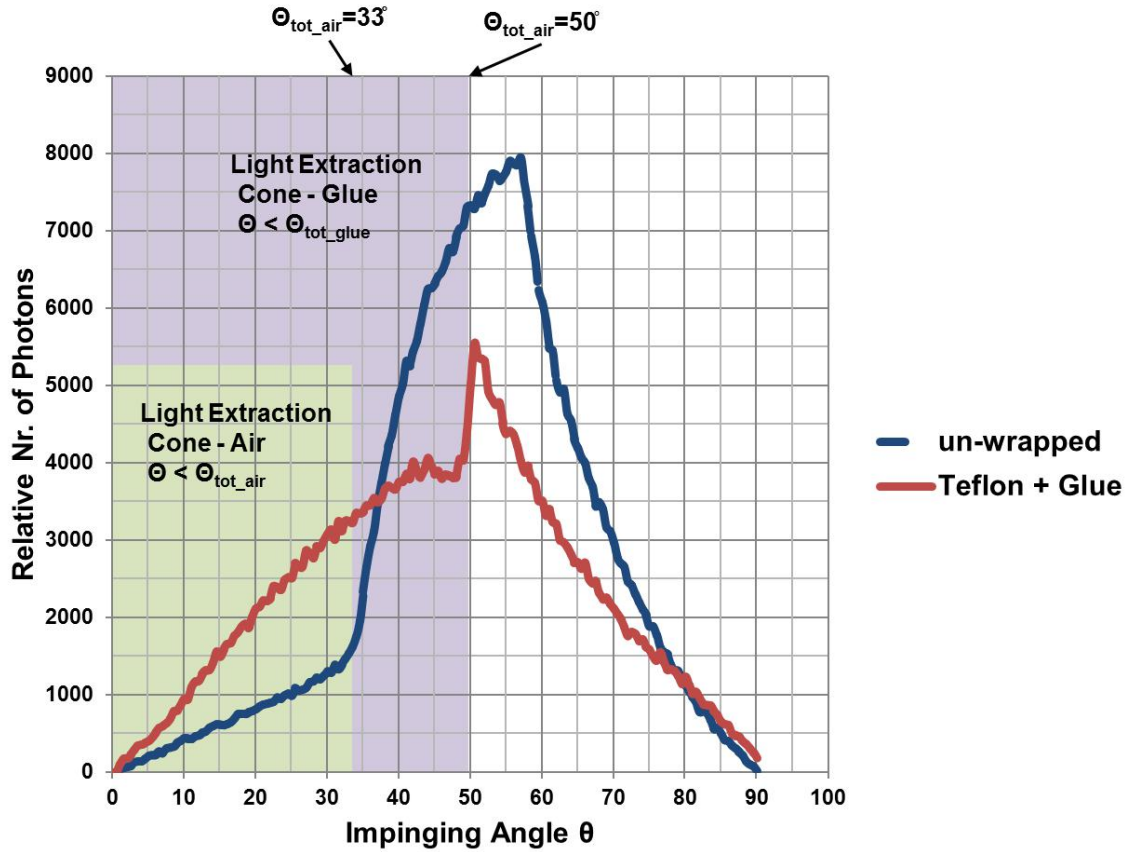
Figure 7.7: Comparison of the simulated angular distribution between an un-wrapped crystal without glue coupling (blue dashed line) and a Teflon wrapped crystal with glue coupling (red solid line). In the case of no wrapping, there are many photons within the angle of $\Theta_{tot} = 33°$ (total reflection angle) and $\Theta_u = 57° = 90 - \Theta_{tot}$ (Θ_u is the upper limit of angles of photons traveling in total reflection modes). Photons which travel within the angular range of Θ_l and Θ_u are called total reflection modes since these photons are reflected within the crystal sidewalls until they get absorbed or diffused. In the case of diffusive wrapping (Teflon), most photons are diffused every time they hit a sidewall. This effect prevents total reflection modes and increases the amount of photons within the photon extraction cone which is $\Theta_{air} = 33°$ for air and $\Theta_{glue} = 50°$ for glue. In this example, 12% of all photons can be extracted in case of no wrapping and no glue and 58% in the case of diffusive wrapping (Teflon) and glue (glue index of refraction=1.42).

7.3   Angular Distribution Measurements

The angular distribution of light coming from a unstructured scintillator is mainly governed by the dimensions of the crystal, index of refraction, the surface polishing grade and the type of wrapping for the lateral faces. If there is a PhC grating at the out-coupling side of the scintillator, the angular distribution changes as well (see Figure 7.9). The light diffraction efficiency is strongly dependent on the light propagation angle, therefore certain angles will be diffracted more strongly than others and this will change the angular distribution. This means that the angular distribution of the light outside the crystal can be used to characterize the PhC efficiency. The angular distribution was measured as illustrated in Figure 7.8. As a light detector a photodiode (Edmund Optics, blue enhanced - G53-378) was used in the first configuration. To get an idea about the spatial light distribution at the crystal surface and to check the photodiode (PD) measurements, a digital single lens reflex camera (DSLR) was used instead the PD in a second setup. As an excitation light source we used UV LEDs or a UV light coming from a $1mm\varnothing$ fibre. While the UV LEDs was used to excite the crystal uniformly over a large volume, the UV fibre was utilized to punctually excite the crystal.

The Setup
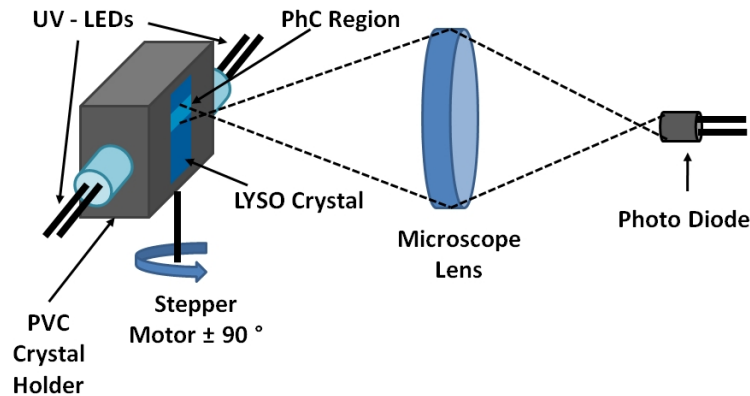
Figure 7.8: Angular distribution measurement setup. The LSO crystal sample is excited by ultraviolet (UV) LEDs or by UV light coming from a $1mm\varnothing$ fiber both having a peak emission wavelength of 365nm. The crystal holder is mounted on top of a computer controlled rotating plate so the surface can be inspected at an angle of ±90 degrees. The crystal can be mounted in horizontal or vertical position. In addition, microscope optics can be used to focus on a certain region of interest.

7.3.1 Measurements using the Photodiode

The setup for the angular distribution measurement using a photodiode consists of a computer controlled rotating table where the crystal can be placed at different angles with respect to the photo-sensor (see Fig. 7.8). To produce enough light for this measurement, the scintillator is excited by two 365nm UV LEDs which leads to strong light emission in the characteristic wavelength of 420nm for LSO and LYSO crystals. The angular distribution has been measured for two different crystal directions, once the crystals x-axis (which defines the short side of the PhC (1.2mm)) was put horizontally on the rotating plate and once the y-axis (which defines the long side of the PhC (2.6mm)). The complete 2π light cone was then inferred from these two measurements. The gain is then calculated as a ratio of the integrated light cone over 2π coming from a PhC scintillator and a reference crystal (see Table 7.6).
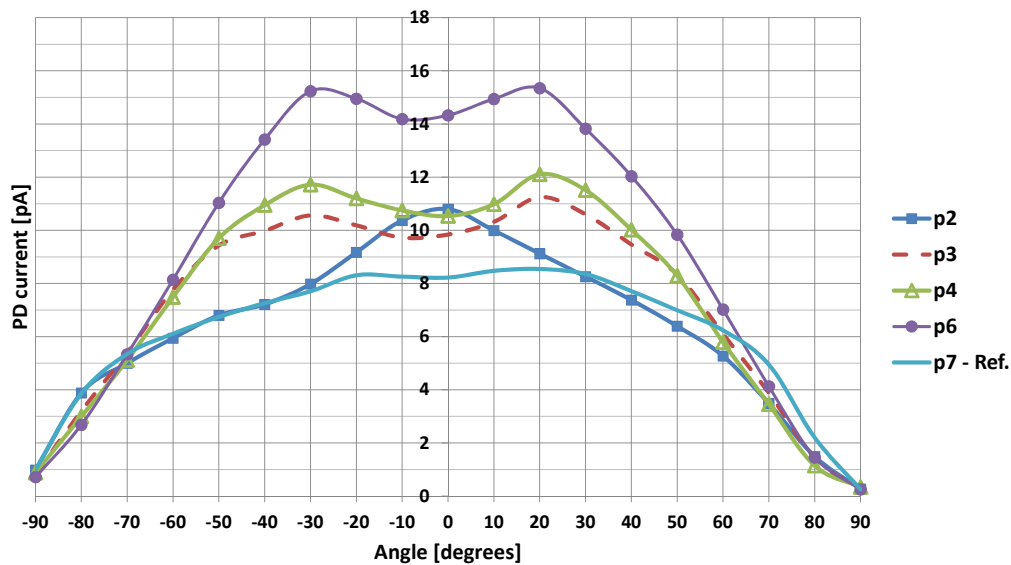
Figure 7.9: Horizontal angular distribution measurements of the four different PhC samples (p2, p3, p4, p6) and the unstructured reference sample (p7). This measurement was performed in the horizontal crystal configuration, which was defined as the crystal position where the x-axis (which defines the short side of the PhC (1.2mm)) is placed horizontally on the measurement bench. Pattern p6, which is the pattern closest to the design, gives the brightest results compared to the reference crystal p7 which is also in best accordance with the light yield simulation results which predicts the same gain.
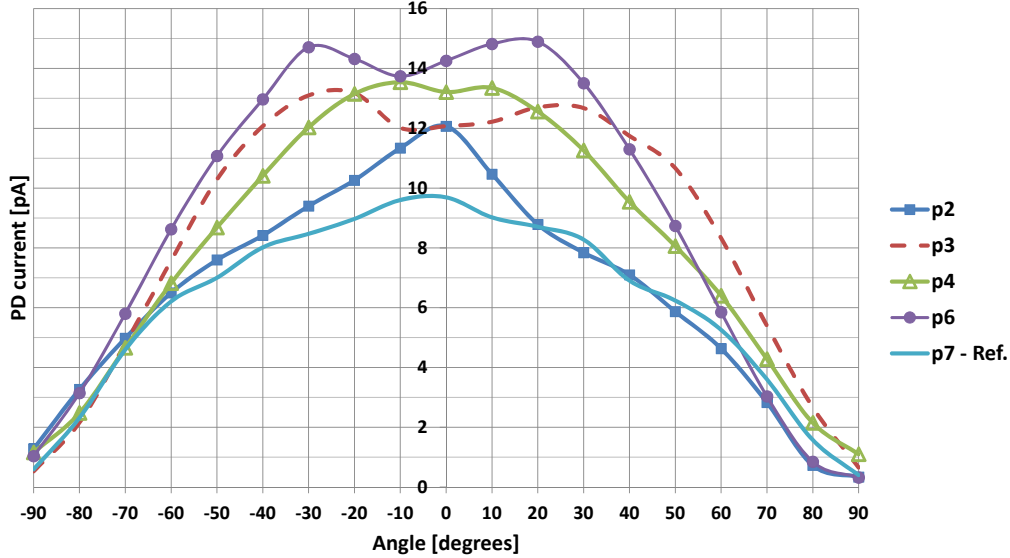
Figure 7.10: Vertical angular distribution measurements of the four different PhC samples (p2, p3, p4, p6) and the unstructured reference sample (p7). The vertical position is defined as the crystal position where the x-axis (which defines the short side of the PhC (1.2mm)) is placed vertically on the measurement bench. It can be seen that the Angular distribution changes for some of the patterns when compared to the horizontal crystal configuration. This can be explained by the fact that the crystal dimensions in x- and y-direction are different at a factor $\geqslant 2$ which leads to this asymmetric behaviour. This difference can also be seen on the unstructured reference sample. p3, p4 and p5 should have the same reflection properties in horizontal and vertical configuration since the PhC patter there is symmetric. Pattern No. 2 (p2) has asymmetric reflection behaviour but since it over all PhC diffraction effect is very low, it cannot be clearly seen in the measurements.

Table 7.6: Light extraction gain of the four different PhC samples compared to the unstructured reference sample. The total light emission for each sample is calculated as the cumulated sum of PD current values from the angular distribution measurements. The measurements were done in a horizontal and in a vertical crystal configuration. To get an approximation of the signal over the whole 2π light cone the average of these two measurements was taken. The values match the light yield gain measured on the LY-bench (see Table 7.5) by $\pm 5\%$.

	p2	p3	p4	p6
Gain Vertical:	1.08	1.30	1.22	1.52
Gain Horizontal:	1.03	1.19	1.24	1.53
Gain Mean:	1.05	1.24	1.23	1.53

To compare the measured angular distribution plots with the ones simulated in Figure 7.7 or Chapter 4 it has to be mentioned that the plots measured with the photodiode are just representing the distribution for one azimuth angle (compare Figure 7.11 and Figure 7.12). If the light emission is assumed to be the same for all azimuth angles the plots can be corrected by the factor $sin(\Theta)$ to get the distribution over the whole 2π light cone.
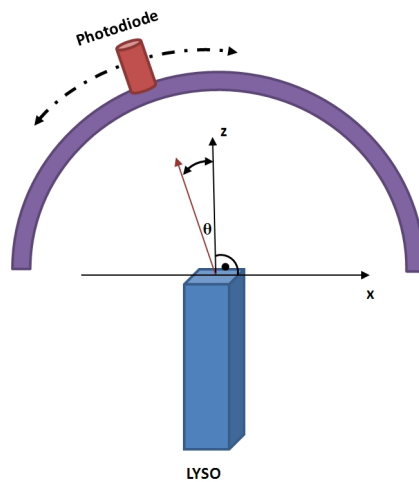
Figure 7.11: Angular distribution measurement with a photodiode. Since just the light along a one dimensional path is recorded, the measurement is just representative for the regarding azimuth angle phi (compare Figure 7.12).
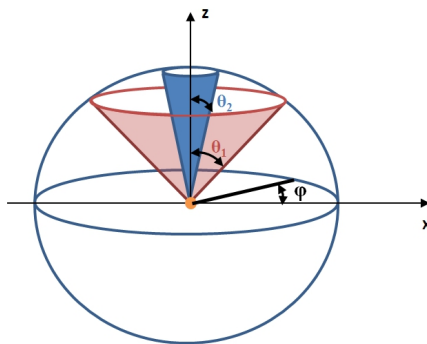
Figure 7.12: Light emission of an isotropic emitter. It shows that light with a bigger angle Θ is more populated since the light cone is infinitesimal small for $\Theta = 0$ and opens up until an angle of $\pi/2$ where it builds a maximum.

7.4   Comparison between Simulation and Measurement Results

In Table 7.7 the simulation and the measurements are compared. The gain is calculated as the ratio between the signals of the PhC enhanced crystal and the un-structured reference crystal. The gain from the angular distribution is calculated from the horizontal and vertical gain measured in Chapter 7.3. For that, the mean of the two measurements were computed as an approximation of the whole 2π light cone. In the Table it can be seen, that the simulated light yield gain is about $10 - 20\%$ higher than the measured results. This is most likely due to the pattern structure imperfections and light absorption by the silicon nitride layer which was not modelled by the simulations. In particular, the square shaped pillar PhC pattern has imperfect edges while the triangular hole pattern shows a certain distortion of the holes which make them slightly elliptic. In addition, the transmission measurements of the silicon nitride layer showed absorption of 15% at a wavelength of 420nm which was also not taken into account for the PhC simulation.

Table 7.7: Comparison between the measured and the simulated light yield in the gamma excitation setup (γ) and in the angular distribution (AD) setup. The four different PhC samples were compared to an unstructured reference sample.

Crystal	Measured gain γ	Measured gain AD	Simulated gain
p2	1.05	1.05	1.32
p3	1.31	1.24	1.41
p4	1.30	1.23	1.47
p6	1.56	1.53	1.69

7.5   Conclusion

This chapter describes the different characterization and performance tests of the current photonic crystal scintillator samples. After the lithography and the cutting and polishing we got four different crystal samples together with one reference sample which was cut from of the same base material for comparison. To check the actual PhC pattern and the differences to the design, a scanning electron beam microscope was used. For the chemical analysis of the PhC material, Energy Dispersive X-ray Spectroscopy (EDS or EDX) was used. It turned out that the samples deviate from the design and the development of

the pattern is of different quality for each crystal. But according to simulations of the corresponding pattern structures, the best sample should still show a 60-70% light yield improvement when compared to the unstructured sample. To check these values, the light yield performance of the PhC scintillator samples were characterized in two different approaches. First, the light output of a $662keV$ gamma ray excitation was measured on a photomultiplier tube. A maximal light yield gain of 56% could be shown between pattern number six (see Figure 7.1) and the reference crystal when using no wrapping. Tyvek® and Teflon® were tested as wrapping material as well but as predicted by the simulations it decreased the PhC gain effect. The explanation for that can be found in taking a closer look to the angles of the photons and the recurrence of them. In the case of no wrapping, more photons are in a total reflection mode and are therefore reflected within the crystal until they get extracted or absorbed. In this configuration, most of the photons are impinging on the extraction surface in a steep angle (larger than the total reflection angle, see the according simulations in Figure 7.7) which makes the photonic crystal grating most efficient. In the case of diffuse lateral wrapping, the angle of the impinging photons are more likely in the light extraction cone already (impinging angle smaller than the total reflection angle) and this makes the PhC grating less effective. Looking to Figure 7.7 we can see that also in the wrapped case there are up to 50% of photons which cannot escape the out-coupling face of the crystal regardless the coupling material (in the case of air there would be light extraction until 33° and in the case of glue until 50°). This shows us that there is still a lot of room for improvement and our simulations showed (see Chapter 9.1), that with an improved PhC structure it should be possible to extract 50% more photons also in the case of diffusive wrapping.

Chapter 8

Summary

Contents

The aim of this work was the design and implementation of a PhC enhanced scintillator sample. The main intention was to overcome the restricted light output of heavy inorganic scintillators which is limited by total internal reflections at the out-coupling face. While the simulations of previous work has shown that this is theoretically possible by the means of photonic crystals [37][80], this work was concentrated on producing and implementing such a structure. For that we improved the PhC simulations as well as the scintillator model itself to better understand the underlying processes which causes the light gain effect. To show the feasibility of producing such a nano scaled grating and to show that the simulated effects can also be measured, a major part of this work was focused on the production of a demonstrator sample. For that we were cooperating with nano lithography specialists from the Nanotechnology Institute of Lyon (INL). As a result of several production trials we have managed to produce six different PhC enhanced lutetium oxyorthosilicate (LSO) scintillator samples. In the characterization process of these samples we could see a clear light yield gain of the PhC samples when compared to an unstructured reference scintillator. In the following three sub-chapters, the main results of this work is summarized which are based on PhC simulations (1), PhC production (2) and the characterization of the PhC enhanced scintillators (3).

8.1   Simulations

8.1.1   Model Fitting

To understand the propagation of light within a scintillator, a good model is required. This is especially of great importance if one wants to study the effects of a PhC grating at the out-coupling side of the scintillator. The CEA (Commissariat à l'énergie atomique et aux énergies alternatives, France) and CERN developed Monte-Carlo program LITRANI [85] was giving us an well-established simulation program to trace the light within a crystal from its birth to the detection or absorption. As we were working on small crystals (e.g. $1.2{\times}2.6{\times}5mm^3$) without wrapping, the former used models [2] were not giving us accurate results. One of the reasons for that was that these models did not take into account the special optical properties of the surface of these models. In unwrapped scintillating crystals, light which is in a reflecting mode bounces within the different surfaces until it gets diffused and extracted or until it gets absorbed. In comparison to big crystals, the light within small crystals has to bounce much more often within the surfaces until it encounters diffusion or absorption. As a result, the surface properties are influencing the light propagation more strongly in small crystals. In our study of the light yield of small un-wrapped LYSO crystals in Chapter 4 the light output of the different sides of the crystal was compared to simulation results. The ratios of the light yield of the different sides could only be reproduced in models where the surface has been given additional diffusion and extraction properties. The different parameters of the bulk material and the surface were optimized to reproduce the measurements of the according configurations. The details on that approach can be seen in Chapter 4. The comparison of the measured and simulated light yield of the final model can be seen in Figure 8.1. The calculated crystal parameters which are giving the best fit for the small scintillator model are shown in Table 8.1. The parameters were successively adjusted until the simulation results were resembling the according measurements shown in Figure 8.1. The two rows with the red background are representing the semi-fixed values of the optimization approach which means that these values are fixed within a small margin which was evaluated by transparency measurements and values taken from actual literature. Therefore the parameter fitting approach was basically optimizing the remaining four parameters which are describing the surface and edge properties of the crystal.
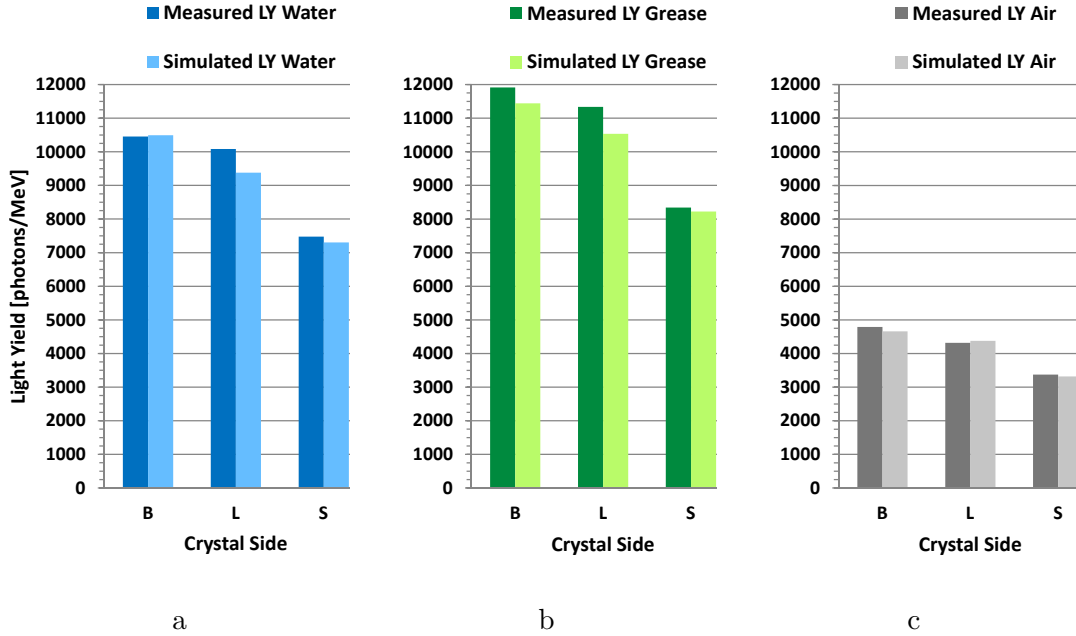
Figure 8.1: Comparison of the light output ($[pht/MeV]$) of the simulations with the light output of the measurements of the different crystal configurations. With the optimized model parameters of the crystal the simulated data fits the measurements by a maximal deviation of 8% and a mean deviation of $\pm 3.2\%$ for all orientations and contact agents.

Table 8.1: Optimized LYSO model parameters of the LITRANI simulations. The diffusion and absorption length of the base material are in the range where other models have predicted them for LYSO [2] [37]. Different surface and edge diffusion was introduced due to a different roughness of these areas. The value of additional diffusion is describing the probability of the diffusion when a photon hits the edge or surface in %. The additional extraction factor describes an additional tendency of the photons getting extracted at the surface which cannot be calculated with diffusion alone. This effect can be explained by Beckmann's and Kirchhof's theory of light scattering on rough surfaces [87] [88].

Parameter	Unit	Value
Substrate Diffusion Length	[cm]	70
Substrate Absorption Length	[cm]	30
Additional Edge Diffusion	[%]	2.0
Additional Surface Diffusion	[%]	0.56
Additional Edge Extraction Factor	[%]	2.7
Additional Surface Extraction Factor	[%]	2.7

8.1.2   Photonic Crystals

The theory of photonic crystals is described in Chapter 3 and the details of our approach including the simulation of it in Chapter 5. Basically, a thin slab of a photonic crystal structure is used to enhance the light extraction of a heavy inorganic scintillator by means of light diffraction. While three dimensional PhC structures would have the most degrees of freedom to control the light propagation and extraction properties, we decided to build a two dimensional structure with finite height, so called two dimensional PhC slabs (2D PhC slab). We have designed and build two different structures to test and compare the feasibility and performance of these PhC structures. While one design is composed of a triangular grid (see Figure 8.2) the other one consists of a square grid of air channels which can also be seen as square pillars of the substrate material (see Figure 8.3).
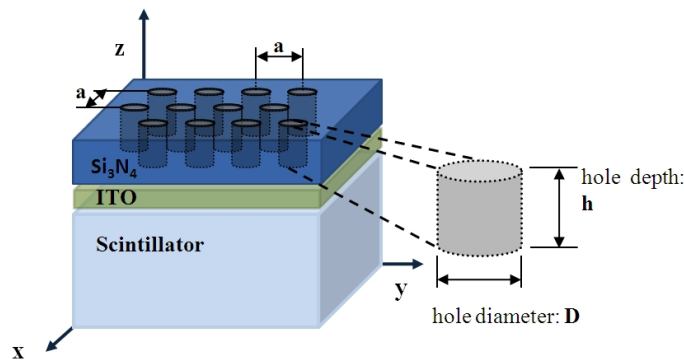
Figure 8.2: PhC structure of triangular placed air holes in a slab of silicon nitride.
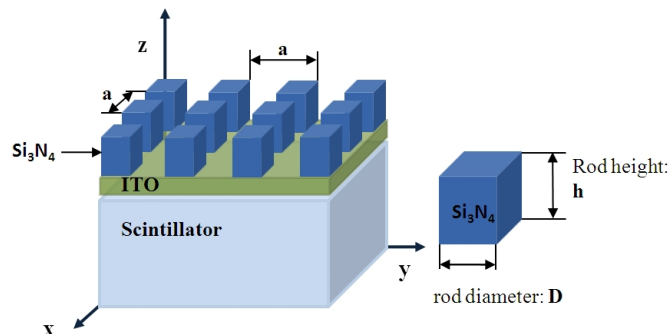
Figure 8.3: PhC structure square pillars of silicon nitride surrounded by air.

Both designs were optimized to give maximal light diffraction for an isotropic light emitter within the substrate. The simulation of the light extraction of pattern No.6 (look for Figure **??** and Table 6.2 in Chapter 6 to see the images and design parameters of the different samples) plotted over the range of impinging photon angles can be seen in Figure 8.4. The figure shows, that the reflection properties of the crystal-air interface are changed completely by the PhC structure. The PhC sample shows more reflection in the case of normal incidence but is able to extract also photons when the angle is larger than the total reflection angle. Since most photons are traveling in the large angle domain (larger than the total reflection angle, in the case of crystal/air it is $\Theta > 33°$) this area has more weight when it comes to light extraction. Therefore, a PhC modified scintillator can emit more light than an unstructured crystal. E.g., in the case of pattern No.6 (which reflectance is shown in Figure 8.4) the simulations predict a light extraction gain of $100 - 120\%$ when applied to an un-wrapped scintillator.

8.1.3   PhC Influence on the Timing

In the chapter of scintillator modeling (Chapter 4) it could be shown that the surface state of the scintillating crystal has a significant influence on the light yield of the regarding detector. Since a PhC changes the reflection and transmission properties of the outcoupling face of a scintillator, it also changes the timing of the extracted photons. By implementing the PhC reflection properties into our Monte Carlo program we could calculate the PhC influence on the photon arrival distribution (see Chapter 5). In this Chapter we could show that photons associated with different modes (nr. of reflections from the lateral faces) are having a different timing component due to their varying path length when they get extracted (modes with more reflections usually travel a longer way and are therefore delayed). These modes have different incident angles and are therefore extracted with a different probability by the PhC. As a result, we can see that the number of very fast photons ($< 50ps$, direct hits - normal incidence, therefore no lateral reflections) is slightly reduced by the PhC while we gain after 50ps (modes which have been reflected several times by the lateral faces with an incidence angle which are in the total reflection regime for unstructured crystals). The timing distribution of these simulations can be seen in Figure 8.5 where the extraction time of photons are compared between a PhC sample and an unstructured reference sample. In Figure 8.6, which shows the integrated time distribution, it can be seen that the extracted number of photons is already larger at 65ps for the PhC sample. Furthermore the simulations showed, that there is still room for
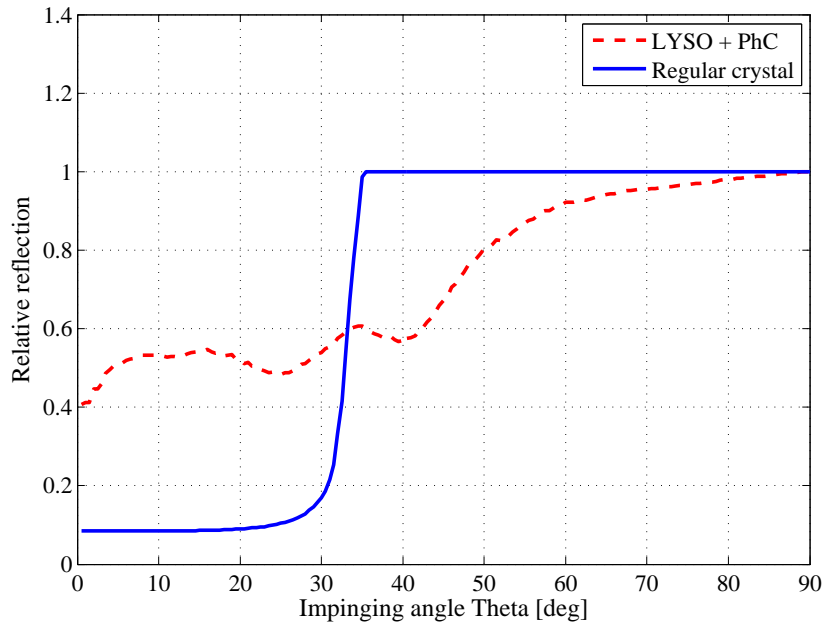
Figure 8.4: Reflection for unpolarized light as a function of the inclination angle Θ for pattern No. 6. Apart from the enhanced transmission for light with $\Theta > 33$ degrees it also shows that the PhC structure reflects a significant amount of light within the range of 0-33 degrees compared to the unstructured sample. But due to the nature of the angular distribution of light impinging on a crystal surface (light wit $\Theta > 33°$ are much more prevalent), the PhC structure still shows a gain over the regular structure.

improvement of the current technique, since for the simulation of the performance shown in Figure 8.5 the actual parameters of the current sample Nr. 6 was used which is not the optimum. The pattern of this sample did not meet the design parameters by 25% divergence. In addition a 20% light absorption of the PhC layer was taken into account for the simulations like measured on our PhC sample reference. If the samples could be produced with a better silicon nitride quality (no absorption) and an more accurate PhC pattern, the performance of the timing could be as shown in Figure 8.7 and 8.8.
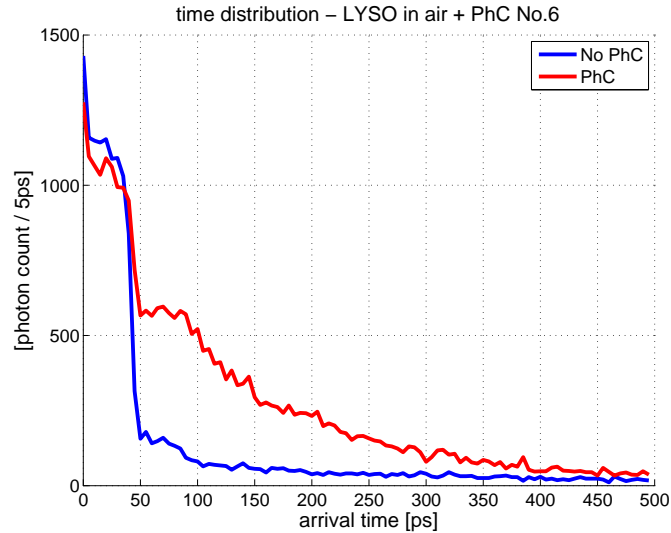
Figure 8.5: Comparison of the time distribution of all extracted photons of the two different configurations (see Figure 5.12 and Figure 5.13). The very fast component ($< 50ps$) is lower at the PhC sample since the PhC surface has lower transmission for light hitting at normal incidence than the unstructured sample (compare Figure 5.9) in Chapter 5.
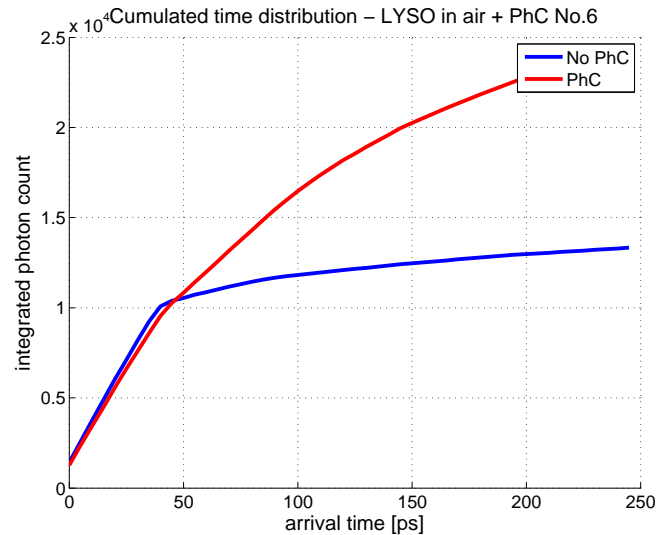
Figure 8.6: Integrated time distribution (from Figure 8.5). It can be seen, that at $\sim$65ps the number of photons are already larger at the PhC sample than at the unstructured sample.
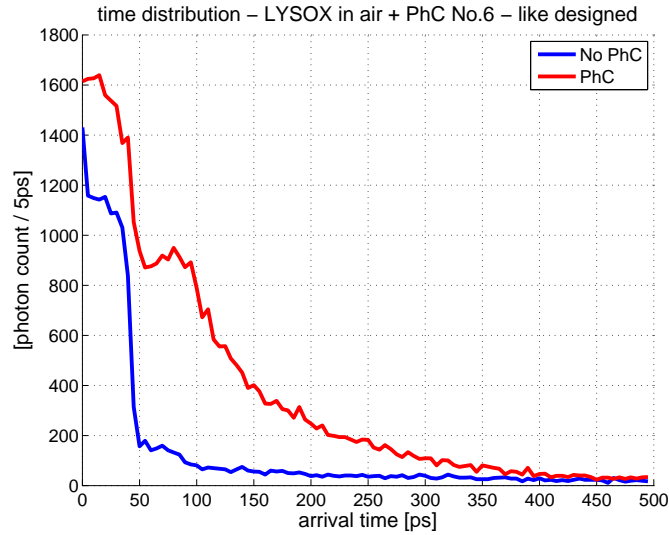
Figure 8.7: Comparison of the time distribution of all extracted photons of the of the reference crystal with PhC No.6 having the exact pattern of the original design (while the real pattern parameters deviates from that by 25% over exposure and a 20% absorption of the silicon nitride.)
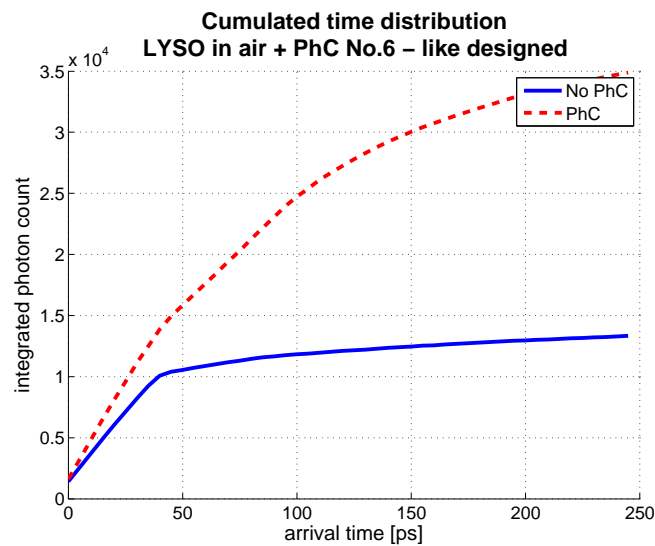
Figure 8.8: Cumulated time distribution of the reference crystal and PhC sample No.6 when having the exact pattern of the original design (compare Figure 8.7). The PhC pattern gives already 50% more photons at an arrival time of 50ps. The overall light yield gain can also be estimated as a factor of 2.1 from this plot when comparing the number of photons at 250ps.

8.2   Experimental Results

8.2.1   Photonic Crystal Fabrication

In Chapter 6, the production of a PhC slab on top of a scintillator is described. The main difficulty of the nano lithography approach was the unusual dimension and the unusual material of our substrate material which was a 5mm high LSO scintillator. The standard nano lithography approach is optimized for thin plates of semiconductors (usually silicon wafers with several inches in diameter and a thickness in the sub-millimetre range). The change from the flat semiconductor material to the scintillator sample introduced a number of problems in the whole process. The details of the different steps and the adaptation we had to make to the standard process can be seen in Chapter 6. One of the two main problems where the spinning of the resist on small crystal samples which resulted in the use of a bigger crystal ($10 \times 10mm^2$ surface area) where small samples were cut out after the whole lithography process. Another problem was the surface charging effects in the electron beam lithography step due to the electrical insulating properties of the scintillator which is interfering with the electrostatic beam deflection of the system. This could be solved by introducing a Indium Tin Oxide (ITO) layer between the silicon nitride and the scintillator which drains the charges when connected to the ground. The silicon nitride (Si_3N_4) layer was used as a transfer material for the PhC pattern which cannot be etched into the scintillator material itself. The ITO as well as the the Si_3N_4 are both optically transparent and have an index of refraction of 1.85 at $420nm$ and are therefore favourable for the PhC. The schematics of the layered structure can be seen in Figure 8.3. As a test, three different PhC layouts and several different lithography parameters were tested on six different samples with an area of $1.2 \times 2.6mm^2$ each. A scanning electron microscope (SEM) image of the six different patterns can be seen in Table 8.2. The patterns are suffering from over or under-exposure but on two samples the design parameters are fitting with a tolerable deviation of about 20%. After the lithography, the six different samples were cut out of the main LSO crystal (dimensions: $5 \times 10 \times 10mm^3$ which was resulting in $1.2 \times 2.6 \times 5mm^3$ large PhC covered scintillator samples. After the cutting, the side walls were polished again. During the cutting and polishing process, pattern No.1 and pattern No.5 were broken which left us the remaining four patterns No.2, No.3, No.4, and No.6.

Table 8.2: Scanning electron microscopy (SEM) images of the six different PhC structures made on top of a LSO sample. The pictures are made with a 40.000× fold magnification using the in-lens camera of a Zeiss SEM.

p1

p2

p3

p4

p5

p6
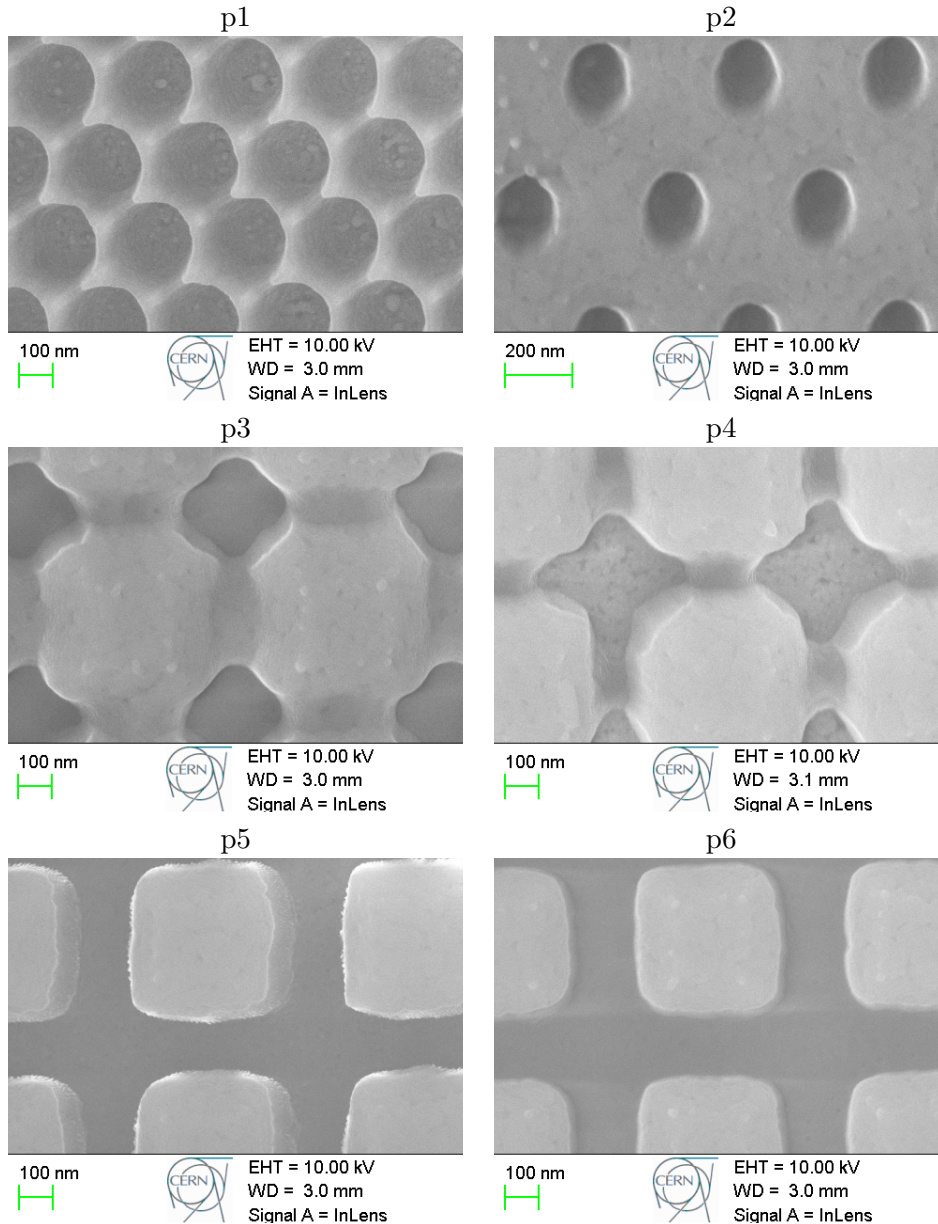
8.2.2 Measurements

For the measurements we followed two different approaches. In the first case the light yield has been measured on a photomultiplier tube (PMT) when exciting the crystals with a $Cs - 137$ gamma source. In the second measurement we recorded the angular light distribution of the emitted light of the PhC surface when the crystal is excited by UV light. The details about the measurements and the setup are explained in the characterization Chapter of this work (7). The summary of the results of the two different approaches can be seen in Figure 8.9. The deviation of the gain between the angular distribution measurement and the light yield measurement, which should be the same, is within the area of ($\pm 10\%$) which is a good agreement.
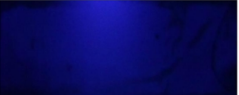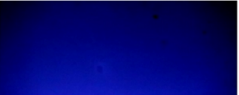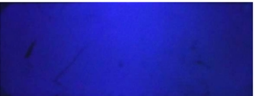
	Picture of the out coupling surface when exiting the crystal with UV light (1.2mm x 2.6mm)	Absolute Light Yield Gain compared to the reference crystal:	Integral of the Angular Distribution Measurement
Reference Crystal #7		1	1
PhC pattern #2:		1.15	0.98
PhC pattern #3:		1.39	1.21
PhC pattern #4:		1.32	1.27
PhC pattern #6:		1.56	1.57

Figure 8.9: Light yield and angular distribution signal gain compared to the unstructured reference crystal in air surrounding. In the left column an image of the PhC region is shown as the scintillator is excited with a 365nm UV LED.

8.2.3　Comparison with the Simulations

When comparing the measurements to the simulations, the simulated light yield gain shows a tendency of being $10 - 20\%$ higher than the measured results (see Table 8.3). This can be explained by the pattern structure imperfections and light absorption by the silicon nitride layer which was not modelled by the simulations. In particular, the square shaped pillar PhC pattern has imperfect edges while the triangular hole pattern shows a certain distortion of the holes which make them slightly elliptic. In addition, the transmission measurements of the silicon nitride layer showed a light absorption of 20% at a wavelength of 420nm. When taking these parameters into account, the simulations are representing a very good fit to the measurements of the regarding samples. But it hast to be mentioned that we do not know the exact reason for this error and there could be other reasons for the deviation between simulation and measurments (e.g. the surface state of the crystal very much influences the internal angular distribution and therefore the PhC perfomance).

Table 8.3: Comparison between the measured and the simulated light yield gain. The four different PHC samples were compared to an unstructured reference sample and the ratio between their light yields is calculated.

Crystal	Measured gain LY	Measured gain AD	Simulated gain
p2	1.05	1.05	1.32
p3	1.31	1.24	1.41
p4	1.30	1.23	1.47
p6	1.56	1.53	1.69

8.3　Conclusion

In the simulation part of our work we could show that we could accurately model a small heavy inorganic scintillator without wrapping. By introducing an additional light-diffusion and extraction caused by surface and edge imperfections, we could reproduce our nine different measurement configurations with an accuracy of $\pm 5\%$. In the second part of the simulations, we were optimizing two different photonic crystal slab structures towards a maximum of light extraction. Additionally, the PhC simulations provided us the reflection and transmission properties of the PhC structure which were then implemented into the Monte Carlo light ray tracing software. The combination of the information from these two programs gave us a complete model of our PhC scintillator samples, which provided

us valuable information when it comes to angular or time distribution information at any position inside or outside of our scintillator sample. In the experimental section, we could show how our PhC scintillators were produced by using an adapted version of electron beam lithography. A $70nm$ layer of Indium tin oxide (ITO) was used for the improvement of the electrical properties and a $400nm$ silicon nitride (Si_3N_4) layer was sputtered as a pattern transfer material. By running several cycles of deposition, resist spinning, electron beam lithography (EBL) and reactive ion etching (RIE) we could adjust the parameters of the process to get a successful lithography result. For this work we produced four different PhC covered LSO scintillators with the dimensions of $1.2 \times 2.6 \times 5mm^3$ where the out-coupling surface of $1.2 \times 2.6mm^2$ was fully covered with a PhC structure. For the characterization of the PhC samples we were having two different measurement setups. First, we were using a $662keV$ gamma excitation to compare the photon light yield of the PhC samples with a un-structured reference sample. And in the second measurement we recorded the angular distribution of light coming from the PhC side of the scintillator when exciting the crystal with UV light. Both characterization methods were showing a clear light extraction improvement of the PhC samples over an unstructured reference sample. In the comparison we could see that the measurements were are in close accordance with our simulations (see Figure 8.3). Even though the overall light extraction of our PhC sample is much smaller than the light extracted from a fully Teflon® wrapped and glued reference crystal, our sample proves the working principle of photonic crystals for light diffraction. The results show that we are in control of a lot of parameters of the PhC technique. This allows us to use the current model to investigate other PhC materials, patterns and applications to further optimize the light output of heavy inorganic scintillators.

Chapter 9

Outlook

9.1 Introduction of an improved PhC structure

Our current sample was designed to work best with air as a filling material for the holes or gaps of the PhC and with the rest of the crystal surrounded by air (no wrapping). The reason for that is that the PhC structure has the largest index of refraction contrast when the holes of the structure are filled with air instead of an optical glue material. Also by not wrapping the crystal, the number of photons which are traveling in total reflection mode are maximized, which is the angular range where the PhC works best. In this configuration, the maximal light diffraction effect with the current design was calculated as 120% compared to the unstructured crystal (see Figure5.5). Therefore it still cannot reach the light output of a scintillator using grease and diffusive wrapping. Our simulation also shows that the optimum for this type of PhC structure is reached when using silicon nitride as a pattern material. To go beyond the performance one can get with glue and diffusive wrapping, the index of refraction of the PhC material has to be increased. Titanium Oxide (TiO_2) and Gallium Nitride (GaN) would be a candidate for such a sample. With those materials one could reach an index of refraction up to 2.5 for TiO_2 and 2.4 with GaN. The simulation results of the reflection and light extraction simulations of an optimized PhC with an index of refraction of 2.4 can be seen in Figure 9.1 and 9.2 respectively. This means, that a PhC material with high index of refraction can provide better light extraction properties. In the search for such a material the feasibility of depositing it on a scintillator has to be kept in mind. Part of the future work will be therefore to investigate new materials for the PhC grating with high index of refraction and the according redesign of the PhC pattern.
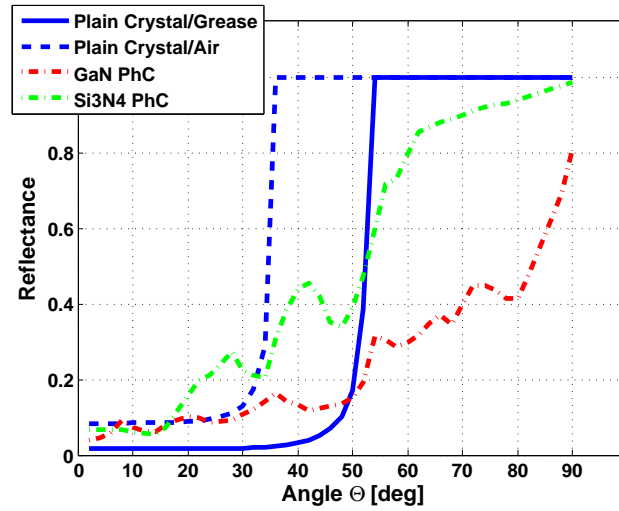
Figure 9.1: Simulation of the reflectance as a function of the angle Θ (impinging, from the crystal to the ambient). The reflections along the whole angular range is significantly reduced for the gallium nitride (GaN) PhC slab compared to the unstructured (plain crystal with grease or air on the outside) or silicon nitride (Si_3N_4) PhC samples.
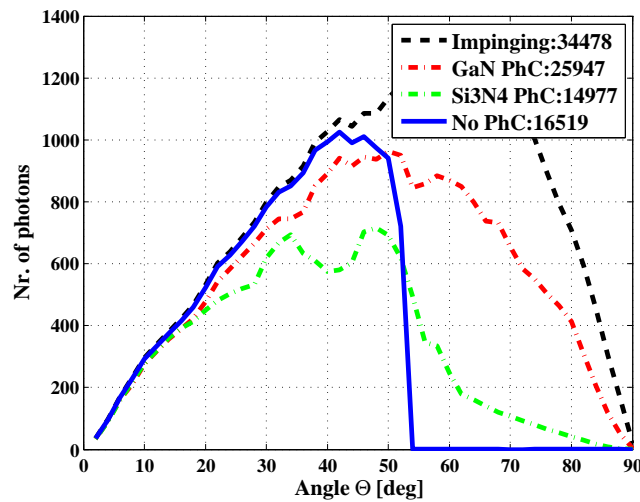
Figure 9.2: The extraction capabilities of a GaN PhC structure with the reflectance shown in Figure 9.1 when applied to a LYSO/LSO crystal with high aspect ratio and highly reflective wrapping. With the PhC grating about 75% of the impinging photons can be extracted to the ambient which is 50% more than achieved with the standard configuration using grease and Teflon (blue solid line). It can be seen that the Si_3N_4 structure cannot compete with the performance of an unstructured crystal with diffusive wrapping and grease coupling.

9.2 Improved PhC production techniques

Electron beam lithography (EBL) is the preferred lithography technique when it comes to prototyping. It is a cheap technique and provides flexibility in the pattern design. The disadvantage is the limited throughput. Due to the scanning nature of the technique, the overall size of the sample is limited by the lithography time. For our sample the EBL took $30 min./mm^2$ and we already tried to speed up the process by using very high dose factors and small beam settling times which has the downside of decreasing the pattern quality. Also just one sample per run can be treated. If one looks now for possibilities of a large area and high throughput production, one has to look out for different lithography techniques. In industry, there are two different ways to cope with that problem; they are called optical interference lithography and nano imprint lithography:

Optical Interference Lithography

Optical Interference Lithography (IL) is a holographic approach where two or more coherent beams interfere to produce a standing wave in the form of the desired pattern [102]. The interference pattern should look like the desired pattern or the negative of it (depends if one uses a positive or negative photo-resist). The exposed areas are the developed and etched like in most other lithography methods. The restriction for that technique is that the pattern has to be periodic in a way that can be reassembled by the superposition of plane waves. The advantage of Optical IL is the large area which can be exposed within a short time.

Nanoimprint Lithography

The nanoimprint lithography (NIL) technique combines the high throughput of an "mask-based" lithography approach with the accuracy and resolution of a low-throughput method like EBL. In the patterning process, a stamp (mold) containing the negative of the desired pattern which was previously manufactured using highly accurate but low throughput approaches is used to mechanically stamp a resist material [103] (see Figure 9.3). The pattern in the resist can then be transferred using standard pattern transfer methods like reactive ion etching (RIE). A nano imprint experiment on scintillating crystals is being prepared with the local company SILSEF and SILTRONIX in cooperation with a CEA - LETI (Laboratoire d'Électronique et de Technologies de l'Information) laboratory in Grenoble. In this experiment, the PhC imprint of several BGO scintillators with a surface
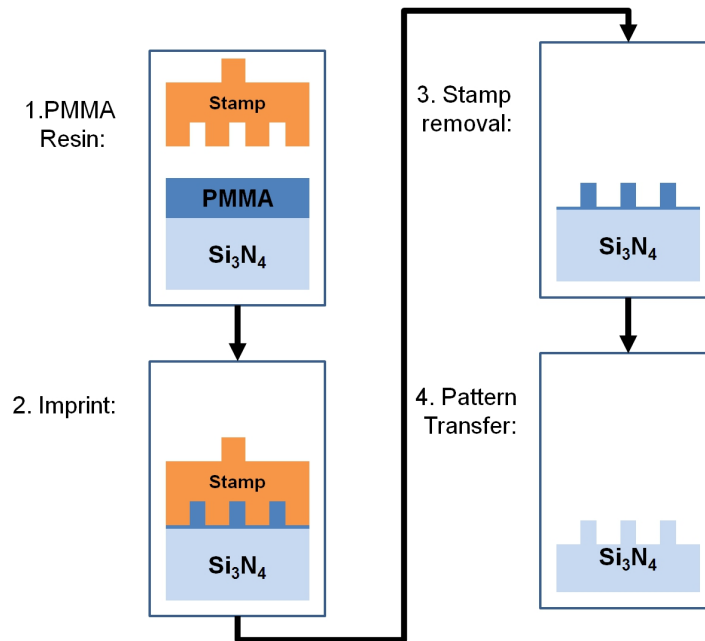
Figure 9.3: The different nano imprint lithography steps. A premanufactured stamp containing the negative of the pattern is imprinted on a PMMA resin which results in the mask for the pattern transfer in the last step.

area of $30mm \times 12mm$ is planned.

9.3 Surface Plasmons

Surface plasmons (SP) are charge-density oscillations at the interface of two media where the real part of the dielectric function is opposite across the interface, e.g. a metal-dielectric interface like a metal sheet in air. They were predicted by Ritchie in 1957 [122] and experimentally evaluated by Powell and Swan in 1959[123] [124]. The excitation of surface plasmons is associated with TM polarized electromagnetic waves at the metal-dielectric interface. The electric field of such a wave would be decaying evanescently into both media which means that it has its maximum at the interface. To couple light to SP a metallic grating which matches the photon and surface plasmon wave vectors can be applied. In the area of light emitting diodes, SP has been used to enhance the light extraction efficiencies of semiconducting or organic materials [125] [126]. Similar to this technique, thin metallic gratings at the outcoupling surface of a scintillating crystal could enhance the light extraction efficiency by coupling total reflection modes to surface

plasmon modes. Another approach would be the surface plasmon assisted light guiding, where SP gratings at an interface are used to couple light and guide it along the metallic grating in a controlled way [127][128] (see Figure **??**).
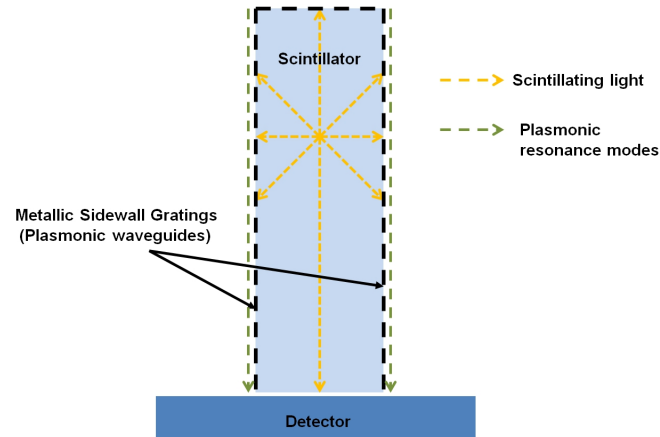
Figure 9.4: Scintillation light guiding at the sidewalls through plasmon resonance modes in metallic gratings.

This could be exploited by applying such metallic gratings at the sidewalls of a scintillator instead of a reflector. In the right configuration, this could have the effect of directly guiding the light towards a detector and therefore detecting light faster by avoiding multiple reflections inside the crystal.

List of Figures

List of Tables

Appendix A

Acronyms

List of Acronyms

BGO	bismuth germinate
BZ	brillouin zone
CAMFR	cavity modeling framework
CCD	charge coupled devise
CDF	cumulative distribution function
CT	computer thomography
dof	degrees of freedom
DUV	deep ultra violet
EBL	electron beam lithography
EM	electro magnetic
ESEM	environmental scanning electron microscopy
eV	electron volt
FFT	fast Fourier transform
FM	fluorescence microscopy
HEP	high energy physic
HIS	heavy inorganic scintillator
IIR	infinite impulse response
ITO	indium tin oxide
LASER	light amplification by stimulated emission of radiation
LED	light emitting diode
LND	linear normal distribution

LITRANI	light transmission in anisotropic media - simulation software
LSM	laser scanning microscopy
LSO	cerium-doped lutetium oxyorthosilicate
LTI	linear time invariant
LY	light yield
LYSO	cerium-doped lutetium yttrium orthosilicate
MPB	MIT Photonic Bands
MeV	mega electron volt
MMA	polymethyl-methacrylat
MRI	magnetic resonance imaging
NA	numerical aperture
NIL	nano imprint lithography
PDE	partial differential equation
PDF	probability density function
PhC	photonic crystal
PCS	photonic crystal slab
PDMS	polydimethylsiloxane
PLM	polarized light microscopy
PMMA	poly(methyl methacrylate)
RIE	reactive ion etching
RL	reciprocal lattice
ROI	region of interest
RV	random variable
SEM	scanning electron microscopy
sccm	standard cubic centimeters per minute
Si_3N_4	silicon nitride
SiO	silicon oxide
SiON	silicon oxi nitrate
TE	transverse electric (s-polarized)
TEM	transmission electron microscopy
TM	transverse magnetic (p-polarized)
TLM	transmitted light microscopy
UV	ultra violet
Z	atomic number

Bibliography

[1] M. Kronberger, E. Auffray, and P. Lecoq, "Improving light extraction from heavy inorganic scintillators by photonic crystals," in *Nuclear Science Symposium Conference Record, 2008. NSS '08. IEEE*, oct. 2008, pp. 3914 –3919.

[2] ——, "Determination of the absolute light yields of luyap and lyso," in *Nuclear Science Symposium Conference Record, 2008. NSS '08. IEEE*, oct. 2008, pp. 1153 –1157.

[3] S. Scheu, H. Kaspar, P. Robmann, A. van der Schaaf, and P. Truoel, "Studies on wrapping materials and light collection geometries in plastic scintillators," *Nuclear Instruments and Methods in Physics Research Section A: Accelerators, Spectrometers, Detectors and Associated Equipment*, vol. 567, no. 1, pp. 345 – 349, 2006, proceedings of the 4th International Conference on New Developments in Photodetection, Fourth International Conference on New Developments in Photodetection. [Online]. Available: http://www.sciencedirect.com/science/article/pii/S0168900206009879

[4] U. Heinrichs, A. Blume, N. Buamann, R. Engels, G. Kemmerling, S. Weber, and K. Ziemons, "Statistical studies on the light output and energy resolution of small lso single crystals with different surface treatments combined with various reflector materials," *Nuclear Instruments and Methods in Physics Research Section A: Accelerators, Spectrometers, Detectors and Associated Equipment*, vol. 486, no. 1-2, pp. 60 – 66, 2002, ¡ce:title¿Proceedings of the 6th International Conference on Inorganic Scin tillators and their Use in Scientific and Industrial Applications¡/ce:title¿. [Online]. Available: http://www.sciencedirect.com/science/article/pii/S0168900202006757

[5] T. Ochiai and K. Sakoda, "Dispersion relation and optical transmittance of a hexagonal photonic crystal slab," *Phys. Rev. B*, vol. 63, p. 125107, Mar 2001. [Online]. Available: http://link.aps.org/doi/10.1103/PhysRevB.63.125107

[6] J. Shakya, K. H. Kim, J. Y. Lin, and H. X. Jiang, "Enhanced light extraction in iii-nitride ultraviolet photonic crystal light-emitting diodes," *Applied Physics Letters*, vol. 85, no. 1, pp. 142–144, 2004. [Online]. Available: http://dx.doi.org/10.1063/1.1768297

[7] S. Fan, P. R. Villeneuve, J. D. Joannopoulos, and E. F. Schubert, "High extraction efficiency of spontaneous emission from slabs of photonic crystals," *Physical Review Letters*, vol. 78, pp. 3294–3297, April 1997. [Online]. Available: http://link.aps.org/abstract/PRL/v78/p3294

[8] E. Matioli and C. Weisbuch, "Impact of photonic crystals on led light extraction efficiency: approaches and limits to vertical structure designs," *Journal of Physics D: Applied Physics*, vol. 43, no. 35, p. 354005, 2010. [Online]. Available: http://stacks.iop.org/0022-3727/43/i=35/a=354005

[9] C. Wiesmann, K. Bergenek, N. Linder, and U. Schwarz, "Photonic crystal leds - designing light extraction," *Laser & Photonics Reviews*, vol. 3, no. 3, pp. 262–286, 2009. [Online]. Available: http://dx.doi.org/10.1002/lpor.200810053

[10] E. M. Purcell, "Spontaneous emission probabilities at radio frequencies," *Physical Review Letters*, vol. 69, pp. 681+, 1946. [Online]. Available: http://prola.aps.org/pdf/PR/v69/i11-12/p674_2

[11] C. M. S. V. S. A. Femius Koenderink, Maria Kafesaki, "Spontaneous emission rates of dipoles in photonic crystal membranes," *J. Opt. Soc. Am. B/Vol. 23, No. 6/June 2006*, vol. 23, pp. 1196–1206, 2006.

[12] J. J. Wierer, A. David, and M. M. Megens, "III-nitride photonic-crystal light-emitting diodes with high extraction efficiency," *Nature Photonics*, vol. 3, no. 3, pp. 163–169, Feb. 2009. [Online]. Available: http://dx.doi.org/10.1038/nphoton.2009.21

[13] A. Knapitsch, E. Auffray, C. W. Fabjan, J.-L. Leclercq, P. Lecoq, X. Letartre, and C. Seassal, "Photonic crystals: A novel approach to enhance the light output of scintillation based detectors," *Nuclear Instruments and Methods in Physics Research Section A: Accelerators, Spectrometers, Detectors and Associated Equipment*, vol. 628, no. 1, pp. 385–388, 2011. [Online]. Available: http://linkinghub.elsevier.com/retrieve/pii/S0168900210015494

[14] A. A. Erchak, D. J. Ripin, S. Fan, P. Rakich, J. D. Joannopoulos, E. P. Ippen, G. S. Petrich, and L. A. Kolodziejski, "Enhanced coupling to vertical radiation using a two-dimensional photonic crystal in a semiconductor light-emitting diode," *Applied Physics Letters*, vol. 78, no. 5, p. 563, 2001. [Online]. Available: http://link.aip.org/link/APPLAB/v78/i5/p563/s1&Agg=doi

[15] A. Knapitsch, E. Auffray, C. Fabjan, J. Leclercq, X. Letartre, R. Mazurczyk, and P. Lecoq, "Effects of photonic crystals on the light output of heavy inorganic scintillators," in *Nuclear Science Symposium and Medical Imaging Conference (NSS/MIC), 2011 IEEE*, oct. 2011, pp. 994 –1001.

[16] A. Knapitsch, E. Auffray, C. W. Fabjan, J.-L. Leclercq, X. Letartre, R. Mazurczyk, and P. Lecoq, "Results of photonic crystal enhanced light extraction on heavy inorganic scintillators," *Nuclear Science, IEEE Transactions on*, vol. PP, no. 99, p. 1, 2012.

[17] P. Lecoq, E. Auffray, S. Gundacker, H. Hillemanns, P. Jarron, A. Knapitsch, J. Leclercq, X. Letartre, T. Meyer, K. Pauwels, F. Powolny, and C. Seassal, "Progress on photonic crystals," in *Nuclear Science Symposium Conference Record (NSS/MIC), 2010 IEEE*, 30 2010-nov. 6 2010, pp. 1970 –1975.

[18] J. B. Birks, *The Theory and Practice of Scintillation Counting*, ser. International series of monographs on electronics and instrumentation. Oxford: Pergamon, 1964.

[19] J. S. Karp, S. Surti, M. E. Daube-Witherspoon, and G. Muehllehner, "Benefit of time-of-flight in pet: experimental and clinical results." *Journal of nuclear medicine official publication Society of Nuclear Medicine*, vol. 49, no. 3, pp. 462–470, 2008. [Online]. Available: http://www.ncbi.nlm.nih.gov/pubmed/18287269

[20] P. Lecoq, E. Auffray, S. Brunner, H. Hillemanns, P. Jarron, A. Knapitsch, T. Meyer, and F. Powolny, "Factors influencing time resolution of scintillators and ways to improve them," in *Nuclear Science Symposium Conference Record (NSS/MIC), 2009 IEEE*, 24 2009-nov. 1 2009, pp. 1880 –1885.

[21] O. V. Losev, "Luminous carborundum (silicon carbide) detector and detection with crystals." *Telegrafiya i Telefoniya bez Provodov*, vol. 44, pp. 485–494, 1927.

[22] N. J. Holonyak and S. F. Bevacqua, "Coherent (visible) light emission from ga(as1-xpx) junctions." *Appl. Phys. Lett.*, vol. 1, pp. 82–83, 1962.

[23] M. Boroditsky, R. Vrijen, T. Krauss, R. Coccioli, R. Bhat, and E. Yablonovitch, "Spontaneous emission extraction and purcell enhancement from thin-film 2-d photonic crystals," *Lightwave Technology, Journal of*, vol. 17, no. 11, pp. 2096 –2112, nov 1999.

[24] R. K. Lee, Y. Xu, and A. Yariv, "Modified spontaneous emission from a two-dimensional photonic bandgap crystal slab," *J. Opt. Soc. Am. B*, vol. 17, no. 8, pp. 1438–1442, Aug 2000. [Online]. Available: http://josab.osa.org/abstract.cfm?URI=josab-17-8-1438

[25] C.-F. Lai, J.-Y. Chi, H.-C. Kuo, C.-H. Chao, H.-T. Hsueh, J.-F. T. Wang, and W.-Y. Yeh, "Anisotropy of light extraction from gantwo-dimensional photonic crystals," *Opt. Express*, vol. 16, no. 10, pp. 7285–7294, May 2008. [Online]. Available: http://www.opticsexpress.org/abstract.cfm?URI=oe-16-10-7285

[26] C.-H. Chao, C.-F. Lai, H.-C. Kuo, and W.-Y. Yeh, "Directional light extraction from photonic crystal thin-film gan light-emitting diodes," in *Lasers Electro Optics The Pacific Rim Conference on Lasers and Electro-Optics, 2009. CLEO/PACIFIC RIM '09. Conference on*, aug. 2009, pp. 1 –2.

[27] J. J. Wierer, M. R. Krames, J. E. Epler, N. F. Gardner, M. G. Craford, J. R. Wendt, J. A. Simmons, and M. M. Sigalas, "Ingan/gan quantum-well heterostructure light-emitting diodes employing photonic crystal structures," *Applied Physics Letters*, vol. 84, no. 19, pp. 3885 –3887, may 2004.

[28] C.-H. Chao, S. L. Chuang, and T.-L. Wu, "Theoretical demonstration of enhancement of light extraction of flip-chip gan light-emitting diodes with photonic crystals," *Applied Physics Letters*, vol. 89, no. 9, pp. 091 116 –091 116–3, aug 2006.

[29] J. G. Mutitu, S. Shi, C. Chen, T. Creazzo, A. Barnett, C. Honsberg, and D. W. Prather, "Thin film solar cell design based on photonic crystal and diffractive grating structures." *Optics Express*, vol. 16, no. 19, pp. 15 238–48, 2008. [Online]. Available: http://www.ncbi.nlm.nih.gov/pubmed/20389619

[30] A. Chutinan, N. P. Kherani, and S. Zukotynski, "High-efficiency photonic crystal solar cellarchitecture," *Opt. Express*, vol. 17, no. 11, pp. 8871–8878, May 2009. [Online]. Available: http://www.opticsexpress.org/abstract.cfm?URI=oe-17-11-8871

[31] W. Crookes, "Certain properties of the emanations of radium," *In Chemical News 87*, p. 241, 1903.

[32] S. C. Curran and J. D. Craggs, *Counting tubes - theory and applications, [1st ed.]*. Academic Press - New York, 1949.

[33] R. D. Evans, *The atomic nucleus*, ser. International series in pure and applied physics. New York, NY: McGraw-Hill, 1955.

[34] P. A. Rodnyi, *Physical Processes in Inorganic Scintillators*, ser. Laser and Optical Science and Technology Series. Boca Raton, FL: CRC Press, 1997.

[35] P. Lecoq, *Inorganic scintillators for detector systems: physical principles and crystal engineering*, ser. Particle acceleration and detection. Springer, 2006. [Online]. Available: http://books.google.com/books?id=dq3LnegUSWAC

[36] J. A. Mares, M. Nikl, N. Solovieva, C. D'Ambrosio, F. de Notaristefani, K. Blazek, P. Maly, K. Nejezchleb, P. Fabeni, G. P. Pazzi, J. T. M. de Haas, C. W. E. van Eijk, and P. Dorenbos, "Scintillation and spectroscopic properties of ce3+-doped yalo3 and lux(re)1-xalo3(re=y3+ and gd3+) scintillators," *Nuclear Instruments and Methods in Physics Research Section A: Accelerators, Spectrometers, Detectors and Associated Equipment*, vol. 498, no. 1-3, pp. 312 – 327, 2003. [Online]. Available: http://www.sciencedirect.com/science/article/pii/S0168900202019964

[37] M. Kronberger, C. W. Fabjan, and P. Lecoq, "Optimization of the light extraction from heavy inorganic scintillators." Ph.D. dissertation, Vienna, Austria, TU Vienna, Vienna, Austria, 2008, presented on 18 Jun 2008.

[38] D. Wahl, V. Mikhailik, and H. Kraus, "The monte-carlo refractive index matching technique for determining the input parameters for simulation of the light collection in scintillating crystals," *Nuclear Instruments and Methods in Physics Research Section A: Accelerators, Spectrometers, Detectors and Associated Equipment*, vol. 570, no. 3, pp. 529 – 535, 2007. [Online]. Available: http://www.sciencedirect.com/science/article/pii/S0168900206017785

[39] P. Dorenbos, J. de Haas, and C. van Eijk, "Non-proportionality in the scintillation response and the energy resolution obtainable with scintillation crystals," *Nuclear Science, IEEE Transactions on*, vol. 42, no. 6, pp. 2190 –2202, dec 1995.

[40] A. Nassalski, M. Moszynski, A. Syntfeld-Kazuch, T. Swiderski, and T. Szczeniak, "Non-proportionality of organic scintillators and bgo," *Nuclear Science, IEEE Transactions on*, vol. 55, no. 3, pp. 1069 –1072, june 2008.

[41] M. M. M. Balcerzyk and M. Kapusta, "Energy resolution of contemporary scintillators. quest for high resolution, proportional detector," *SCINT99*, 1999.

[42] M. Moszynski, "Energy resolution and non-proportionality of scintillation detectors - new observations," *Radiation Measurements*, vol. 45, no. 3-6, pp. 372 – 376, 2010, proceedings of the 7th European Conference on Luminescent Detectors and Transformers of Ionizing Radiation (LUMDETR 2009). [Online]. Available: http://www.sciencedirect.com/science/article/pii/S1350448709001887

[43] W. Moses, S. Payne, W.-S. Choong, G. Hull, and B. Reutter, "Scintillator non-proportionality: Present understanding and future challenges," *Nuclear Science, IEEE Transactions on*, vol. 55, no. 3, pp. 1049 –1053, june 2008.

[44] M. Moszynski, J. Zalipska, M. Balcerzyk, M. Kapusta, W. Mengesha, and J. D. Valentine, "Intrinsic energy resolution of nai(tl)," *Nucl. Instrum. Methods Phys. Res., A*, vol. 484, no. 1-3, pp. 259–269, 2002.

[45] M. Moszyriski, A. Nassalski, A. Syntfeld-Kazuch, L. Swiderski, and T. Szczesniak, "Energy resolution of scintillation detectors - new observations," *Nuclear Science, IEEE Transactions on*, vol. 55, no. 3, pp. 1062 –1068, june 2008.

[46] M. Balcerzyk, M. Moszynski, M. Kapusta, D. Wolski, J. Pawelke, and C. Melcher, "Yso, lso, gso and lgso. a study of energy resolution and nonproportionality," *Nuclear Science, IEEE Transactions on*, vol. 47, no. 4, pp. 1319 –1323, aug 2000.

[47] E. V. D. van Loef, P. Dorenbos, C. W. E. van Eijk, K. W. Krämer, and H. U. Güdel, "Scintillation properties of labr3:ce3+ crystals: fast, efficient and high-energy-resolution scintillators," *Nuclear Instruments and Methods in Physics Research Section A: Accelerators, Spectrometers, Detectors and Associated Equipment*, vol. 486, no. 1-2, pp. 254 – 258, 2002. [Online]. Available: http://www.sciencedirect.com/science/article/pii/S016890020200712X

[48] W. W. Moses, "Scintillator requirements for medical imaging," *International Conference on Inorganic Scintillators and Their Applications: SCINT99*, 1999.

[49] C. W. E. van Eijk, "Inorganic scintillators in medical imaging detectors," *Nuclear Instruments and Methods in Physics Research Section A: Accelerators, Spectrometers, Detectors and Associated Equipment*, vol. 509, no. 1-3, pp. 17 – 25, 2003, proceedings of the 4th Internatonal Workshop on Radiation Imaging Detectors. [Online]. Available: http://www.sciencedirect.com/science/article/pii/S0168900203015420

[50] P. Lecoq, P. Li, and B. Rostaing, "BGO radiation damage effects: optical absorption, thermoluminescence and thermoconductivity," *Nuclear Instruments and Methods in Physics Research Section A: Accelerators, Spectrometers, Detectors and Associated Equipment*, vol. 300, no. 2, pp. 240 – 258, 1991. [Online]. Available: http://www.sciencedirect.com/science/article/pii/016890029190433Q

[51] A. Annenkov, E. Auffray, A. Borisevich, M. Korzhik, P. Lecoq, and V. Ligun, "Suppression of the radiation damage in lead tungstate scintillation crystal," *Nuclear Instruments and Methods in Physics Research Section A: Accelerators, Spectrometers, Detectors and Associated Equipment*, vol. 426, no. 2-3, pp. 486 – 490, 1999. [Online]. Available: http://www.sciencedirect.com/science/article/pii/S0168900298014478

[52] CMS Collaboration, *The CMS electromagnetic calorimeter project: Technical Design Report*, ser. Technical Design Report CMS. Geneva: CERN, 1997.

[53] A. Breskin and R. Voss, *The CERN Large Hadron Collider: Accelerator and Experiments*. Geneva: CERN, 2009.

[54] P. Lecoq, I. Dafinei, E. Auffray, M. Schneegans, M. V. Korzhik, O. V. Missevitch, V. B. Pavlenko, A. A. Fedorov, A. N. Annenkov, V. L. Kostylev, and V. D. Ligun, "Lead tungstate (PbWO4) scintillators for LHC EM calorimetry," *Nuclear Instruments and Methods in Physics Research Section A: Accelerators, Spectrometers, Detectors and Associated Equipment*, vol. 365, no. 2-3, pp. 291 – 298, 1995. [Online]. Available: http://www.sciencedirect.com/science/article/pii/0168900295005897

[55] S. Baccaro, P. Bohacek, B. Borgia, A. Cecilia, I. Dafinei, M. Diemoz, M. Ishii, O. Jarolimek, M. Kobayashi, M. Martini, M. Montecchi, M. Nikl, K. Nitsch, Y. Usuki, and A. Vedda, "Influence of la3+-doping on radiation hardness and thermoluminescence characteristics of pbwo4," *physica status solidi (a)*, vol. 160, no. 2, pp. R5–R6, 1997. [Online]. Available: http://dx.doi.org/10.1002/1521-396X(199704)160:2⟨R5::AID-PSSA99995⟩3.0.CO;2-L

[56] A. A. Annenkov, M. V. Korzhik, and P. Lecoq, "Lead tungstate scintillation material," *Nuclear Instruments and Methods in Physics Research Section A: Accelerators, Spectrometers, Detectors and Associated Equipment*, vol. 490, no.

1-2, pp. 30 – 50, 2002. [Online]. Available: http://www.sciencedirect.com/science/article/pii/S0168900202009166

[57] E. Auffray, P. Lecoq, M. Korzhik, A. Annenkov, O. Jarolimek, M. Nikl, S. Baccaro, A. Cecilia, M. Diemoz, and I. Dafinei, "Improvement of several properties of lead tungstate crystals with different doping ions," *Nuclear Instruments and Methods in Physics Research Section A: Accelerators, Spectrometers, Detectors and Associated Equipment*, vol. 402, no. 1, pp. 75 – 84, 1998. [Online]. Available: http://www.sciencedirect.com/science/article/pii/S0168900297010887

[58] M. Kobayashi, Y. Usuki, M. Ishii, T. Yazawa, K. Hara, M. Tanaka, M. Nikl, and K. Nitsch, "Improvement in transmittance and decay time of pbwo4 scintillating crystals by la-doping," *Nuclear Instruments and Methods in Physics Research Section A: Accelerators, Spectrometers, Detectors and Associated Equipment*, vol. 399, no. 2-3, pp. 261 – 268, 1997. [Online]. Available: http://www.sciencedirect.com/science/article/pii/S0168900297009297

[59] CMS colaboration, *CMS, the Compact Muon Solenoid : technical proposal*, ser. LHC Tech. Proposal. Geneva: CERN, 1994, cover title : CMS, the Compact Muon Solenoid : technical proposal.

[60] P. Harrison and H. Quinn, *BaBar physics book: physics at an asymetric B factory*, ser. SLAC report. Stanford Linear Acceleration Center, 1998. [Online]. Available: http://books.google.com/books?id=HJ0sAAAAYAAJ

[61] D. e. a. Boutigny, "BaBar technical design report," *SLAC-R-0457*, vol. 1, p. 1, 1995, sLAC-R-0457.

[62] J. M. Bauer, "The babar electromagnetic calorimeter: Status and performance improvements," SLAC, Stanford, CA, Tech. Rep. physics/0601138. BABAR-TALK-2005-145. SLAC-PUB-11578, Jan 2006.

[63] G. N. B. D. da Silva, "Development and implementation of the clearpem-sonic detector control system," Ph.D. dissertation, Universidade Técnica de Lisboa, 2010.

[64] M. Abreu, J. Aguiar, F. Almeida, P. Almeida, P. Bento, B. Carrico, M. Ferreira, N. Ferreira, F. Goncalves, C. Leong, F. Lopes, P. Lousa, M. Martins, N. Matela, P. Mendes, R. Moura, J. Nobre, N. Oliveira, C. Ortigao, L. Peralta, R. Pereira, J. Rego, R. Ribeiro, P. Rodrigues, J. Sampaio, A. Santos, L. Silva, J. Silva, P. Sousa,

I. Teixeira, J. Teixeira, A. Trindade, and J. Varela, "Design and evaluation of the clear-pem scanner for positron emission mammography," *Nuclear Science, IEEE Transactions on*, vol. 53, no. 1, pp. 71 – 77, feb. 2006.

[65] L. Biró, K. Kertész, Z. Vértesy, G. Márk, Z. Bálint, V. Lousse, and J.-P. Vigneron, "Living photonic crystals: Butterfly scales – nanostructure and optical properties," *Materials Science and Engineering: C*, vol. 27, no. 5-8, pp. 941 – 946, 2007, eMRS 2006 Symposium A: Current Trends in Nanoscience - from Materials to Applications. [Online]. Available: http://www.sciencedirect.com/science/article/pii/S0928493106003468

[66] E. Yablonovitch, "Inhibited spontaneous emission in solid-state physics and electronics," *Phys. Rev. Lett.*, vol. 58, no. 20, pp. 2059–2062, May 1987.

[67] S. John, "Strong localization of photons in certain disordered dielectric superlattices," *Phys. Rev. Lett.*, vol. 58, no. 23, pp. 2486–2489, Jun 1987.

[68] Y. Lin, D. Rivera, and K. P. Chen, "Woodpile-type photonic crystals with orthorhombic or tetragonal symmetry formed through phase mask techniques," *Opt. Express*, vol. 14, no. 2, pp. 887–892, Jan 2006. [Online]. Available: http://www.opticsexpress.org/abstract.cfm?URI=oe-14-2-887

[69] J. D. Joannopoulos, "Photonics: Self-assembly lights up," *Nature*, vol. 414, pp. 257–258, November 2001.

[70] J. D. Jackson, *Classical Electrodynamics Third Edition*, 3rd ed. Wiley, Aug. 1998. [Online]. Available: http://www.amazon.com/exec/obidos/redirect?tag=citeulike07-20&path=ASIN/047130932X

[71] K. Busch and S. John, "Liquid-crystal photonic-band-gap materials: The tunable electromagnetic vacuum," *Phys. Rev. Lett.*, vol. 83, pp. 967–970, Aug 1999. [Online]. Available: http://link.aps.org/doi/10.1103/PhysRevLett.83.967

[72] N. Ashcroft and N. Mermin, *Solid state physics*, ser. Holt-Saunders International Editions: Science : Physics. Holt, Rinehart and Winston, 1976. [Online]. Available: http://books.google.ch/books?id=FRZRAAAAMAAJ

[73] K. Sakoda, *Optical Properties Of Photonic Crystals*, ser. Springer Series in Optical Sciences. Springer, 2005. [Online]. Available: http://books.google.ch/books?id=oMIF_NRoV8QC

[74] H. Ibach and H. Lüth, *Solid-state physics: an introduction to principles of materials science*, ser. Advanced texts in physics. Springer, 2003. [Online]. Available: http://books.google.ch/books?id=PIEfweaKyK8C

[75] S. G. Johnson and J. D. Joannopoulos, "Block-iterative frequency-domain methods for maxwell's equations in a planewave basis," *Opt. Express*, vol. 8, no. 3, pp. 173–190, 2001. [Online]. Available: http://www.opticsexpress.org/abstract.cfm?URI=OPEX-8-3-173

[76] S. G. Johnson, S. Fan, P. R. Villeneuve, J. D. Joannopoulos, and L. A. Kolodziejski, "Guided modes in photonic crystal slabs," *Physical Review B*, vol. 60, pp. 5751–5758, 1999.

[77] H. Y. Ryu, Y. H. Lee, R. L. Sellin, and D. Bimberg, "Over 30-fold enhancement of light extraction from free-standing photonic crystal slabs with ingaas quantum dots at low temperature," *Applied Physics Letters*, vol. 79, no. 22, pp. 3573 –3575, nov 2001.

[78] H.-Y. Ryu, J.-K. Hwang, Y.-J. Lee, and Y.-H. Lee, "Enhancement of light extraction from two-dimensional photonic crystal slab structures," *Selected Topics in Quantum Electronics, IEEE Journal of*, vol. 8, no. 2, pp. 231 –237, mar/apr 2002.

[79] R. Hagen, "Spectral investigation of a 2-dimensional photonic crystal slab for mid-infrared radiation," September 2007. [Online]. Available: http://essay.utwente.nl/645/

[80] M. Kronberger, E. Auffray, and P. Lecoq, "Probing the concepts of photonic crystals on scintillating materials," *Nuclear Science, IEEE Transactions on*, vol. 55, no. 3, pp. 1102 –1106, june 2008.

[81] J. D. Joannopoulos, S. G. Johnson, J. N. Winn, and R. D. Meade, *Photonic Crystals: Molding the Flow of Light (Second Edition)*, 2nd ed. Princeton University Press, 2008.

[82] A. David, H. Benisty, and C. Weisbuch, "Optimization of light-diffracting photonic-crystals for high extraction efficiency leds," *Display Technology, Journal of*, vol. 3, no. 2, pp. 133 –148, june 2007.

[83] A. Wirrwar, N. Schramm, H. Vosberg, and H.-W. Muller-Gartner, "Influence of crystal geometry and wall reflectivity on scintillation photon yield and energy resolution," in *Nuclear Science Symposium, 1999. Conference Record. 1999 IEEE*, vol. 3, 1999, pp. 1443 –1445 vol.3.

[84] J. Bea, A. Gadea, L. Garcia-Raffi, J. Rico, B. Rubio, and J. Tain, "Simulation of light collection in scintillators with rough surfaces," *Nuclear Instruments and Methods in Physics Research Section A: Accelerators, Spectrometers, Detectors and Associated Equipment*, vol. 350, no. 1-2, pp. 184 – 191, 1994. [Online]. Available: http://www.sciencedirect.com/science/article/pii/0168900294911622

[85] F. X. Gentit, "SLITRANI simulation framework." [Online]. Available: http://gentitfx.fr/SLitrani/

[86] CERN, "ROOT data analysis framework - CERN." [Online]. Available: http://root.cern.ch/drupal/

[87] P. Beckmann and A. Spizzichino, "The scattering of electromagnetic waves from rough surfaces," *Pergamon Press, New York*, 1963.

[88] J. E. Harvey, A. Krywonos, and C. L. Vernold, "Modified Beckmann-Kirchhoff scattering model for rough surfaces with large incident and scattering angles," *Optical Engineering*, vol. 46, no. 7, p. 078002, 2007. [Online]. Available: http://link.aip.org/link/OPEGAR/v46/i7/p078002/s1&Agg=doi

[89] G. Guohua, K. Songfeng, S. Xiubao, and C. Qian, "Study of photons reflection on rough surface," *Optical and Quantum Electronics*, vol. 41, pp. 453–461, 2009, 10.1007/s11082-010-9378-y. [Online]. Available: http://dx.doi.org/10.1007/s11082-010-9378-y

[90] PHOTONIS, "XP2262 photomultiplier Datasheet." [Online]. Available: http://my.et-enterprises.com/pdf/XP2262.pdf

[91] R. Thompson, J. LeBlanc, and D. McDaniel, "A new monte carlo simulation model for the transport of optical photons over rough surfaces," in *Nuclear Science Symposium Conference Record, 2003 IEEE*, vol. 5, oct. 2003, pp. 3226 – 3229 Vol.5.

[92] T. Tomitani, "A model of optical reflection on rough surface and its application to monte carlo simulation of light transport," *Nuclear Science, IEEE Transactions on*, vol. 43, no. 3, pp. 1544 –1548, jun 1996.

[93] M. Janecek and W. Moses, "Measuring light reflectance of bgo crystal surfaces," *Nuclear Science, IEEE Transactions on*, vol. 55, no. 5, pp. 2443 –2449, oct. 2008.

[94] I. Vilardi, A. Braem, E. Chesi, F. Ciocia, N. Colonna, F. Corsi, F. Cusanno, R. D. Leo, A. Dragone, F. Garibaldi, C. Joram, L. Lagamba, S. Marrone, E. Nappi, J. Seguinot, G. Tagliente, A. Valentini, P. Weilhammer, and H. Zaidi, "Optimization of the effective light attenuation length of yap:ce and lyso:ce crystals for a novel geometrical pet concept," *Nuclear Instruments and Methods in Physics Research Section A: Accelerators, Spectrometers, Detectors and Associated Equipment*, vol. 564, no. 1, pp. 506 – 514, 2006. [Online]. Available: http://www.sciencedirect.com/science/article/pii/S0168900206007820

[95] C. G. Bostan, "Design and fabrication of quasi-2d photonic crystal components based on silicon-on-insulator technology," Ph.D. dissertation, Enschede, 2005. [Online]. Available: http://doc.utwente.nl/50288/

[96] P. Bienstman, "Camfr (cavity modelling framework)." [Online]. Available: http://camfr.sourceforge.net

[97] J.-P. Berenger, "A perfectly matched layer for the absorption of electromagnetic waves," *Journal of Computational Physics*, vol. 114, no. 2, pp. 185 – 200, 1994. [Online]. Available: http://www.sciencedirect.com/science/article/pii/S0021999184711594

[98] M. G. Moharam and T. K. Gaylord, "Rigorous coupled-wave analysis of planar-grating diffraction," *J. Opt. Soc. Am.*, vol. 71, no. 7, pp. 811–818, Jul 1981. [Online]. Available: http://www.opticsinfobase.org/abstract.cfm?URI=josa-71-7-811

[99] NIST, "NIST XCOM: Photon Cross Sections Database."

[100] C. Mack, *Fundamental principles of optical lithography: the science of microfabrication*. Wiley, 2007. [Online]. Available: http://books.google.com/books?id=nHm4e7rFNfgC

[101] H. Levinson, *Principles of lithography*, ser. Press Monographs. SPIE Press, 2005. [Online]. Available: http://books.google.com.pe/books?id=EjMpqEy07bsC

[102] M. Maldovan and E. L. Thomas, *Periodic Materials and Interference Lithography for Photonics, Phononics and Mechanics*. Wiley-VCH; 1 edition (December 16, 2008), 2008.

[103] S. Y. Chou, P. R. Krauss, and P. J. Renstrom, "Nanoimprint lithography," *Journal of Vacuum Science Technology*, vol. 14, no. 6, pp. 4129+, Nov. 1996.

[104] MicroChem Corp, "Process data for PMMA." [Online]. Available: http://www.nano.org.tr/files/e-beam_lithography/Resist_process_data_NANO_PMMA_04_eng.pdf

[105] M. J. B. L. F. Thompson, C. G. Willson, *Introduction to Microlithography - Theory, Materials, and Processing*, L. F. Thompson, Ed. American Chemical Society, Seattle, Washington,, March 20-25, 1983.

[106] MicroChem Corp, "Process data for PMMA Resist." [Online]. Available: http://www.microchem.com/pdf/PMMA_Data_Sheet.pdf

[107] K. Suzuki and B. Smith, *Microlithography: science and technology*, ser. Optical science and engineering. CRC Press, 2007. [Online]. Available: http://books.google.com/books?id=_hTLDCeIYxoC

[108] P. Rai-Choudhury, *Handbook of microlithography, micromachining, and microfabrication*. SPIE press, 1997, vol. 1. [Online]. Available: http://books.google.com/books?id=vcVPfTCcQ04C&pgis=1

[109] D. F. Kyser, "Monte carlo simulation of spatially distributed beams in electron-beam lithography," *Journal of Vacuum Science and Technology, vol. 12, issue 6, p. 1305*, 1975.

[110] MicroChem Corp, "PMMA Developer." [Online]. Available: http://www.microchem.com/pdf/pmma.pdf

[111] E. D. Palik, *Handbook of Optical Constants of Solids (5 Volume Set)*. Academic Press, Jan. 1997. [Online]. Available: http://www.amazon.com/exec/obidos/redirect?tag=citeulike07-20&path=ASIN/012544415X

[112] D. Bartle, D. Andrews, J. Grange, A. Trigg, and D. Wickenden, "An examination of the reactive sputtering of silicon nitride on to gallium arsenide," *Vacuum*, vol. 33, no. 7, pp. 407 – 410, 1983. [Online]. Available: http://www.sciencedirect.com/science/article/pii/0042207X83906607

[113] M. Z. Kana, E. Centurioni, D. Iencinella, and C. Summonte, "Influence of the sputtering system's vacuum level on the properties of indium tin oxide films,"

Thin Solid Films, vol. 500, no. 1-2, pp. 203 – 208, 2006. [Online]. Available: http://www.sciencedirect.com/science/article/pii/S0040609005020432

[114] M. Vila, J. A. Martín-Gago, A. Muñoz-Martín, C. Prieto, P. Miranzo, M. I. Osendi, J. García-López, and M. A. Respaldiza, "Compositional characterization of silicon nitride thin films prepared by rf-sputtering," *Vacuum*, vol. 67, no. 3-4, pp. 513 – 518, 2002. [Online]. Available: http://www.sciencedirect.com/science/article/pii/S0042207X0200221X

[115] SOPRALAB, "Optical n&k database," Jun. 2009. [Online]. Available: http://www.sopra-sa.com/index2.php?goto=dl&rub=4

[116] T. Bååk, "Silicon oxynitride; a material for grin optics," *Appl. Opt.*, vol. 21, no. 6, pp. 1069–1072, Mar 1982. [Online]. Available: http://ao.osa.org/abstract.cfm?URI=ao-21-6-1069

[117] TYVEK, "TYVEK datasheet." [Online]. Available: http://www2.dupont.com/Tyvek/en_US/assets/downloads/tyvek_handbook.pdf

[118] M. Janecek and W. W. Moses, "Simulating Scintillator Light Collection Using Measured Optical Reflectance," *IEEE Transactions on Nuclear Science*, vol. 57, pp. 964–970, Jun. 2010.

[119] R. Mao, L. Zhang, and R.-Y. Zhu, "Optical and scintillation properties of inorganic scintillators in high energy physics," *Nuclear Science, IEEE Transactions on*, vol. 55, no. 4, pp. 2425 –2431, aug. 2008.

[120] TEFLON, "TEFLON datasheet." [Online]. Available: http://www2.dupont.com/Teflon_Industrial/en_US/products/product_by_name/teflon_af/properties.html

[121] www.ellsworth.se, "Rhodorsil paste 7." [Online]. Available: http://www.ellsworth.se/UserFiles/file/DATABLAD/Rhodorsil%207.pdf

[122] R. H. Ritchie, "Plasma losses by fast electrons in thin films," *Phys. Rev.*, vol. 106, pp. 874–881, Jun 1957. [Online]. Available: http://link.aps.org/doi/10.1103/PhysRev.106.874

[123] C. J. Powell and J. B. Swan, "Origin of the characteristic electron energy losses in aluminum," *Phys. Rev.*, vol. 115, pp. 869–875, Aug 1959. [Online]. Available: http://link.aps.org/doi/10.1103/PhysRev.115.869

[124] ——, "Origin of the characteristic electron energy losses in magnesium," *Phys. Rev.*, vol. 116, pp. 81–83, Oct 1959. [Online]. Available: http://link.aps.org/doi/10.1103/PhysRev.116.81

[125] J. Vuckovic, M. Loncar, and A. Scherer, "Surface plasmon enhanced light-emitting diode," *Quantum Electronics, IEEE Journal of*, vol. 36, no. 10, pp. 1131 –1144, oct 2000.

[126] J. Frischeisen, Q. Niu, A. Abdellah, J. B. Kinzel, R. Gehlhaar, G. Scarpa, C. Adachi, P. Lugli, and W. Brütting, "Light extraction from surface plasmons and waveguide modes in an organic light-emitting layer by nanoimprinted gratings," *Optics Express*, vol. 19, p. 7, Jan. 2011.

[127] A. Karalis, E. Lidorikis, M. Ibanescu, J. D. Joannopoulos, and M. Soljačić, "Surface-plasmon-assisted guiding of broadband slow and subwavelength light in air," *Physical Review Letters*, vol. 95, p. 063901, August 2005. [Online]. Available: http://link.aps.org/abstract/PRL/v95/e063901

[128] H. P. Paudel, M. F. Baroughi, and K. Bayat, "Plasmon resonance modes in two-dimensional arrays of metallic nanopillars," *J. Opt. Soc. Am. B*, vol. 27, no. 9, pp. 1693–1697, Sep 2010. [Online]. Available: http://josab.osa.org/abstract.cfm?URI=josab-27-9-1693